Dissertation

submitted to the

Combined Faculties for the Natural Sciences and for Mathematics

of the

Ruperto-Carola University of Heidelberg, Germany

for the degree of

Doctor of Natural Sciences

Put forward by

Dipl.-Phys. Kristin Stefanie Grußmayer

born in: Karlsruhe, Germany

Oral examination: 28.10.2015

Fluorescence Quantification by Photon Statistics: From Objective Characterization to Application

Referees:

Prof. Dr. Dirk-Peter Herten
Prof. Dr. Wolfgang Petrich

ABSTRACT

Quantitative information is key to unravel molecular processes in all fields of research. Counting by Photon Statistics (CoPS) is a single molecule technique that provides such quantification for fluorescent species. CoPS exploits the photon antibunching effect to infer the number of independent emitters and their molecular brightness from multiple photon detection events. I laid the foundation for high quality results by improving the microscope detection efficiency more than threefold compared to earlier measurements. Using both simulations and experiments with defined, DNA-based probes, I investigated the critical interplay of fluorophore properties and analysis parameters. I discovered that measurements at high molecular brightness can be ten times faster than previously established which opens new possibilities for time resolved quantification. The findings stress that the choice of analysis parameters is vital and provide an objective measure of fluorophore eligibility for CoPS. I characterized sixteen organic dyes across the visible spectrum based on their molecular brightness and photostability. This study accomplished the transition of CoPS from a proof of concept technique to a widely applicable quantification method. Experiments demonstrated that CoPS can reveal the label number distribution of fluorescent markers, a prerequisite for quantitative investigations in biology. Moreover, I showed that CoPS offers new perspectives for characterization of photophysical processes in photoluminescent materials.

ZUSAMMENFASSUNG

Quantitative Daten sind – unabhängig vom Forschungsgebiet – der Schlüssel zum Verständnis von Prozessen, die sich auf molekularer Ebene abspielen. Zählen durch Photonenstatistik (Counting by Photon Statistics, kurz: CoPS) ist eine Einzelmolekültechnik die fluoreszierende Spezies quantifiziert. CoPS nutzt den Photon Antibunching-Effekt um die Anzahl unabhängiger Emitter und deren molekulare Helligkeit aus dem Auftreten von Mehrfach-Photonenereignissen abzuleiten. Als Grundlage für qualitativ hochwertige Ergebnisse habe ich zunächst die Detektionseffizienz des Mikroskops im Vergleich zu früheren Messungen mehr als verdreifacht. Mit Simulationen und Experimenten an definierten, DNS-basierten Proben konnte ich in Folge das kritische Zusammenspiel von Farbstoffeigenschaften und Analyseparametern untersuchen. Ich habe herausgefunden, dass Messungen bei hohen molekularen Helligkeiten bis zu zehn mal schneller als zuvor durchgeführt werden können, was neue Möglichkeiten für zeitaufgelöste Quantifizierung eröffnet. Die Erkenntnisse unterstreichen die Wichtigkeit der Analyseparameterwahl und ermöglichten ein objektives Maß für die Eignung von Fluorophoren für CoPS. Ich habe sechzehn organische Farbstoffe im sichtbaren Spektrum anhand ihrer molekularen Helligkeit und Photostabilität charakterisiert. Diese Studie markiert den Übergang von CoPS von einer reinen Machbarkeitsstudie zu einer breit anwendbaren Quantifizierungsmethode. Ich konnte demonstrieren, dass man mit CoPS die Verteilung der Fluoreszenzfarbstoffe auf Markerproteinen messen kann, eine Grundvoraussetzung für quantitative Untersuchungen in der Biologie. Des Weiteren konnte ich zeigen, dass CoPS neue Perspektiven für die Charakterisierung von photophysikalischen Prozessen in photoluminiszenten Materialen bietet.

Im Gedenken an meine Oma.

TABLE OF CONTENTS

Part I

INTRODUCTION AND FUNDAMENTALS

1

INTRODUCTION

1.1 MOTIVATION

Children start to count from age 2 on and refine the developed skill in the years after [1–3]. A recent study suggests that we begin to grasp the principles of counting already in infancy by witnessing our parents, siblings or other public demonstrations of counting [4]. As we grow up, counting becomes an routine task in our daily lives. It is straightforward even for young children, e.g., to determine the number of apples that are sitting in a bowl. They can easily distinguish individual apples and if there are many, take them out of the container one by one to facilitate the counting routine. Unfortunately, the task of counting is not always that simple when moving from macroscopic to microscopic dimensions.

To understand the function of living organisms, we need to unravel the complex inner workings of cells. For instance, self-association and oligomerization is crucial for the function of many proteins [5]. Clustering of cell surface receptors is a mechanism to enhance local protein concentrations that may lead to efficient signal transfer accross the plasma membrane by amplification of signaling. For example, tumor necrosis factor (TNF) receptors are believed to form such clusters for apoptosis signaling in response to binding of cytokines [6–8]. Again, counting is important to fully understand the process.

The first step to quantify the target proteins is to identify them in the crowded cellular environment. Fortunately, fluorescence microscopy has emerged as a minimally invasive technique that is ideally suited for this task. It allows the specific investigation of proteins in live cells with high spatial and temporal resolutions. With microscope schemes that suppress background signals by spatial selection [9, 10] and extremely sensitive semiconductor devices as detectors [11], single fluorescence molecules and even single photons can be detected. The observation of single molecules allows measurement of transport, kinetics far from thermal eqilibrium and uncovers heterogeneity that is often hidden in ensemble measurements [12]. However, the extremely valuable information about the number of proteins in a complex at the single molecule level cannot be easily extracted.

The resolution of conventional far-field light microscopy is limited by diffraction to a few hundred nanometers. The dimensions of

molecular complexes are much smaller so that individual entities — unlike the apples in the bowl — cannot be resolved in space. Super-resolution methods established in the past decade greatly enhanced the spatial resolution, but do not routinely reach molecular-scale [13–16].

Therefore, alternative approaches are needed that allow quantification below the resolution limit. Here, I am using counting by photon statistics (CoPS), a calibration free single molecule technique that is based on the fundamental principle of photon antibunching, to infer the number of independent emitters and their molecular brightness. This method is not only suited for application in biology, but is extremely useful for the investigation of new materials.

2

FUNDAMENTALS

2.1 QUANTITATIVE FLUORESCENCE MICROSCOPY

2.1.1 *Estimation of Molecule Numbers in Biology*

Most biomolecules are not naturally fluorescent. The need to fluorescently label molecules of interest (MOI) for observation is a great advantage and a demanding challenge for fluorescence microscopy at the same time. Provided fluorescent labels are of high quality and labeling is specific, researchers can identify and investigate a certain molecular species, e.g., against the vast background of proteins, lipids and small molecules of a cell [13]. The most common labels to date are fluorescent proteins, organic dyes and semiconductor quantum dots [17]. In this study, I mainly used organic dyes for they are small in size ($\sim$1 nm), come in all colors of the visible to near-infrared spectrum and have reasonable brightness and photostability [18]. Here, I will first explain the basic photophysics of organic dyes. Then, I will describe the most common labeling schemes and discuss critical implications for quantitative investigation of biological complexes.

The photophysics of organic dyes, generally small organic molecules containing conjugated π-bond systems, can be explained by a Jablonski diagram (see Figure 1). This simplified term scheme illustrates possible transitions between different energy and spin states of a molecule. For a more rigorous treatment of transition rules, molecular spectra and interactions of light and matter, please refer to the books of Demtröder and Lakowicz [19, 20].

The absorption and fluorescence emission spectra are continuous in solution and usually mirror images of one another. Typically, stimulated emission does not play a role at room temperature as long as the excitation intensity is low. Fluorescence emission is in general independent of excitation (Kashas rule) and shifted towards higher wavelengths (Stokes shift, Franck-Condon principle). After absorption of a photon, fast internal conversion to an electronic state of lower energy and vibrational relaxation to the vibronic ground state take place before spontaneous fluorescence emission. It is also possible to populate the triplet state via intersystem crossing. Return from the triplet state to the ground state (phosphorescence) is typically delayed. This results in blinking of the fluorophore between the fluorescent on-state

and the triplet off-state (0.1 ms to 100 ms timescale) that can only be observed in single molecule imaging.

On top of the previously described processes, non-radiative decay to the ground state, e.g. due to photoinduced electron transfer (PET), collisional quenching or Förster resonance energy transfer (FRET) to an acceptor molecule excited state is possible [20]. As well, oxidation or reduction may lead to a long lived (seconds timescale), radical cation or anion off-state. Irreversible photodestruction, often through reactive oxygen species that destroy the chromophore, may happen from a variety of states as indicated in Figure 1. Photobleaching and blinking of the dyes can be prevented, e.g. by removal of oxygen from the solution and by depopulation of the dark states via a system of reducing and oxidizing agents [21].

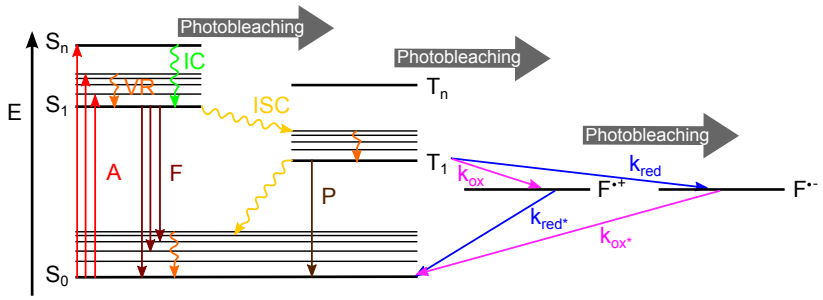

FIGURE 1: Simplified Jablonski diagram. The electronic ground state S_0, the singlet excited states S_n, the triplet excited states T_n and radical cation $F\hat{\cdot}+$ or anion states $F\hat{\cdot}-$ along with possible transitions. Absorption A, Fluorescence F, Phosphorescence P, Vibrational Relaxation VR, Internal Conversion IC, Inter System Crossing ISC, rate of oxidation and reduction k_{ox} k_{red}.

The following parameters characterize a fluorophore in addition to the wavelength of maximum absoption and emission. The molar extinction coefficient ϵ_λ is a measure of how well a dye is excited at a given wavelength and can be determined with an ensemble absorption spectrometer using Lambert-Beers' law (see Equation 1; l is the path length through a dye solution with concentration c_M). The fluorescence quantum yield Q_f describes how many fluorescence photons are emitted relative to the number of absorbed photons (see Equation 2). Usually, labels with a high brightness (see Equation 3) are preferred to achieve a good signal-to-noise ratio. Another important property is the fluorescence lifetime τ_f, i.e., the average time the molecule stays in the excited state before emitting a photon which is typically on the order of a few nanoseconds for organic dyes (see Equation 4).

$$\epsilon_\lambda = \frac{A_\lambda}{c_M l} = \frac{\log\left(\frac{I_0}{I}\right)}{c_M l} \tag{1}$$

$$Q_f = \frac{\sum k_f}{\sum k_f + k_{\text{non-radiative}}} \tag{2}$$

$$B_\lambda = Q_f \cdot \epsilon_\lambda \tag{3}$$

$$\tau_f = \frac{1}{\sum k_f + k_{\text{non-radiative}}} \tag{4}$$

The characteristics of the organic fluorophores used in this study can be found in Section 11.1. It is important to note that the above mentioned properties are all subject to changes in fluorophore environment. In particular, the tendency of a dye to photobleach varies greatly with the excitation conditions and the buffer that is used for imaging.

In the last decade, a multitude of new labeling schemes has been developed that enable the specific attachment of organic dyes to molecules of interest [17, 22–25]. To date, the most widely applied approaches can be divided into two categories, protein or short peptide tags and immunofluorescence staining with antibodies. Both are primarily used for labeling of target proteins of interest (POI).

Prominent examples of the former are the SNAP-tag and HaloTag, small enzymes that can be covalently labeled via fluorophore modified substrates [26–28]. Protein or short peptide tags are typically genetically fused to the target much like fuorescent proteins and thus provide elegant ways for introducing up to one label per protein (see Figure 2 a) and c)). This enables both *in vitro* and *in vivo* studies, given that the exogenously applied fluorescent substrate is cell permeable.

Immunofluorescence can be used *in vitro* and for labeling of endogeneous protein in fixed cells or tissue [17, 29]. A vast variety of antibodies are commercially available; they can be raised against almost any structural motif (see Figure 2 b)). Standard IgG antibodies are large in size (molecular weight $\sim$150 kDa, size $\sim$7 nm to 10 nm which is detrimental for super-resolution microscopy. Features may be broadened (linker effect) but also dense staining of small MOIs is hindered. An alternative is the digestion of IgGs until only smaller, single antigen binding regions remain (F(ab) fragments, $\sim$55 kDa). Recently, nanobodies, small single-domain antibodies from camelids or sharks, came into play ($\leq$15 kDa) [30, 31].

For quantitative measurements in a biological context, several factors need to be considered. First, labeling of the target POI should be specific and any remaining unspecific background fluorescence needs to be characterized by appropriate control measurements.

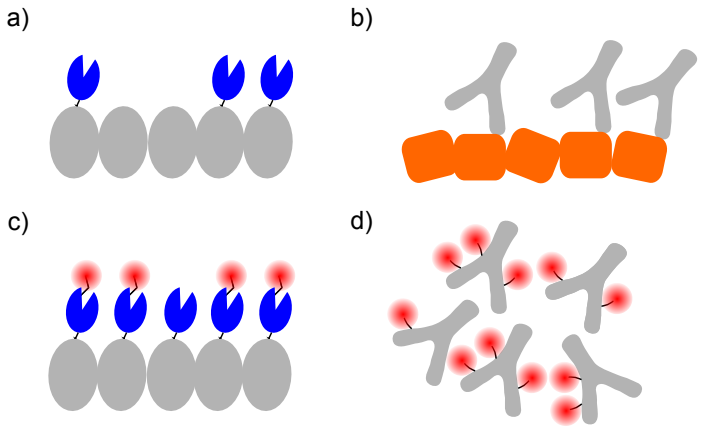

FIGURE 2: Most common labeling schemes in a biological context are protein or peptide-tags and antibodies. a) HaloTag fusion with the protein of interest (blue-grey) is coexpressed with endogeneous protein (grey). b) The degree of protein target (orange) saturation depends on antibody (grey) affinity and concentration. c) HaloTag (blue) can be covalently labeled with up to one fluorescently labeled ligand (black-red). d) Labeling of antibodies with NHS-ester activated dyes is a random process.

Next, the fraction of marker bound POI has to be determined. For tags, this includes the ratio of genetically modified to endogeneous protein (see Figure 2 a)) which may be measured e.g. by quantitative western blotting [32]. Removal or silencing of the endogeneous protein can be achieved e.g. by genome editing with CRISPR/Cas systems or RNA interference [33, 34]. This is not necessary for immunofluorescence. In fact, immunoreagents are usually directed towards endogeneous POI; target saturation depends both on the affinity of the antibody and the applied concentration during staining (see Figure 2 b)). The degree of saturation can be determined by titration of the immunoreagent and must not be confused with the degree of labeling (DOL) described below [35].

Last, a precise knowledge of the organic dye to protein marker stoichiometry is essential. For protein or peptide tags there is at most one label per construct (see Figure 2 c)). However, antibodies and their smaller counterparts are usually labeled with NHS-ester activated dyes at their lysine residues or the terminal amino function. The average number of labels per antibody may be controlled, but the individual antibody labeling is random (see Figure 2 d)). Quantitative measurements based on immunofluorescence are further complicated by the use of a combination of unlabeled primary and labeled secondary antibodies or when several polyclonal antibodies can bind to the target protein. This leads to a complex label stoichiometry that

is a convolute of the antibody labeling reaction with the primary-secondary or antibody-to-target protein distribution [36, 37].

Typically, the average label stoichiometry is determined by the degree of labeling (DOL), i.e., the relative concentrations of protein and fluorophore measured by ensemble UV/Vis absorption spectrometry (see Section 10.2). Commonly, the characteristic extinction coefficient of the individual free compounds is used to calculate the DOL. However, these are subject to change upon conjugation and the spectral properties of fluorophores may vary from protein to protein and even depend on the number of dye labels [38–42]. It has also been shown that a higher DOL often decreases protein functionality [43–45]. The ensemble absorption measurement cannot distinguish between active and inactive protein. All these issues show that the DOL can only provide a rough estimate of the average label number.

For reliable quantitative analysis, information about the underlying label number distribution of functional marker molecules is valuable. This can only be obtained with single molecule fluorescence spectroscopy (SMFS) based quantitative methods that are explained in detail in the following sections Section 2.2 and Section 2.3.

The DOL for labeling via genetic modifications can be assigned without much effort by calibration constructs with a known, fixed degree of oligomerization. One possibility is to estimate the DOL as the probability of a subunit to fluoresce by fitting a binomial distribution with a fixed subunit number N to the obtained label number distribution [46]. Otherwise, single markers can be imaged to directly measure their label number distribution in conjunction with the ordinary ensemble DOL. Label number distributions in SMFS experiments have, e.g., been acquired by single-step photobleaching (see Section 2.2) to determine the number of proteins per nanoparticle and by single-pair FRET (see Section 2.2) to measure the number of proteins per functionalized quantum dot [47, 48]. In this study, one of my tasks was to determine the label number distribution of different fluorescent markers, namely SNAP-tag, anti-GFP antibodies, anti-GFP nanobodies and streptavidin (see Chapter 7 and [49]).

The overall labeling efficiency, i.e., the number of organic dyes per POI, can be inferred from the aforementioned characterizations. This conversion factor is needed to translate the estimated number of fluorophores determined by quantitative microscopy methods (Section 2.2) into an absolute number of POI.

2.1.2 *Conjugated Polymers - Organic Semiconductor Materials*

Far-field optical microscopy is considered a mainly non-invasive technique that is ideally suited for the investigation of biological systems and is even compatible with studies of living cells or tissue [13]. Since, as mentioned before, most molecules of interest are not naturally fluorescent, elaborate schemes have been developed to achieve specific labeling. The properties of the MOI are then inferred through observation of said labels. Fluorescence and, in particular, single molecule fluorescence spectroscopy and microscopy can also be used to study the properties of the fluorescing or, more general, the photoluminescing material itself.

In this study, I also investigated so called conjugated polymers together with Florian Steiner and Jan Vogelsang from the group of Prof. Lupton at Regensburg University. These polymers are organic macromolecules that are named for their backbone chain of alternating double- and single-bonds, so called conjugated bonds (see Figure 3, top). This results in a system of delocalized π-electrons that can lead to appealing electro- and photoluminescence properties. The excitation energies of π-electrons are typically on the order of a few eV and conjugated polymers (CP) are therefore optically active in the visible wavelength regime. CPs are semiconducting materials that may be used for, e.g., field-effect transistors, light-emitting diodes and polymer solar cells [50, 51], yet they possess the convenient mechanical properties of plastics. A fundamental understanding of their electronic characteristics is needed to fully explore the potential for applications.

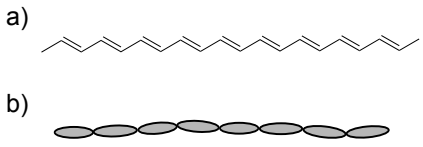

FIGURE 3: Structure of conjugated polymers. a) Polyacetylene, the most simple conjugated polymer, consists solely of a chain of alternating single and double bonds. b) Model of a conjugated polymer chain that is segmented into spectroscopic units, the chromophores.

A single polymer chain is generally not equivalent to a single chromophore. The delocalized π-electron system can be randomly perturbed by various defects (e.g. interjectional single bonds or kinks, twists) such that intact conjugation only extends over a few repeat units (see Figure 3, bottom) [51, 52]. These distinct regions form one chromophore with a singlet ground state S_0. Upon excitation by visi-

ble light, excitons (coupled electron–hole pairs) are formed. The first optically excited state is a singlet excitonic state S_1 and spin flip leads to the triplet excitonic state T_1. Triplet excitons decrease the efficiency of LEDs and may reduce the efficiency of organic solar cells [52, 53]. Chromophores in CPs can thus be decribed in the same simplified picture as for organic dyes (see Section 2.1.1).

The photophysical properties of individual chromophores [54] and of the overall CP chain is greatly influenced by chain conformation [51]. CPs are thought to be unfolded in 'good' nonpolar solvents and adopt a collapsed form in 'poor' polar solvents (see Figure 4 a) and b)). In the unfolded state, chromophores mainly emit independently and for folded chains, efficient energy transfer may take place even to the extent that the energy absorbed by the whole chain is funneled to a single emitter. This was widely studied for single polymer chains, e.g., by excitation/ emission polarization measurements, spectral changes and in simulations [55–61]. Non-classical emission from a few or even single chromophores can be determined by examining the photon statistics of CPs [62–65]. Typically, photon pair analysis with a Hanbury-Brown and Twiss beam splitter setup with two detectors (see Section 2.3) is applied. For single emitters, at most one photon is emitted per excitation cycle which manifests in a vanishing probability to detect two photons simultaneously. This characteristic photon antibunching is the only direct proof for single photon sources and can also be used to quantify the number of independent emitters (see Section 2.3.1). The alternative methods for emitter number estimation discussed in Section 2.2 are generally not applicable to CP, mainly due to a lack of necessary calibration samples.

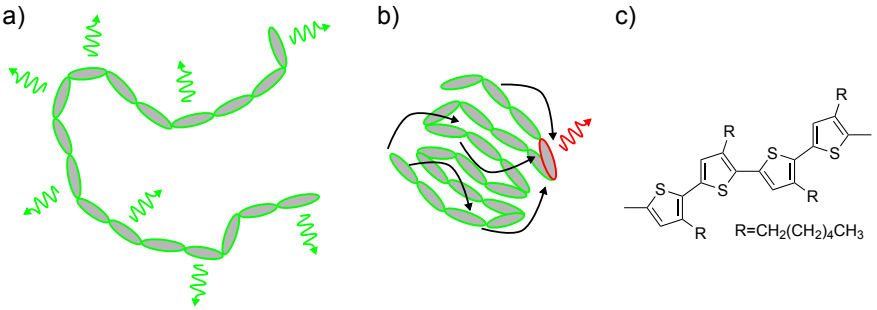

FIGURE 4: Photophysical properties of conjugated polymers depend on chain conformation and monomer structure. a) Unfolded polymer chain with independently emitting chromophores. b) Completely folded polymer chain with efficient energy transfer to a single emitting chromophore. c) Structure of poly(3-hexylthiophene).

Our collaborators previously investigated the chromophoric disorder of poly(3-hexylthiophene) (P3HT, see Figure 4 c)) in solution, bulk film and under single molecule conditions in different host matrices [65]. P3HT is a conjugated polymer frequently used in photovoltaics research [66]. They confirmed that single-chain photophysics of P3HT differs greatly depending on the chain conformation. Immobilization in a 'virtually non-polar Zeonex matrix' [65] lead to an extended structure with independent emission of multiple chromophores as determined by 'coincidence' analysis of photon pairs (see Section 2.3.1). In contrast, P3HT in poly(methyl-methacrylate) (PMMA) was completely collapsed and appeared as single emitter. Steiner et al. could also reveal that 'singlet-triplet annihilation limits exciton yield' of P3HT by controlling the chain length of folded, single P3HT chains in PMMA [53].

P3HT are poor emitters that make photon statistics analysis challenging. Here, we examined P3HT of different chain length under single molecule conditions in a Zeonex matrix. This was possible by analyzing the full photon statistics measured with an extended HBT setup with four detectors. Counting by photon statistics (CoPS), the quantification method developed in the Herten group (Section 2.3.2), is more efficient at detecting photon pairs and also considers photon triples and quadruples. It provides a suitable counting range to quantify the number of independent emitters in dependence of P3HT chain length. The simultaneous estimation of emitter brightness allowed investigation of P3HT photoluminescence quenching.

2.2 SINGLE MOLECULE FLUORESCENCE SPECTROSCOPY METHODS FOR EMITTER NUMBER ESTIMATION

Conventional far-field light microscopy in the visible to near-infrared spectrum cannot resolve structures below a few hundred nanometers due to diffraction. As mentioned before, molecular complexes are typically much smaller, so that individual subunits or binding partners cannot be resolved in space. Super-resolution methods developed in the past decade are starting to provide near molecular-scale resolution, but do not yet routinely reach it [13–16]. Therefore, alternative approaches are necessary for quantification of label or emitter numbers to, e.g., deduce the number of subunits of an oligomer or aggregate.

Here, I am focussing on quantitative single-molecule fluorescence spectroscopy (SMFS) methods. They can provide valuable information about the full distribution of states adopted by a population of molecules that may otherwise be hidden in the ensemble average.

Among the most prominent SMFS counting methods are the analysis of intensity distributions, photobleaching step counting, localization microscopy, quantification via FRET and quantification based on photon antibunching. For counting by photon statistics is the subject of this study, a complete section will be dedicated to photon antibunching approaches. I will provide a brief summary of the remainder, highlighting advantages and pitfalls of the respective method.

All diffraction limited microscopy techniques require the spatial separation of single complexes so that they can be addressed individually. The most straightforward measure for the number of labels in fluorescence microscopy is their intensity. Analysis of the intensity distribution - provided the intensity of a single label is known - may reveal the underlying label number distribution (see Figure 5 a)). This approach is feasible with all commonly used fluorophores including fluorescent proteins [67]. A prerequisite for intensity analysis is that all labels have the same brightness [68]. This requires either homogeneous illumination across the imaged field of view or correction for inhomogeneous excitation during postprocessing. Care has to be taken for differences in z-position of complexes especially for TIRF illumination where the illumination intensity strongly depends on the distance from the cover slide. Furthermore, fluorophore brightness in complex samples is subject to changes in microenvironment due to e.g. solvent effects (viscosity, pH) or fluorescence quenchers [69, 70]. For a given average intensity F_1 and corresponding standard deviation σ of single fluorophores, the intensity of N independent labels amounts to $F_N = N \cdot F_1 \pm \sqrt{N} \cdot \sigma$ [71]. It hence becomes more difficult to directly assign molecule numbers to single complexes with increasing N which limits the method to low numbers. Still, complexes with N up to four were quantified for single molecules [71–73] and the analysis of an ensemble of complexes is applied for higher oligomers or to quantify protein expression in a cell [67, 74–76].

A frequently used method consists in counting the number of photobleaching steps while continually photobleaching individual complexes (see Figure 5 b)) [77]. Here, the bottleneck lies in the reliable identification of photobleaching of single labels. This requires an excellent signal-to-noise and restricts the counting to complexes with a low number of subunits N. Photobleaching steps (BS) become harder to identify for higher N because of accumulating noise (see previous paragraph). As well, the likelihood to miss BSs because they occur simultaneously increases exponentially with the label number. BS analysis is often performed manually. This tedious task may also be carried out automatically, but existing algorithms apparently only work well for high quality data [78]. Counting the number of photobleach-

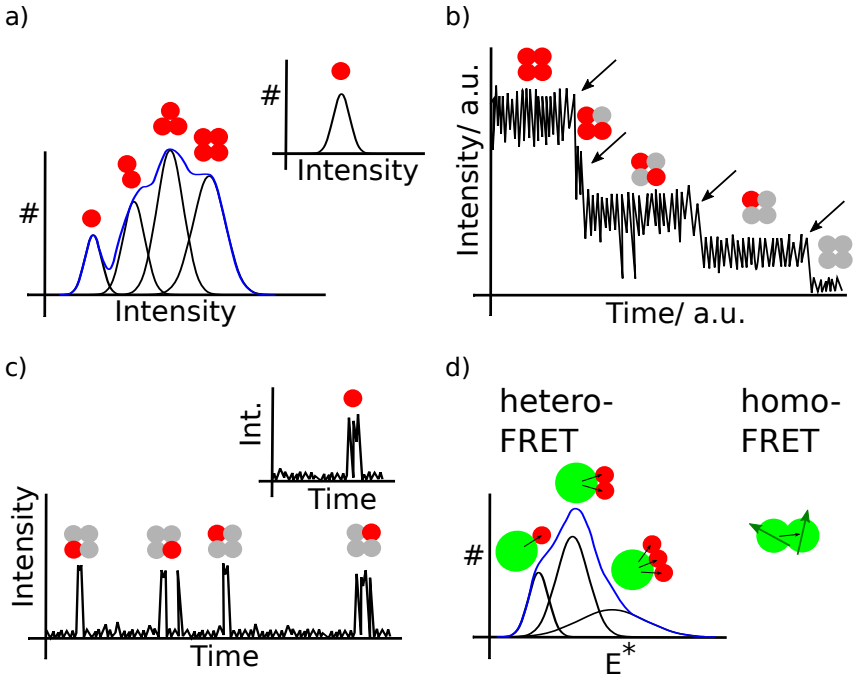

FIGURE 5: Alternative methods for fluorescence quantification. Fluorescing labels are denoted in red and non-active labels in grey. a) Analysis of fluorescence intensity or fluorescence intensity distribution and comparison with an intensity standard. b) Photobleaching step analysis. c) Localization microscopy with calibrated number of localizations per marker. d) Analysis of hetero- or homo-FRET distributions.

ing steps has been extensively used to quantify membrane receptors and ion channels in the plasma membrane [79]. With organic dyes as bright labels, up to seven BSs were reliably counted in one study [80], but the number of BSs with fluorescent protein tags is usually on the order of four or five [77]. The method is relatively easy to implement given a high quality single molecule microscope setup, but it inherently destroys the fluorescent labels which prevents dynamic measurements of emitter or subunit numbers.

Localization based super-resolution microscopy (stochastic optical reconstruction microscopy (STORM)[81], photoactivated or fluorescence photoactivation localization microscopy (PALM or FPALM)[82, 83], etc) provides yet another approach to counting molecules. Here, the stochastic on-switching of a subset of individual fluorescent molecules followed by bleaching or off-switching, temporally separates molecules that would otherwise be spatially indistinguishable. Merging of all positions of single-molecule localizations over many of such switching/imaging/bleaching cycles yields a final super-resolved im-

age because the center of individual point-spread functions can be determined with high precision [84]. The number of localizations per complex yields information about the stoichiomtry of labeled subunits (see Figure 5 c)). However, single labels may undergo more than one switching cycle and/or exhibit blinking and appear as multiple localizations which leads to overcounting [37]. On the other hand, undercounting might occur when a fraction of labels does not become activated at all in the imaging channel, when localizations are not registered during data analysis or when two labels are activated at the same time in one diffraction limited volume. Localization microscopy based quantification has the benefit of superior image resolution, it can thus tolerate higher densities of investigated complexes and provide superior contextual information. As well, the counting range does not appear to be restricted given sufficient time for complete imaging of all fluorophores. However, dynamic quantitative measurements are not possible because of the destructive imaging process. It is also obvious that absolute number determination requires additional efforts to cope with the raised concerns.

One strategy to deal with overcounting is to perform a calibration experiment to extract the number of localizations typically detected per fluorophore or per fluorescent marker. It is crucial to perform calibration experiments in the same cellular nanoenvironment because otherwise the properties of the fluorophore might change[35]. Other approaches include analysis of the time dependence of blinking and activation [85, 86], the application of pair-correlation functions [87, 88] or fourier ring analysis [89]. Undercounting can be prevented using appropriate imaging conditions [86, 90] and localization algorithms with a high recall rate [91] and failure of labels to fluoresce in the imaging channel is best characterized using calibration standards with a known oligomerization state [46].

The last single molecule number estimation method I would like to mention makes use of Förster resonance energy transer (FRET). This process describes the non-radiative transfer of energy from a so called donor fuorophore to an acceptor fluorophore. It depends on the donor-acceptor distance, the spectral overlap of the donor emission spectrum with the acceptor absorption spectrum and on the relative orientation of the respective molecular dipole moments [20]. FRET can occur between identical fluorophores and from donor to acceptor with different fluorescence properties (homo- and hetero-FRET, see Figure 5 d)). Identification of donor and acceptor emission is required for reliable hetero-FRET imaging. When the sample geometry is well defined, the interpretation of FRET values or histograms is relatively straigtforward [48]. This is generally not the case and

the most probable complex configuration is identified from the calculated pairwise FRET histogram that matches the experimentally determined distribution best [92]. Then, hetero-FRET imaging cannot provide numbers for single complexes. Homo-FRET can be quantified by observing its effect on the fluorescence anisotropy, a measure for the difference in polarization of the emission of the fluorophores [20]. Data interpretation is challenging because the mutual orientations of fluorophores and the number of fluorophores per oligomer affect the fluorescence anisotropy alike [93, 94]. Both hetero- and homo-FRET are limited to distances over which FRET occurs which in turn restricts the size of the clusters that can be analyzed (1 nm to 10 nm). Quantification via FRET typically does not exceed tetramers or pentamers [92–94].

The given account of SMFS methods only provides an overview of the most commonly applied single molecule quantification techniques. Other popular approaches are investigating ensembles of molecules; many analyze the statistical fluctuation of fluorescence intensity over time. Among them are fluorescence intensity distribution analysis [95], photon counting histogram [96] and the number and brightness method [97].

The four single molecule methods — analysis of intensity distributions, photobleaching step counting, localization microscopy and quantification via FRET — vary greatly in the accessible number range, the need for reference samples and the sophistication of the microscopes, labels and analysis. In the next section I will give detailed insight into single molecule quantification based on photon antibunching and compare its advantages and challenges with those of the above mentioned approaches.

2.3 PHOTON ANTIBUNCHING IN SINGLE MOLECULE FLUORESCENCE SPECTROSCOPY

Single molecule fluorescence spectroscopy (SMFS) allows studying the properties of individual emitters, such as fluorescence lifetime τ_f or emission spectra, under ambient conditions. A fundamental characteristic of single quantum systems is based on their capability to emit at most one photon per excitation cycle. This results in photon antibunching, that is, the probability for detecting multiple photons vanishes as the detection time window approaches zero. *We recently pubished a book chapter titled ‚Photon Antibunching in Single Molecule Fluorescence Spectroscopy' that gives a detailed account of how photon antibunching is exploited in SMFS applications [98]. In the following, a concise*

overview shall be given that amounts to the introduction of counting by photon statistics, the quantification method that is subject of this study.

The photon statistics of a light source can be measured with a so called Hanbury-Brown and Twiss (HBT) setup that consists of a 50:50 beam splitter and two sensitive detectors by correlating the signal of the two beam paths (see Figure 6). HBT used the measured second-order correlation function (intensity autocorrelation function $G^{(2)}(\tau)$ to study the temporal coherence of a light beam [99]. Coherent light sources with constant intensity such as lasers result in a flat autocorrelation function with $G^{(2)}(\tau) = 1$. On the other hand, classical light sources with time varying intensity like thermal black body radiation have $G^{(2)}(0) \geq 0$. This indicates that it is more likely to detect subsequent photons within short inter-photon time intervals meaning photons occur in bunches [100]. The opposite is true for photon antibunching, an effect that can only be described by quantum mechanics.

In short, this can be explained for single fluorophores in the simplified picture of a two-state quantum system. When the emitter is prepared in the ground state, it can be excited e.g. by laser light and remain in the excited state on average for the fluorescene lifetime. It will then, with a certain probability (fluorescence quantum yield Q_f), return to the ground state by emission of a photon. The fluorophore may then undergo the next excitation cycle, hence there will always be a finite time between emission of subsequent photons. A non-zero probability to detect multiple photons simultaneously indicates the presence of multiple independent emitters in the sample.

Photon antibunching was predicted by Kimble and Mandel [101] and independently by Walls and Carmichael [102] and first proven in experiments by Kimble et al. in 1977 [103]. The first observation for single molecules took place at low temperatures for pentacene dyes trapped in a crystal host [104].

Photon antibunching is the only direct proof for pure single photon sources. It was used to test e.g. quantum dots and nitrogen vacancy centers in diamond along with organic fluorophores under varying excitation conditions [105–113] [114–116]. The creation of single photons on demand is indispensable for quantum information processing [117–119], secure communication through quantum cryptography [120, 121] , and for quantum metrology [122].

Second, the characteristic photon statistics of single fluorophores can be utilized for estimating the number of independently emitting molecules within a diffraction limited spot. I will first present quantification by measuring photon pairs that can be accomplished with a HBT-type detection pathway and then move on to the more compre-

hensive counting by photon statistics (CoPS) with an extended HBT array.

2.3.1 *Quantification by Photon Pairs*

Most initial photon antibunching measurements of fluorescent molecules were conducted with CW laser excitation [123–127]. Photon correlations, i.e., the conditional probability of detecting a photon at time $t + \tau$ after the detection of the first photon at time t, were measured in a HBT-array with two single photon sensitive detectors (typically avalanche photodiodes (APDs)) and time-correlated single photon counting (TCSPC) electronics as mentioned above (see Figure 6). It is necessary to use two detectors because they have a dead time of about 50 ns that is larger than the measurement timescale set by the fluorescence lifetime of small organic dyes. Here, I want to point out that it is important to use appropriate filters in front of APD detectors to avoid infrared photons that may be emitted by the diode material in the process of photon detection [64, 128]. Otherwise those might lead to additional peaks in the inter-photon time histogram.

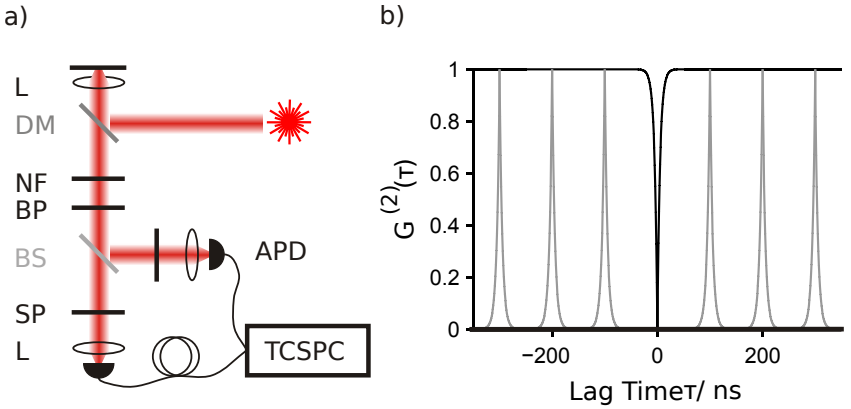

Figure 6: Quantification by photon pairs. Modification of Figure 1 and Figure 4 of [98]. a) Point-scanning microscope with CW laser excitation and HBT-array detection scheme; fluorescence photons are split 50:50 towards two avalanche photon diodes (APDs) by a non-polarizing beam splitter (BS). Time-correlated single photon-counting (TCSPC) allows the determination of the histogram of inter-photon arrival times. DM dichroic mirror, BP bandpass filter, SP shortpass filter, L lens. b) Modeled inter-photon time histogram for CW (black line) and pulsed (grey line) laser excitation. The repetition rate of 10 MHz results in distinct peaks every 100 ns with a width depending on the fluorescence lifetime

The expression for normalized photon correlations $G^{(2)}(\tau)$ can be easily derived for N identical, independent emitters. Both APDs are considered equal and all emitters shall contribute alike to the constant average intensity $\langle I(t)\rangle = N\langle i(t)\rangle$. For simplicity, background photons are neglected.

$$G^{(2)}(\tau) = \frac{\langle n_1(t)\, n_2(t+\tau)\rangle}{\langle n_1(t)\rangle\langle n_2(t+\tau)\rangle} = \frac{\langle I(t)\, I(t+\tau)\rangle}{\langle I(t)\rangle^2} = \frac{N(N-1)}{N^2} + \frac{1}{N}\frac{\langle p(t)\, p(t+\tau)\rangle}{\langle p(t)\rangle^2} \tag{5}$$

n_m is the number of registered counts at detector m that is proportional to the intensity I_m. $G^{(2)}(\tau)$ is described by the number of emitters N and by the conditional probability of emitting a photon at time t and emitting a second photon at time $t+\tau$ in the following excitation cyle. This conditional probability for a simple, immobile two-state system can be derived from rate equations for excitation and emission and the initial conditions. The solution for the general case of diffusing molecules with more than two states can be found, e.g., in [104, 128, 129]. Equation 6 describes the antibunching dip in the correlation function (see Figure 6 b), black line) with a width depending on the rate of excitation k_{ex} and spontaneous fluorescence emission k_f. Since the amplitude of the dip is antiproportional to the number of independent emitters N, antibunching measurements with CW laser excitation can be used for quantification.

$$G^{(2)}(\tau) = 1 - \frac{1}{N}\exp\left(\frac{\tau}{T}\right) \tag{6}$$

$$T = \frac{1}{k_{ex} + k_f} \tag{7}$$

There were a number of experiments that investigated the influence of chain conformation on the photophysics of multichromophoric conjugated polymers (see Section 2.1.2) [62, 63]. Other studies were interested in the number of nitrogen-vacancy color centers in nanodiamonds [130] or characterized the single photon emission of B-Phycoerythrin (B-PE), a highly fluorescent phycobiliprotein found in the light harvesting structures of red algae and cyanobacteria [131]. It contains 34 bilin chromophores in close proximity that very efficiently transfer their energy to only one emitter.

Random emission upon CW excitation leads to inefficient detection of photons because many cannot be registered due to the dead time of the detectors. Older TCSPC electronics that directly measure the

inter-photon time by assigning start- and stop-channels to the APDS instead of time-tagging the individual photons aggravate the problem [98]. Under ambient conditions, single (probe) molecules were generally not sufficiently photostable to reconstruct a proper histogram of inter-photon arrival time delays. Often, photon pair correlations could only be characterized for an ensemble of molecules.

This limitation can be overcome using excitation with short laser pulses ($\leq$100 ps) that excite the fluorophores only once. If the time between laser pulses is longer than the dead time of the detectors and TCSPC electronics, photon detection is maximized. Photons then arrive periodically with the laser pulses delayed by the fluorescence lifetime. Also, photochemical stability is extended compared to CW laser excitation because molecules undergo less excitation cycles per time interval. Now, photon correlation consists of peaks with a spacing that reflects the laser repetition rate and a width according to the fluorescence lifetime. The peak around lag time zero corresponds to 'coincident' photon pairs from the same laser cycle whereas the satellite peaks represent photon pairs from different laser pulses (see Figure 6 b), gray line). The signature of single photon emitters remains the vanishing probability for detecting multiple photons as the detection time window approaches zero, i.e., the central peak disappears. This was first demonstrated by Lounis and Moerner who created 'single photons on demand from a single molecule' [108].

Of course, pulsed laser excitation antibunching experiments still contain the information about the number of independent emitters. The coincidence ratio $\frac{N_c}{\langle N_l \rangle}$ between the central peak and the lateral peaks with $\tau \gg \tau_f$ can be recovered from Equation 6 with $\tau = 0$ or it may be derived by combinatorics [98] (see Equation 8).

$$\frac{N_c}{\langle N_l \rangle} = 1 - \frac{1}{N} \tag{8}$$

The more efficient pulsed laser excitation permitted simultaneous monitoring of several photophysical parameters, such as the coincidence ratio, fluorescence intensity and fluorescence lifetime, over time for single molecules on surfaces or attached to DNA *in vitro* and in cells [132–134]. Coincidence ratio measurements were performed, e.g., for DNA-hairpin probes with up to three fluorescent dyes or to determine the number of apolipoprotein A-I molecules in high density lipoprotein particles [135, 136].

When photon statistics are used to quantify the number of constituents in a complex, energy transfer between the fluorescent labels should be prevented. All emitters must be fluorescing independently

to avoid undercounting. Sánchez-Mosteiro and coworkers [137] discovered that fluorescent protein tetramers of DsRed appear mostly as single emitters presumably due to efficient energy transfer between the chromophores. Other well defined complexes appeared with reduced fluorophore numbers as well [128].

The ability of photon antibunching experiments to measure the number of active, independent emitters has been extensively used to investigate energy transfer in single molecules of engineered multichromophoric systems [138–144] and in model systems of conjugated polymers [64, 65] (see Section 2.1.2).

2.3.2 *Counting by Photon Statistics — State of the Art*

In the previous section, I have introduced the analysis of the temporal distribution of photon pairs. Both measurements with CW and pulsed laser excitation can be used to infer the number of independent emitters that contribute to the photon statistics. The respective measures for antibunching, i.e., the magnitude of the dip in the second-order correlation function or the relative weight of the central peak, scale with the number of emitters as $1 - \frac{1}{N}$. In practice, this function quickly saturates and can scarcely be used for counting up to three or four.

Work in the Herten group over the past years has demonstrated, both in simulations and experiments, that the counting range can be considerably expanded when photon triples and quadruples are taken into account [145–148]. This can be realized experimentally with an extended HBT-array with four detectors and pulsed laser excitation (see Figure 7). As for conventional 'coincidence' analysis, short pulses with moderate repetition rates ($\tau_{\text{laser pulse}} \ll \tau_f \ll \tau_{\text{laser repetition}}$) are used to ensure efficient detection of at most one photon per independent emitter and laser cycle. Multiple photon detection events (mDE) in one laser cycle again signify multiple emitters in the sample (see Figure 8).

The probability $P_m\left(N, p; i\right)$ for i detection events depends on the number of independent emitters N in the focus, on the average photon detection probability per laser pulse and per label of the microscope setup (short: detection probability p) and on the number of equivalent detectors m (here: $m = 4$). Again, all N emitters are considered identical with alike brightness. The full photon statistics are derived from the stochastic processes of excitation, emission, and detection of photons comprising the geometry of the detection pathway and can be constructed from a multinomial distribution.

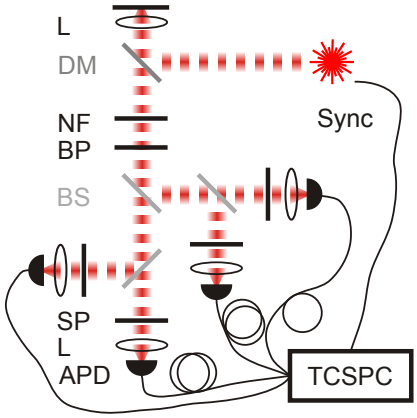

FIGURE 7: Microscope setup used for Counting by Photon Statistics with an extended HBT-array. Modified Figure 7 from [98]. Point-scanning microscope with pulsed laser excitation; fluorescence photons are directed towards four avalanche photon diodes (APDs) by three non-polarizing 50:50 beam splitters. The absolute photon arrival time for each APD is registered by TCSPC with four synchronized, independent channels. DM dichroic mirror, BP bandpass filter, SP shortpass filter, L lens.

In experiments, additional mDE occur due to random 'coincidences' of background photons with signal photons. Since scattering in the sample and electronic noise are low, the background can be modeled as an additional single, dim fluorophore with fixed background detection probability between $p_b = 0.1 \times 10^{-4}$ to 5×10^{-4} to yield $P_{m,p_b}(N, p; i)$ (Equation 9). It should be noted that only one photon can be registered per TCSPC channel and per laser cycle due to the combined dead time of the detectors and electronics. The missing mDE are accounted for in the model of photon statistics. The recursive formula in Equation 9 consists of two parts. The first is the probability for i mDE and the second is the sum of all probabilities for mDE$\leq$i.

$$P_{m,p_b}(N, p; i) = \binom{m}{i} \left[\left(1 - \left(\frac{m-i}{m}\right) p\right)^N \left(1 - \left(\frac{m-i}{m}\right) p_b\right) \right] - \sum_{k \geq 0}^{i-1} \frac{\binom{i}{k}}{\binom{m}{k}} P_{m,p_b}(N, p; k) \tag{9}$$

$$p = \frac{I_{\text{laser}}}{f_{\text{laser repetition}} h\nu} \sigma_{abs} Q_f \eta_{det} \tag{10}$$

Typically, mDE are calculated by post-processing the four-channel TCSPC data of a certain number of laser cycles (LC) (= analysis pe-

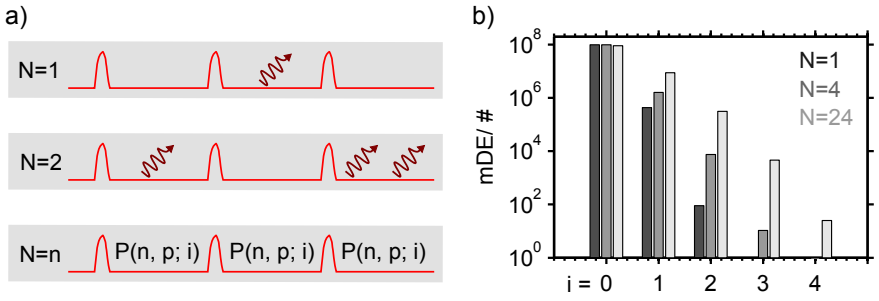

FIGURE 8: Counting by Photon Statistics. a) Scheme of multiple photon detection events (mDE) after laser excitation depending on the number of emitters N in the focal volume. b) Probability for i detection events and $N = 1$, 4 and 24, detection probability $p = 4 \times 10^{-4}$ and background detection probability $p_b = 3 \times 10^{-4}$.

riod t_{acq}) (see Figure 8 b)). The number of independent emitters N and their detection probability p can then be estimated by non-linear regression of the model $P_{m,p_b}\left(N, p; i\right)$ to the mDE data with the standard Levenberg– Marquardt algorithm [149]. In truth, only four of the mDE probabilities of the four detector model are independent from one another. Since covariances are small $< 10^{-3}$, these dependencies are neglected.

The detection probability p (see Equation 10) only differs from the molecular brightness ϵ_{MB} by the laser repetition rate $f_{\text{laser repetition}}$ (= laser repetition frequency). Both depend on the photon flux, i.e., the average laser intensity I_{laser} divided by the photon energy $h\nu$ during the laser pulse, the absorption cross-section σ_{abs}, the fluorescence quantum yield Q_f and the overall detection efficiency of the microscope setup η_{det}.

In the case of $m = 4$ detectors and for small $N \cdot p \ll 1$, the probability for mDE can be approximated by Equation 11. Only a higher number of bright emitters lead to significant mDE with three and four photons.

$$P_{4,p_b}\left(N, p; 1 \leq i \leq 4\right) \sim \prod_{k=0}^{i-1} \left(N - k\right) p^i \tag{11}$$

In fact, the probability to detect single photons is the same for microscope setups with four and two detectors in the limit of $N \cdot p \ll 1$, but the former is 1.5 fold more efficient at collecting photon pairs $\left(P_{4,p_b}\left(N, p; i = 2\right) = 1.5 \cdot P_{2,p_b}\left(N, p; i = 2\right)\right)$ [147]. In addition, higher maximum count rates should be tolerable since only a fourth of the overall signal reaches one detector. Four detector, four channel TC-

SPC enables more efficient photon collection and should allow the collection of mDE for a higher number of bright fluorophores before the detectors and read out electronics are saturated. All in all, this new approach, which was termed counting by photon statistics (CoPS) [148], provides more information and allows a significant extension of the limited counting range of two-detector 'coincidence' analysis.

Initial studies demonstrated the potential of CoPS with Monte Carlo simulations for the idealized case without background [145]. Estimation with CoPS showed no significant bias for simulated emitter numbers up to $N = 50$ and a detection probability of $p = 2.5 \times 10^{-3}$. When the number of laser cycles (LC) included in the analysis period was varied from 4 MLC, 8 MLC and 16 MLC for better mDE statistics, the relative standard deviation decreased from about 20 % to 30 % and 10 % to 15 % down to 5 % to 8 %.

The first experimental realization of CoPS used DNA based probes with up to five bright and photostable organic Atto647N dyes [146]. The analysis period was manually adjusted for each analyzed fluorescent transient to include as many photons as possible before the next photobleaching step occured. CoPS analysis resulted in sensible label number estimates slightly higher than determined by photobleaching step (BS) analysis (see Section 2.2) and correlated with the stepwise decrease in fluorescence intensity traces.

At the early stages of my work, I was involved in experimentally investigating the counting range of CoPS [148]. We used DNA origami labeled with Atto647N as a probe with defined, higher number of emitters [68]. In addition, repeated fitting of a random subset of mDE data (for details refer to Section 12.8) [150, 151] was introduced to achieve more robust parameter estimation and to provide error estimates for individual CoPS measurements.

Altogether, we could show that CoPS is a promising quantification method based on photon antibunching with an extended counting range with respect to 'coincidence' analysis of photon pairs. Reliable CoPS number estimates can be made in experiments with Atto647N at least in the number range of 1–20 in as little as 3 MLC or 150 ms (at a laser repetition rate of 20 MHz and moderate laser excitation). Photobleaching of Atto647N takes place on a larger timescale which puts repetitive or dynamic measurements of emitter numbers into perspective. CoPS works well with bright and photostable emitters because they have the prerequisite to deliver sufficient mDE statistics. Some of the alternative single-molecule quantification methods pose less stringend requirements on labels, but most need calibration measurements and a number of corrections or controls for reference (see

Section 2.2). CoPS provides emitter number and brightness estimates directly by analysis of the full photon statistics of a sample.

Broadening the range of fluorophores that can be used for counting by photon statistics is essential to render the method more widely applicable. Conceptually, candidate dyes may be chosen from the whole visible to near-infrared wavelength regime because the nature of photon statistics does not depend on spectral parameters. In order to do so, minimal requirements in terms of brightness and photostability of a dye need to be known. This knowledge is indispensable for measurements, e.g., in living cells where the dyes that can be used for staining are limited. Unraveling the relation between photon detection probability and minimal analysis period for CoPS measurements, i.e. the maximal achievable time resolution, is key for further successful applications.

2.4 SCOPE OF THIS STUDY

This study is driving the transition of Counting by Photon Statistics (CoPS) from a static, proof of concept technique to a widely applicable fluorescence quantification method able to observe dynamic processes. In CoPS, the statistics of measured multiple photon detection events from a diffraction limited volume are modeled to estimate the number and molecular brightness of independent fluorescent emitters within. Obtaining sufficient photon statistics is crucial for the quality of CoPS estimates and depends on the overall photon detection efficiency of the microscope setup, the fluorescent emitters in use and on analysis parameters.

As a first step, the detection efficiency of the single molecule fluorescence microscope used for CoPS will be improved. This will be realized by removal of dispensable optical elements and introduction of new, optimal components including a higher numerical aperture objective. This will both open up the possibility to increase the achievable time resolution of CoPS and to use fluorophores that were previously too dim or prone to premature photodestruction. As well, the fluorescence excitation will be modified to simplify switching between different excitation sources resulting in a flexible CoPS setup for measurements with multiple colors.

Emphasis is then put on unravelling the interplay of dye properties and analysis parameters in CoPS estimations. The molecular brightness and photostability of emitters and the analysis period to collect photon statistics are varied both in simulations and in experiments with defined, DNA based probes. This will reveal minimal requirements in terms of brightness and photostability to be met by fluo-

rophores for use with CoPS and determine the maximal time resolution achievable in CoPS measurements.

Next, a large set of organic dyes across the visible wavelength regime will be systematically evaluated in CoPS measurements. Proof of concept simulations and experiments with DNA based probes demonstrated the feasability of CoPS and characterized the accessible number range solely using the dye Atto647N. Conceptually, there is no limitation in spectral parameters for CoPS. Finding more suitable dyes will greatly expand the applicability of this counting method and open possibilities for multiplexing. It will be determined if the fluorophores under investigation meet the prerequisites for successfull CoPS implementation and, if that is the case, the relative molecular brightness estimates by CoPS will be verified by known extinction coefficients and quantum yields of the fluorophore.

As a first demonstration of CoPS in a biological context, the label number distribution of two organic dyes on different fluorescent markers will be investigated *in vitro*. Those marker proteins are routinely used to signal the presence and location of proteins of interest. The precise knowledge of these labeling stoichiometries is a prerequisite to infer the oligomerization or aggregation state of a certain protein and paves the way for in depth biological studies.

The last part of this work will be dedicated to the study of photoluminescent conjugated polymers that are heavily investigated due to their use in organic semiconductor devices like solar cells. This emphasizes the broad application range of CoPS and will show that the method is not limited to classic organic dyes. The measurement of independent exciton number as a function of polymer molecular weight and the dynamic observation of exciton number and molecular brightness will provide new insights into polymer photophysics and morphology.

Part II

EXPERIMENTS AND RESULTS

3

OVERVIEW

In this part, counting by photon statistics is demonstrated as a versatile and widely applicable fluorescence quantification method. First, experimental optimizations to the single molecule fluorescene microscope setup for CoPS are discussed that form the basis for all subsequent measurements. Then, the method is characterized with respect to dye brightness, photostability and the chosen analysis parameters both in simulations and experiments. The gathered information is used to screen for suitable dyes in the red, green/yellow and green/blue wavelength regime. The versatility of the CoPS methods is demonstrated in the last two chapter by applying it to open problems in two different fields. In a biological context, I investigated the label number distribution of fluorescent markers. Finally, I used CoPS in the context of polymer semiconductor physics where I investigate the number of independent emitters of conjugated polymers and shed light on their photoluminescence quenching mechanisms.

4

IMPROVING THE SINGLE MOLECULE FLUORESCENCE MICROSCOPE FOR COPS

It is the nature of single molecule fluorescence microscopy to make the most out of a limited photon budget. Therefore it is crucial to optimize both the experimental conditions as well as to adapt the analysis routine to the task at hand. In general, the quality of molecular brightness and emitter number estimations with CoPS increases the better the statistics of multiple photon detetion events are. At the heart of experimental conditions lies the fluorophore that is chosen for measurements and the microscope setup that should be adapted to the spectral parameters of the fluorophore.

In the first experimental demonstration of CoPS [146], a detection probability of $p \approx 1.3 \times 10^{-3}$ was reached with 10 µW diffraction limited laser excitation of a DNA hybridization probe labeled with Atto647N at a repetition rate of 10 MHz. At the beginning of my work, I was involved in experimentally investigating the counting range of CoPS [148]. Then, the same setup reached a detection efficiency of $p \approx 2 \times 10^{-3}$ with 18 Atto647N dyes on DNA origami using the same mean excitation power at 20 MHz laser repetition rate.

Before I started the first CoPS measurements for this work, I remodelled part of the CoPS microscope detection pathway together with my coworker Anton Kurz (see Section 10.1). I achieved a more than four- or threefold increase in detection probability with respect to the first CoPS measurements and the DNA origami data, to $p \approx 6 \times 10^{-3}$ for measurements with 10 µW diffraction limited laser excitation of the same DNA hybridization probe labeled with Atto647N at a repetition rate of 20 MHz (see Section 6.1). The average photon detection probability per laser pulse and per label (compare Equation 10) scales linearly with the overall detection efficiency of the microscope setup $p \propto \eta$. The average laser excitation power was the same in all experiments, but the first experiment was conducted at half laser repetition rate and thus had a higher laser power per pulse. Hence, the increase in microscope detection efficiency was even higher than fourfold.

$$\eta(\lambda) = \tfrac{1}{2}(1 - \cos\theta)\, T\, \eta_{detector} \tag{12}$$

$$NA = n_{ref} \sin\theta \tag{13}$$

The detection efficiency depends on the light collection efficiency of the microscope objective, the overall transmission T of all optical elements and on the detection efficieny of the detector as defined in Equation 12. A major improvement was the removal of the microscope tube lens and the use of a higher numerical aperture objective (see Equation 13 with $n_{ref} \approx 1.52$ refractive index of the immersion oil and θ half-opening angle of the objective lens , NA = 1.45 instead of NA = 1.4). As well, I used optimized filter sets in all experiments (here, bandpass filters 685/70 instead of 675/50). All my measurements were performed without confocalization by a pinhole. This was possible because I used well defined, immobilized samples throughout my thesis and background levels were low enough for CoPS analysis. For example, single molecules of conjugated polymer were spin coated in a layer of only $\sim$200 nm thickness, not even exceeding the dimensions of the diffraction limited observation volume in the axial dimension. Of course, the instrumentally possible overall microscope detection efficiency is only reached for proper alignment of the microscope.

This rise in detection efficiency allows for an increase in the achievable time resolution of CoPS or for an increase in estimation precision (see Chapter 5) with otherwise unchanged excitation parameters. Furthermore, it enables the use of fluorophores that were previously too dim for CoPS or allows lowering the excitation power to measure fluorophores that are easily destroyed by photobleaching. The detection efficiency depends on the wavelength range mainly because the avalanche photodiode detectors have wavelength dependent detection quantum yields [11]. This CoPS setup is optimized for detection in the red wavelength regime. The detection efficiency could be further improved by even higher NA objectives and possibly by custom-designed microscope and optics with even less transmission losses. However, the NA cannot be increased much due to the requirement of matching index of refraction between objective lens, immersion oil and glass coverslip. Commonly, borosilicate glass with a refractive index of about $n_{ref} \approx 1.51 - 1.54$ across the visible spectrum is used.

As a second step of microscope modification, I completely changed the excitation pathway of the CoPS setup in order to facilitate measurements with different laser excitation sources. Initially, an open beam path was realized with a 635 nm and a 470 nm picosecond pulsed laser overlaid using a dichroic mirror (for details please refer to Section 10.1). This was replaced by a fibre coupling unit comprising a 640 nm, the 470 nm and a 532 nm picosecond pulsed laser (for deteails please refer to Section 10.1). The previous red laser had to be exchanged due to emerging long term power instability. The new

beam path aligned the different lasers optimally by coupling them into one fibre. In the course of this remodeling the beam waist before coupling into the microscope was reduced to 2 mm by a common collimator for all lasers. The intention was to underfill the back aperture of the objective to obain a more extended point spread function with less variation of excitation intensity in the center.

All in all, the current CoPS microscope includes simple switching between three colors in a well shielded setup with high detection efficiency.

5

UNRAVELLING THE INTERPLAY OF DYE PROPERTIES AND ANALYSIS PARAMETERS IN COPS ESTIMATIONS

Fluorescence quantification with CoPS is based on measuring multiple photon detection events (mDE) followed by modeling of these photon statistics to estimate the number and photon detection probability of the underlying independent emitters. The quality of CoPS number estimation thus depends on the ability to accurately determine the distribution of mDE in experiments. Clearly, the measurement of relative frequencies of mDE improves the longer the analysis period to collect the photon statistics lasts. The absolute number of mDE obviously increases with increasing detection probability, concurrently the relative error of mDE measurement decreases. In fact, the probability to detect i photons per laser cycle for a given emitter number scales roughly with p^i [98]. The detection probability for experiments with a given microcope setup, i.e. a given detection efficiency, depends on the chosen fluorophore and laser excitation power. In principle, fluorescence emission will increase with the laser excitation power until the saturation limit of resonance fluorescence is reached [152, 153]. In turn, the photostability of the fluorophores will decrease, posing a natural upper limit to the CoPS analysis period.

In this section, I will present both simulations and experiments with defined, DNA based probes. My objective is to determine the minimal requirements in terms of brightness and photostability for a suitable dye to deliver reliable CoPS estimates and to obtain the maximal achievable time resolution of the method.

5.1 OPTIMAL COPS ANALYSIS FOR SIMULATED DATA

I started to investigate the interplay of dye properties and analysis parameters by simulation using the Monte Carlo method to generate single molecule CoPS data. I simulated N independent emitters that reside exactly in the center of the observation volume, i.e they have exactly the same brightness hence the same p. Neither variation in brightness over time, nor intersystem crossing of emitters into the triplet state or any related reduced or oxidized state where return to the ground state is delayed, were simulated. The omission of blinking from the simulations reflects the supression of blinking in

experiments by means of a system of reducing and oxidizing components (ROXS) in the measurement buffer (see Section 12.3). For each laser cycle and fluorophore, random sampling determines if a photon is detected and which of the four detectors it reaches (see Figure 9 and Section 2.3.2). Photobleaching can be included in the simulation by stopping photon emission of a fluorophore at the assigned photobleaching time. Details about the implementation can be found in Section 12.9. The final output of the simulation is four files that contain the macrotime of detected photons for each detector, much like the experimentally generated data. The data was then analyzed exactly like the experimental data (see Section 2.3.2).

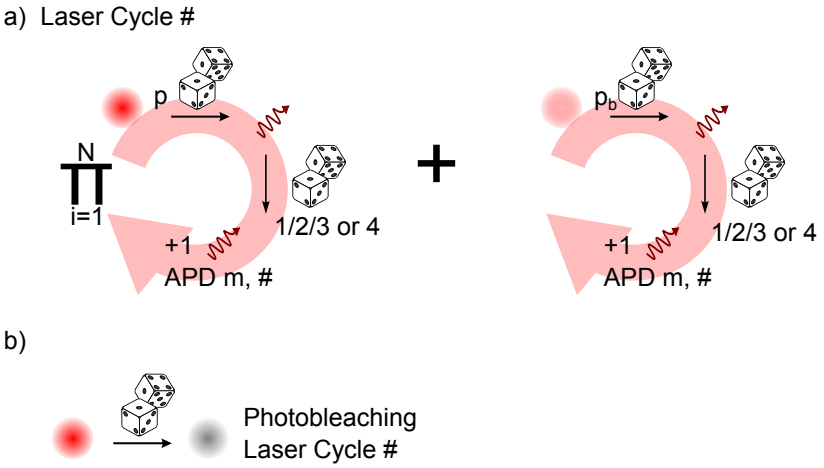

FIGURE 9: Illustration of the generation of CoPS data using the Monte Carlo method. a) Simulation of photons from N emitters with detection probability p and background photons from one dim emitter with background detection probability p_b in one laser cycle. b) Simulation of photobleaching by random sampling from an exponential distribution with mean photostability time τ_{ph}

To verify that the simulations were correctly implemented, I compared the probability of multiple detection events calculated from the simulations with the predictions from the CoPS model supplied with the parameters of the simulation. I chose a detection probability of $p = 4 \times 10^{-3}$ for fluorophores and a background detection probability of $p_b = 3 \times 10^{-4}$, similar to what is typically obtained in experiments. In all the simulations, unless noted otherwise, 200 traces that last for 100 MLC or 5 s were simulated. To assure good statistics, all the data from the simulated traces were included, i.e. the maximal simulated analysis period of 100 MLC was used to compute the probability of mDE. No systematic deviations of the simulations from the model are

apparent (see Figure 10 a)). Similarly, average photstability times τ_{ph} estimated by fitting the sum of 200 simulated intensity traces with a monoexponential decay are in agreement with the simulated parameters (see Figure 10 b)). The simulated τ_{ph} span the range of 10 MLC to 400 MLC corresponding to 0.5 s to 20 s, photobleaching time scales typical in experiments.

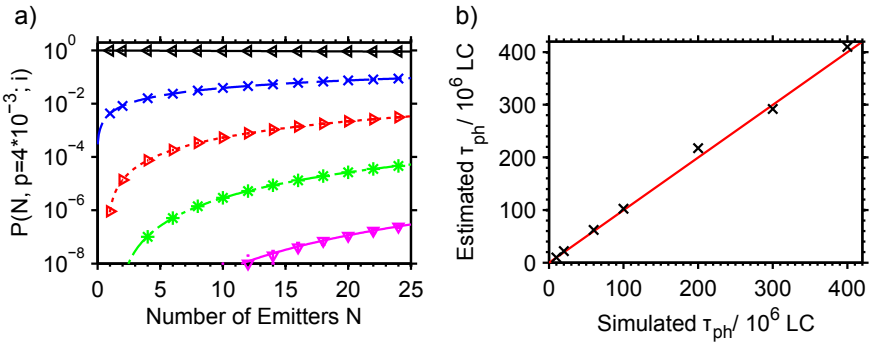

FIGURE 10: Verification of Simulations. a) Comparison of mDE from simulated data (symbols indicate the median with the lower and upper quartiles as error bars; the error is very small) with the CoPS model supplied with simulation parameters $p = 4 \times 10^{-3}$ and $p_b = 3 \times 10^{-4}$ (lines). Black left-pointing triangles i = 0, blue crosses i = 1, red right-pointing triangles i = 2, green asterisks i = 3, magenta downward-pointing triangle i = 4. b) Comparison of average photostability times τ_{ph} (black crosses) estimated by fitting the sum of 200 simulated intensity traces with a monoexponential decay and the simulated τ_{ph} parameters. The red line indicates the true, simulated photostability times. Additional simulation parameters were $p = 4 \times 10^{-3}$ and $p_b = 3 \times 10^{-4}$.

Since I considered the ideal case of N identical emitters that have the same brightness without any variation over time, I was wondering how noticeable the discrepancies between real experiments and simulations were. Figure 11 shows the intensity of a simulated trace with $N = 4$ together with three exemplary traces from an experiment with $N = 4$ and comparable brightness. It is not surprising that the experimental data reveals variation in the mean intensities and, in general, a higher variance of the fluorescence intensity over time (here: up to twofold interquartile range of the intensity distribution).

In the following, I simulated four independent emitters and varied their brightness and photostability to mimick the DNA probe with four labeling sites that was used in experiments in Section 5.2. Simulations conveniently allow the separation of the two parameters while they are inadvertently connected in experiments. To test if the results

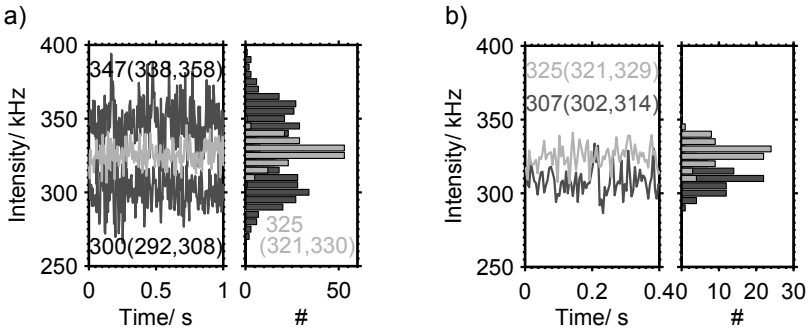

FIGURE 11: Comparison of Simulations and Experiment. Graphs display the intensity over time and the intensity histogram along with its quantiles (median($Q_{0.25}$, $Q_{0.75}$)). Simulation with $N = 4$, $p = 4 \times 10^{-3}$ and $p_b = 3 \times 10^{-4}$ assuming laser repetition at 20 MHz in light grey and experiments with the tetraAtto633 probe at 10 µW laser excitation power at 640 nm and laser repetition rate of 20 MHz in dark grey (for details see Section 5.2). a) and b) Experimental traces with higher and comparable intensity fluctuation than the simulated trace.

hold regardless of the label number, I varied the number of emitters for a value of molecular brightness representative for experiments.

5.1.1 *Four Labels with Varying Brightness*

As a first step, I simulated 4 labels without photobleaching and varied the fluorophore brightness for $p = 0.5$, 1, 2, 4, 6, 8 and 10×10^{-3} and the background level for $p_b = 0.5$, 1, 2, 3, 4, 5 and 6×10^{-3}. This extends slightly below and above the experimentally covered range of detection probabilities.

CoPS analysis was performed on all simulated data spanning an analysis period range of more than two orders of magnitude from 0.1 MLC to 40 MLC or 5 ms to 2 s. It should be noted that the simulated background detection probabilities were used in the fit (compare Section 12.8). In Figure 12 a) the estimated label numbers are displayed for a simulated brightness with $p = 1 \times 10^{-3}$, slightly lower than in the very first experimental demonstration of CoPS [146], and for the highest simulated brightness with $p = 10 \times 10^{-3}$. The results for all simulations can be found in Figure A.2. The estimated label number initially rises with increasing analysis period and then levels off around the simulated label number $N = 4$.

Figure 12 b) illustrates the influence of rising fluorophore brightness on the saturation-like dependance of label number estimates on increasing analysis period. The label number estimate at the shortest analysis period rises for higher detection probabilities and the true,

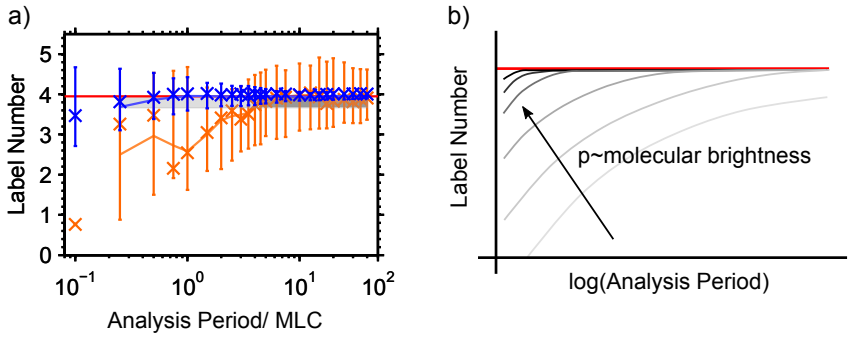

FIGURE 12: Simulations with $N = 4$ and varying brightness. a) Estimated label numbers (median with $Q_{0.25}$ and $Q_{0.75}$) for CoPS analysis with varying analysis period in orange/blue for simulated $p = 1 \times 10^{-3}/10 \times 10^{-3}$ and $p_b = 1 \times 10^{-4}/6 \times 10^{-4}$. The orange/blue line is the three point moving average of label number estimates and the plateau of valid CoPS estimates is shaded in dark grey/light grey. The red line indicates the simulated label number $N = 4$. b) Scheme of estimated label numbers for CoPS analysis with varying analysis period and varying brightness.

simulated label number is approached already at shorter analysis periods. However, CoPS can deliver valid label number estimates for all simulated data if the analysis period is chosen accordingly. In order to identify this plateau of stable CoPS estimates, an arbitrary definition of what is still accepted as a 'good' estimate has to be made. Here, label number estimates that fall within 5 % of the mean saturation level are considered valid. In practice, the maximum of the three point moving average (MA_{max}) of label number estimates is determined. It is further assumed that this MA_{max} lies 2.5 % above the mean saturation level, i.e. all CoPS estimates with MA $\geq$ 92.5 % MA_{max} are considered part of the plateau. In principle, the simulated label number could have served as a benchmark, but plateau identification was intended both for simulations and experiments and the true label number in experiments is generally unknown.

One may use the variation of label number estimates as a second quality criterion for CoPS analysis. Figure 13 highlights the increase in precision of label number estimates in the plateau with increasing analysis period. Here, we define the precision as half the interquartile range (see Equation 14), a robust measure of scale. The precision of the data with highest brightness is better than 20 % of the simulated label number even at analysis periods as short as 0.25 MLC or 12.5 ms. For $p = 1 \times 10^{-3}$, this threshold is only passed for a fraction of anal-

ysis periods. In general, the precision increases as the analysis period becomes larger (compare Figure A.3).

$$\text{precision} = \frac{IQR}{2} = \frac{Q_{0.75} - Q_{0.25}}{2} \tag{14}$$

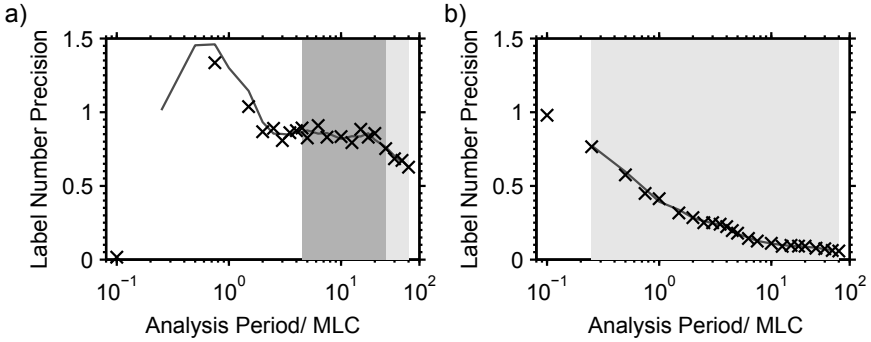

FIGURE 13: Precision of label number estimates for simulations with $N = 4$ and varying brightness. a)/ b) Precision for simulations with $p = 1 \times 10^{-3}/10 \times 10^{-3}$ and $p = 1 \times 10^{-4}/6 \times 10^{-4}$ with varying analysis period. The plateau of valid CoPS estimates is shaded in dark grey and a precision $\frac{IQR}{2} \leq 20\,\%$ of simulated N is indicated in light grey.

The optimal analysis periods for CoPS change tremendously with fluorophore brightness as can be seen in Figure 14 a). Valid label number estimates are achieved already after 0.25 MLC or 12.5 ms of simulation for the highest simulated brightness of $p = 10 \times 10^{-3}$, but only after 4.5 MLC or 225 ms for ten times dimmer fluorophores. The simulations for the lowest brightness with $p = 0.5 \times 10^{-3}$ had to be extended because the plateau of valid CoPS estimates was only reached from analysis periods of 100 MLC or 5 s on. These analysis periods are no longer practical for experiments when a large number of single molecule measurements are made. The minimum analysis period displayes a highly non-linear dependence on the detection probability. The same is true for the label number precision of valid CoPS estimates that becomes more precise with increasing p as shown in Figure 14 b), excluding the simulations for $p = 0.5 \times 10^{-3}$. Both tendencies can be explained by the nonlinear dependency of multiple detection events on p already mentioned previously. The mean label number precision increases with increasing brightness from 30 % down to 5 %. For the highest simulated detection probability $p = 10 \times 10^{-3}$, the variance of label number estimates was much reduced and a precision better than 2 % was reached at the maximum analysis period of 2 s.

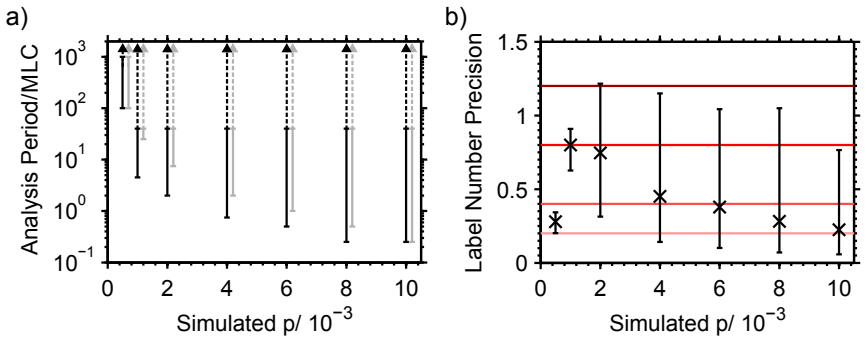

FIGURE 14: CoPS analysis providing valid label number estimates for simulations with varying brightness. a) The range of analysis periods for valid label number estimates (black) and for label number precision better than 20 % of simulated N (grey). The upper bar indicates the length of the simulated traces. b) Mean label number precision with errors indicating the extreme values. 30 %, 20 %, 10 % and 5 % of simulated N are displayed as horizontal lines in decreasing shades of red.

To conclude, CoPS delivers valid label number and brightness estimates for simulations with $N = 4$ and detection probabilities spanning more than an order of magnitude. In general, the precision of label number estimates increases with the analysis period and with the simulated fluorophore brightness. While the optimal analysis periods differ considerably from several tens of milliseconds to seconds, label number and detection probabilities in the plateau of 'good' CoPS estimates agree well with the simulated parameters (see Figure A.1) in all considered cases.

5.1.2 *Optimal Analysis Times Are Independent of Label Numbers*

The simulations with varying brightness were performed for the fixed label number $N = 4$, mimicking the experimental situation presented in Section 5.2. They could show that both the optimal analysis times for valid CoPS estimates and the achievable precision are determined by the fluorophore brightness. To test if the observed characteristics of CoPS estimates depend on the label number, a set of simulations with constant brightness ($p = 4 \times 10^{-3}$ and $p_b = 3 \times 10^{-4}$), representative of experimental conditions, and varying label number (N = 1, 4, 8, 12, 16, 20 and 24) was performed. The label numbers were chosen to match previous successfull experiments with DNA origami standards, so that those may serve as additional comparison. In principle, the label number range could be extended further.

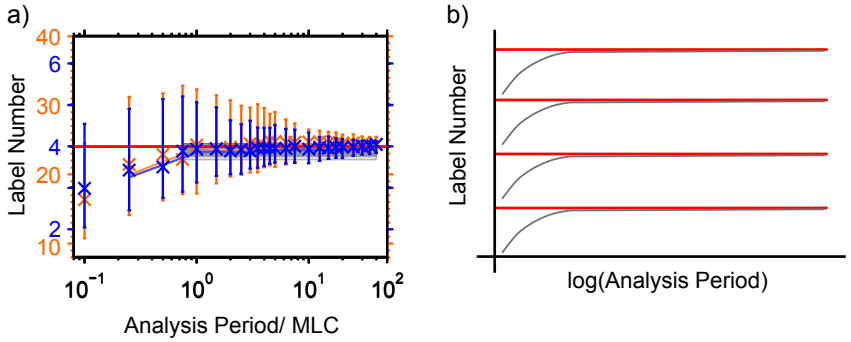

FIGURE 15: Simulations with constant brightness and varying label number. a) Estimated label numbers (median with $Q_{0.25}$ and $Q_{0.75}$) for CoPS analysis with varying analysis period in orange/blue for simulated $N = 24/4$, $p = 4 \times 10^{-3}$ and $p_b = 3 \times 10^{-4}$. The orange/blue line is the three point moving average of label number estimates and the plateau of valid CoPS estimates is shaded in dark grey/light grey. The red line indicates the simulated label number. b) Scheme of estimated label numbers for CoPS analysis with varying analysis period and varying label number.

CoPS analysis was performed on all the simulated data using exactly the same procedure as explained in detail above. In Figure 15 a), the estimated label numbers for $N = 4$ and $N = 24$ are displayed. The results for all simulations can be found in Figure A.5. As illustrated in Figure 15 b), the estimates follow the same trend regardless of absolute numbers when the analysis period is varied. In fact, the two 'experimental' graphs can be almost perfectly superimposed.

A closer look at the location of the plateau of valid label number estimates reveals that the minimal analysis period does not change significantly with the simulated label number (see Figure 16 a)). It varies around 0.75 MLC only to adjacent evaluated analysis periods and no pattern is apparent. There may be a slight increase with label numbers when a precision of at least 20 % is required. However, this change is negligable compared to the change of optimal analysis periods with brightness described in Section 5.1.1. The mean and best relative precision of valid label number estimates remains roughly constant around 15 % and 5 % across the simulated label number range (see Figure 16 b)). The worst obtained precision does not considerably exceed 30 %.

Exempt from this general trend are the label number estimates for $N = 1$ that show higher mean precision of about 4 %, with the best and worst precision reaching just below 2 % and 10 %, respectively. This is reasonable because the main contribution to photon statistics for $N = 1$ are single photon detection events that have the least rel-

ative error of mDE measurements. Occurence of mDE with i = 2 are due to coincidence with background photons. Since the simulated background detection probability is used as input parameter for CoPS analysis, modelling of the full photon statistics results in less variation of estimated parameters.

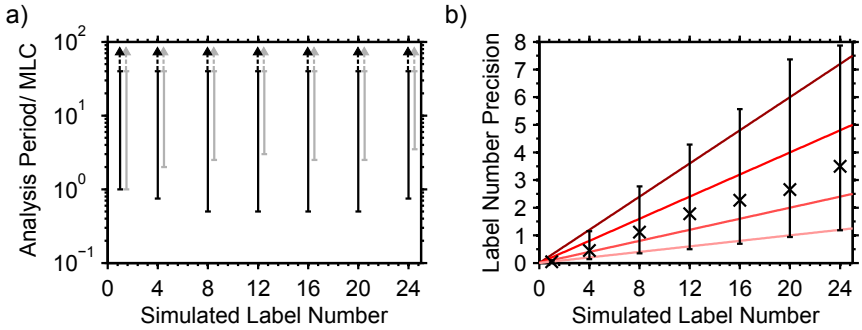

FIGURE 16: Summary of CoPS analysis providing valid label number estimates for simulations with varying label number. a) The range of analysis periods for valid label number estimates (black) and for label number precision better than 20 % of simulated N (grey). The upper bar indicates the length of the simulated traces. d) Mean label number precision with errors indicating the extrem values. 30 %, 20 %, 10 % and 5 % of simulated N are indicated as lines of decreasing shades of red.

A comparison of mean 'good' CoPS parameter estimates in Figure A.6 with the simulated parameters confirms the consistent quality of CoPS analysis across the simulated label number range of $N = 1$ to 24. This finding is in accordance with our previous measurements with DNA origami with 6, 12 and 18 Atto647N dyes [148]. Although the estimated label numbers were slightly higher than the experimentally designed dye number, this relative bias appeared constant over the tested number range and so did the relative variance of label number estimates.

For a full confirmation of unchanging characteristics of CoPS estimates with varying label numbers, simulations for different brightness values should be provided. However, the results for the experimentally relevant fluorophore brightness presented here suggest that the optimal analysis parameters are mainly independant of the label number.

5.1.3 *Four Labels with Varying Photostability*

In the simulations shown in Section 5.1.1, I could show that the minimum analysis period for CoPS analysis and the precision of la-

bel number estimates varies considerably with fluorophore brightness. Extension of the analysis period led to better statistics of the measured multiple photon detection events and eventually to an improved precision of CoPS estimates. In real experiments, fluorescence quantification is hampered by photobleaching and the measurement cannot be prolongued infinitely.

Next, I simulated constant brightness ($p = 4 \times 10^{-3}$ and $p_b = 3 \times 10^{-4}$) and a label number of $N = 4$, again representative of experimental conditions, and included photobleaching in the simulation. Photobleaching times were assumed to follow an exponential decay with a single average photostability time constant τ_{ph}. Photostability was varied from τ_{ph} = 10 MLC, 20 MLC, 60 MLC, 100 MLC, 200 MLC, 300 MLC and 400 MLC or 0.5 s, 1 s, 3 s, 5 s, 10 s, 15 s and 20 s, a range also observed in experiments (see Section 5.2 and Chapter 6). The simulations correspond to different fluorophores with the same brightness, but increasing photostability.

CoPS analysis was performed on all the simulated data, again using exactly the same procedure as explained in detail above. The intensities shown in Figure A.7 reflect the change in simulated photostability. For the small τ_{ph}, a clear decrease in intensity due to photobleached labels can be seen whereas for higher simulated photostability, the intensity appears almost constant over the analyzed range of analysis periods. In Figure 17 a), the estimated label numbers for $\tau_{ph} = 10$ MLC or 0.5 s and for $\tau_{ph} = 400$ MLC or 20 s are displayed. The results for all simulations can be found in Figure A.8. As illustrated in Figure 17 b), the label number estimates initially rise and then fall again depending on the photostability.

For very high photostability as in Figure 17 a) with $\tau_{ph} = 400$ MLC or 20 s, $\tau_{ph} \gg$ analysis period over the whole range of analysis periods. Photobleaching is then negligable for all analysis and label number estimates are very similar to those of the simulation without photobleaching (see Figure 15 a) for $N = 4$). The effect of increasing photobleaching is depicted in Figure 17 b). On the one hand, label number estimates are rising for short analysis periods due to increasing photon statistics and on the other hand, they are declining for longer analysis periods due to photodestruction. This leads to an intermediate plateau of valid label number estimates if photobleaching is not severe. The plateau is truncated further the more the labels are prone to photobleaching until CoPs estimates no longer approach the true, simulated label number. This transition can be observed for the simulation with $\tau_{ph} = 10$ MLC or 0.5 s in Figure 17 a). Only the maximum label number estimate lies just within 5 % of $N = 4$. The three point moving average is already lowered and the mean label number

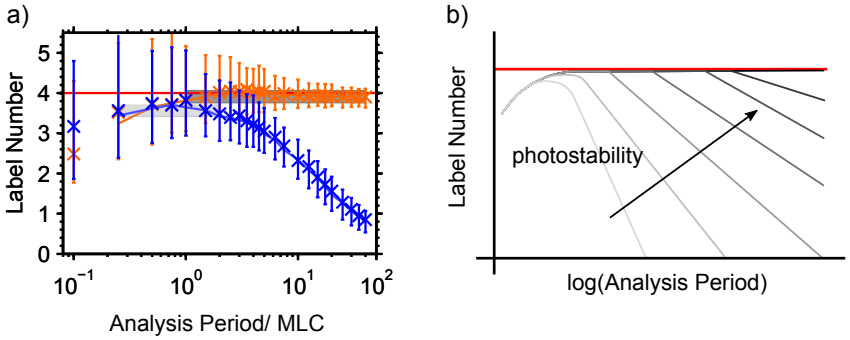

FIGURE 17: Simulations with constant brightness and varying photostability. a) Estimated label numbers (median with $Q_{0.25}$ and $Q_{0.75}$) for CoPS analysis with varying analysis period in orange/blue for simulated $N = 4$, $p = 4 \times 10^{-3}$, $p_b = 3 \times 10^{-4}$ and $\tau_{ph} = 10\,\text{MLC}$, 400 MLC or 0.5 s, 20 s. The orange/blue line is the three point moving average of label number estimates and the plateau of valid CoPS estimates is shaded in dark grey/light grey. The red line indicates the simulated label number. b) Scheme of estimated label numbers for CoPS analysis with varying analysis period and varying photostability

estimate of the recognized, short plateau is further reduced (see Figure 18 c); the plateau no longer serves as a reliable identifier for valid CoPS estimates.

In Figure 18 a), the optimal analysis periods determined according to the criteria defined in Section 5.1.1 are indicated for varying average photostability times. One would anticipate the same minimal analysis periods regardless of photostability because all simulations were performed at the same brightness. In principle this is true, the minimum varies by one adjacent evaluated analysis period around the minimum analysis period without photobleaching. Only the minimum analysis periods for $\tau_{ph} = 10\,\text{MLC}$ and 20 MLC or 0.5 s and 1 s are lowered slighty more, presumably due to a lowered plateau in label number estimates. There is also no trend indicating a correlation between the analysis periods with a precision better than 20 % of the simulated label number and the simulated photostability. Furthermore, the maximum analysis period is rising with increasing τ_{ph}, as expected, until the longest evaluated analysis period is reached.

A closer look at the precision of label number estimates for varying photostability reveals that the mean and best precision are increasing with τ_{ph} (see Figure 18). This can be explained by the corresponding increase in maximum analysis period taking into account the accompanied gain in precision that was demonstrated before (see Figure 13).

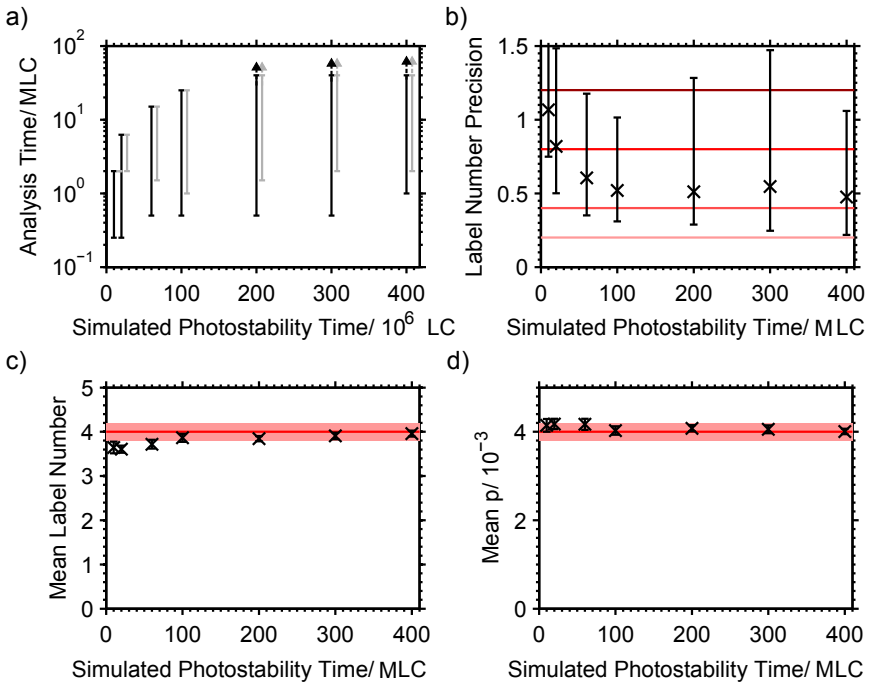

FIGURE 18: Summary of CoPS analysis with varying photostability. a) The range of analysis periods recognized as valid label number estimates (black) and for label number precision better than 20 % of simulated N (grey). The upper bar indicates the length of the simulated traces for the three largest simulated photostability times. d) Mean label number precision with errors indicating the extrem values. 30 %, 20 %, 10 % and 5 % of simulated N are indicated as horizontal lines of decreasing shades of red. c), d) Comparison of estimated (mean and standard deviation in the recognized plateau of label numbers) with simulated detection probabilities and label numbers. The red line indicates the simulated detection probabilities and label number, respectively, with a 10 % window shaded in light red.

The mean precision for the data with highest photostability is similar to that obtained without consideration of photobleaching.

Figure 18 c) and d) show that the analysis procedure results in lowered mean label numbers for very low photostability, but the estimated detection probability remains within 5 % of simulated p. It is presumably slightly elevated because of the reduced minimal analysis period. Judging from these overall mean CoPS estimates, it is not enough to identify a plateau in label number estimates to conclude that CoPS quantification reflects the true label number. This procedure is only reliable as long as photobleaching allows for a valid three point moving average maximum. Otherwise the label number in the plateau reflects a certain fraction of the true label number. However,

it should be possible to untangle this relation by considering a model for photobleaching, known average photobleaching times and known fluorophore brightness.

5.1.4 *Connecting the Minimum Photostability with Fluorophore Brightness*

Any fluorescence quantification is influenced by the inevitable photobleaching of fluorophores during data acquisition. The commonly used methods mentioned in Section 2.2 may even be categorized into actively photodestructing approaches like photobleaching step counting or single molecule localization microscopy and into minimally invasive techniques such as PCH analysis or CoPS. The extent of photobleaching greatly varies with the fluorophores that are used, their environment and with the excitation laser power. It is indeed possible to minimize photobleaching through a sensible choice of the mentioned parameters. Photostability may be greatly enhanced, e.g. by removing oxygen from buffer solutions and supplying a combination of reducing and oxidizing compounds [21, 154] or by the many commercially available antifading agents.

As shown by previous simulations in Section 5.1.3, photobleaching may be negligible for CoPS or it may lead to a reduced label number estimate. The impact of photobleaching depends on the relative magnitude of the average photostability time τ_{ph} and the necessary analysis period to obtain valid label number estimates. In the following, I aim at providing a guideline for the required photostability of fluorophores of a certain brightness.

I modeled photobleaching again as a process that can be described by a single parameter, the average photostability time τ_{ph}. The timepoints of fluorophore photobleaching were assumed to be distributed according to the monoexponential probability distribution function $\mathrm{pdf}(t, \tau_{ph})$ given in Equation 15. The probability for fluorophores to photobleach in a certain timespan Δt is then given by the cumulative distribution function $\mathrm{cdf}(\Delta t, \tau_{ph})$ (see Equation 16). In turn, the probability for fluorophores to still be fluorescent after Δt is $P(\Delta t, \tau_{ph}) = 1 - \mathrm{cdf}(\Delta t, \tau_{ph})$ (see Equation 17). Photobleaching of a pure N-mer leads to a distribution of label numbers k that can be described by a binomial distribution with fluorescence 'success' probability $P(\Delta t, \tau_{ph})$ (see Equation 18). Here, I focused on the average fraction of molecules that are still fluorescent after the CoPS analysis period (see Equation 19).

$$\mathrm{pdf}(t;\tau_{ph}) = \frac{1}{\tau_{ph}} \exp\left(-\frac{t}{\tau_{ph}}\right) \tag{15}$$

$$\begin{aligned}\mathrm{cdf}(\Delta t;\tau_{ph}) &= \int_0^{\Delta t} \mathrm{pdf}(t;\tau_{ph})\,\mathrm{d}t \\ &= 1 - \exp\left(-\frac{\Delta t}{\tau_{ph}}\right)\end{aligned} \tag{16}$$

$$P(\Delta t;\tau_{ph}) = 1 - \mathrm{cdf}(\Delta t;\tau_{ph}) = \exp\left(-\frac{\Delta t}{\tau_{ph}}\right) \tag{17}$$

$$\mathrm{b}(k;N,P(\Delta t;\tau_{ph})) = \binom{N}{k} \left(P(\Delta t;\tau_{ph})\right)^k \left(1 - P(\Delta t;\tau_{ph})\right)^{N-k} \tag{18}$$

$$\begin{aligned}\frac{\langle k\rangle}{N} &= P(\text{analysis period};\tau_{ph}) \\ &= \exp\left(-\frac{\text{analysis period}}{\tau_{ph}}\right)\end{aligned} \tag{19}$$

In Figure 19 a), the set of curves describes the fraction of fluorophores that resisted photobleaching for different CoPS analysis periods with varying average photostability times τ_{ph}. More than 90 % of fluorophores remain active if there is at least one order of magnitude difference between the selected analysis period and τ_{ph}. The inset shows that about 93 % of labels are still fluorescent after the minimal analysis period (0.75 MLC or 37.5 ms) needed to obtain valid CoPS estimates with $p = 4 \times 10^{-3}$ (see Section 5.1.1) and the lowest simulated photostability ($\tau_{ph} = 10$ MLC or 0.5 s) in Section 5.1.3. Already a sixfold increase in photostability to $\tau_{ph} = 60$ MLC or 3 s results in 99 % of remaining fluorophores. This explains, as expected, the differences in estimated label number in Figure 18 c). In turn, the necessary minimal average photostability time to guarantee a certain retained fraction of fluorophores (e.g. 95 % in Figure 19 b)) increases considerably with the duration of the analysis period.

In order to identify the minimum required photostability for a fluorophore of a particular brightness, I used the minimum analysis period that delivers valid CoPS label number estimates determined in Section 5.1.1 for different detection probabilities as a starting point. The minimal average photostability time $\tau_{ph,min}$ can then be calculated for different average fraction of molecules that are still fluorescent after this minimum CoPS analysis period (see Equation 20). This results in a highly nonlinear relation between the brightness and the required minimal photostability. The curves for different remaining fractions

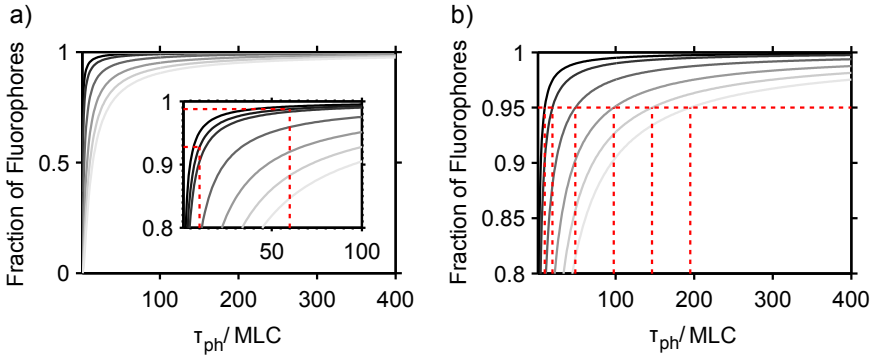

FIGURE 19: Modeling the fraction of surviving fluorophores. a) Fraction of remaining fluorescent labels after photobleaching for Δt = CoPS analysis period with varying average photostability time. Analysis period = 0.5 MLC, 1 MLC, 2.5 MLC, 5 MLC, 7.5 MLC and 10 MLC or 25 ms, 50 ms, 125 ms, 250 ms, 375 ms and 500 ms from dark grey to light grey. The inset contains in addition Δt = 0.75 MLC or 37.5 ms, the minimum analysis period for $p = 4 \times 10^{-3}$. The dotted red line indicates the fraction of remaining fluorescence for τ_{ph} = 10 MLC or 0.5 s and τ_{ph} = 60 MLC or 3 s. b) Same as a). The dotted red lines indicates the average photobleaching time τ_{ph} corresponding to 95 % remaining fluorescence for the set of curves.

of fluorophores in Figure 20 a) have an offset in $\tau_{ph,min}$ and slightly deviate from a straight line in this double logarithmic representation. The exact shape of the curves should be taken with care because just seven p values were sampled and, more importantly, the corresponding minimum analysis periods could only be determined to a certain analysis period grating by one set of simulations. Figure 20 b) illustrates the brightness-photostability parameter range that should be chosen to minimize the influence of photobleaching . Most of the simulated average photostability times in Section 5.1.3 with $p = 4 \times 10^{-3}$ lie close to or to the right of the 97.5 % line in Figure 20 a), thus photobleaching did not significantly impair CoPS analysis.

$$\tau_{ph,min}(\text{analysis period}_{min}(p), \frac{\langle k \rangle}{N}) = -\frac{\text{analysis period}_{min}(p)}{\ln(\frac{\langle k \rangle}{N})} \quad (20)$$

Fluorophore brightness and photostability can be easily characterized in a confocal microscope. In combination with the knowledge about minimum analysis periods, suitable dyes for CoPS can be readily identified using the relatively simple model of photobleaching presented here. If a fluorophore is prone to photobleaching and there is no alternative labeling option, the decrease in label number can be estimated and accounted for by the procedure described above.

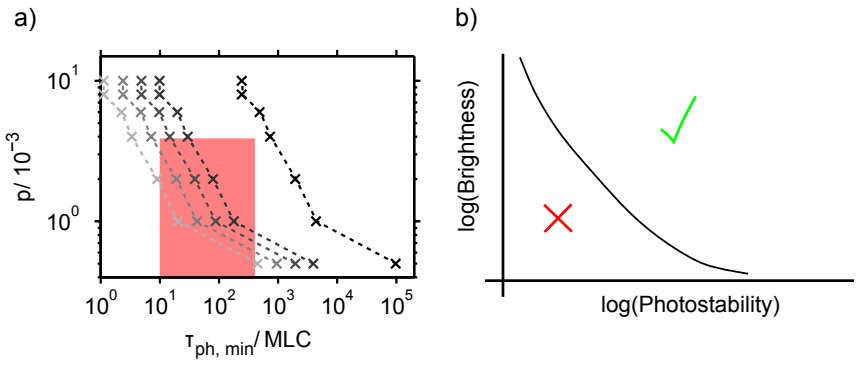

FIGURE 20: Fluorophore brightness and minimum required photostability. a) Simulated detection probability, i.e. fluorophore brightness, and corresponding minimum average photostability time τ_{ph} for a remaining fraction of fluorescent labels of 80 %, 90 %, 95 %, 97.5 % and 99.9 % from light grey to dark grey. Dotted lines connect the data points and the area shaded in light red indicates the range of simulated average photostability times in Section 5.1.3. b) Scheme of fluorophore brightness versus minimum photostability time for valid CoPS estimates. The green check mark and the red cross indicate the adequate and not suitable parameter range.

5.2 OPTIMAL COPS ANALYSIS IN EXPERIMENTS

Simulations have the advantage that all aspects of the data that is created can be controlled, i.e. the ground truth is known. For CoPS, this allowed testing the analysis for an ideal N-mer with a fixed label number, a defined detection probability and controlled photobleaching on demand (see Section 5.1). In the following, the findings of the simulations were tested in experiments. For this, I designed a double stranded DNA probe with four modified nucleotides that were incorporated in one of the single DNA strands (tetraProbe, see Figure 21 and Section 11.2). The nucleotides were then commercially labeled with fluorophores using the very efficient click-chemistry approach [155] and purified. The tetraProbe serves as a standard with a label number close to four with little variation due to the efficient labeling reaction. However, the true average label number is not known and, in general, there is variability in probe brightness. This is for instance reflected in the much higher variation of the mean intensity and the increased intensity fluctuations as compared to simulated data (see Figure 11, Figure A.4 and Figure A.12).

In the following, I conducted CoPS measurements using the tetraProbe labeled with Atto633 (tetraAtto633) and varying laser excitation power at 640 nm with a repetition rate of 20 MHz (2.5 µW, 5 µW,

10 µW and 20 µW; for details on the microscope settings, see Section 10.1). As a comparison, I also performed an experiment with the standard CoPS dye Atto647N (tetraAtto647N) and 20 µW laser excitation. Samples were prepared by immobilization of the tetraProbes under single molecule conditions (see Section 12.6). To enhance photostability and prevent blinking of the dyes a photostabilization buffer with enzymatic oxygen scavenging and reducing and oxidizing systems, termed ROXS Red, was used (for details, see Section 12.3). First a field of view was scanned at 5 µW laser excitation power, then individual probe molecules were localized and their photon emission statistics recorded. I measured and analyzed between ∼90 and 160 traces in total for each experiment (see Figure A.9). All experiments were conducted consecutively to prevent changes in microscope setup detection efficiencies.

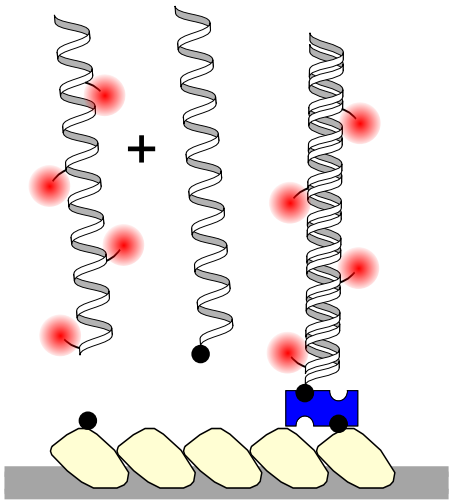

FIGURE 21: Scheme of tetraProbe with four labels. The dyes are coupled to four modified nucleotides in single stranded DNA. The tetraProbe is then formed by hybridization with the complementary biotinylated strand (black dot) and immobilized via streptavidin (blue) on a glass surface coated with BSA (beige) and biotinylated BSA (beige with black dot).

CoPS analysis was performed on the experimental data spanning the same analysis period range as for the analysis of simulations (0.1 MLC to 40 MLC or 5 ms to 2 s). Here, the background detection probabilities were estimated for each excitation laser power using the CoPS algorithm with $p_b = 0$ at the end of a trace when the fluorphores were photobleached. The resulting detection probabilities for estimated $N = 1$ of 5–20 traces were averaged and used as input parameter p_b for the analysis ($p_b = 1.2$, 2.0, 2.3 and 5.2×10^{-4} for

2.5 µW, 5 µW, 10 µW and 20 µW laser excitation power) (compare Section 12.8).

In Figure 22 a) the estimated label numbers are displayed for tetraAtto633 with 2.5 µW and 20 µW laser excitation power. Identification of the plateau of valid label number estimates was performed as described for the simulations (see Section 5.1.1). The results for all experiments can be found in Figure A.10. The estimated label number rises with increasing analysis period and then levels off at label numbers slightly below $N = 4$ for the measurements with low laser excitation power. For high laser excitation, the label number estimates start already at higher numbers and considerably increase only for the first two evaluated analysis periods. At larger analysis periods photobleaching results in a decrease of label numbers. This behaviour is illustrated in Figure 22 b) and can be explained by an increase in brightness and a decrease in photostability as a response of the fluorophores to increasing laser excitation power. The two parameters that could be controlled seperately in simulations are now inevitably connected in experiments.

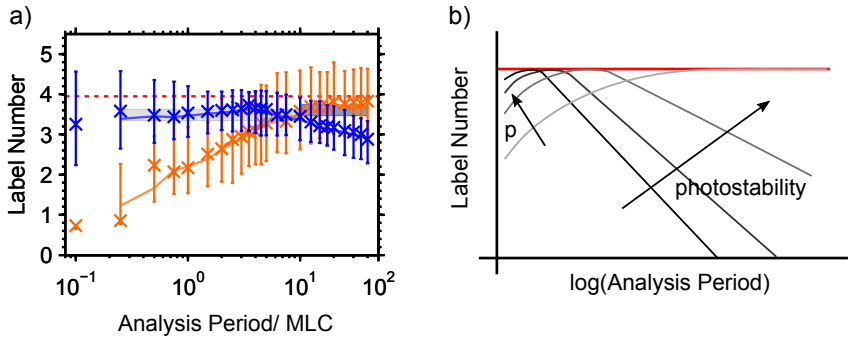

FIGURE 22: Experiments with tetraProbes and varying laser excitation power. a) Estimated label numbers (median with $Q_{0.25}$ and $Q_{0.75}$) for CoPS analysis with varying analysis period in orange/blue for tetraAtto633 measurements with 2.5 µW/20 µW laser excitation power at 640 nm and a repetition rate of 20 MHz. The orange/blue line is the three point moving average of label number estimates and the plateau of valid CoPS estimates is shaded in dark grey/light grey. The red line indicates the simulated label number. b) Scheme of estimated label numbers for CoPS analysis with varying analysis period and varying excitation power.

The estimated detection probabilities for the experiments are displayed in Figure 24 as a function of laser excitation power. The brightness for the measurements with Atto633 seems to linearly increase with the excitation laser power until fluorescence saturation starts to set in at higher laser powers. tetraAtto647N is brighter than

tetraAtto633 at 20 µW. Since the product of extinction coefficient and quantum yield is very similar for the two dyes, one would naively expect approximately equal brightness (see Table 8). Atto647N might be brighter under the chosen intense illumination conditions possibly due to less saturation effects as compared to Atto633.

I also characterized photobleaching of the dyes by manually identifying photobleaching steps and combining the resulting photostability times for the single fluorophores in histograms. The individual histograms were then modeled by a single exponential decay to estimate the average photostability lifetime τ_{ph} (see Figure B.19). The photostability for tetraAtto633 increased with decreasing laser excitation power as expected ($\tau_{ph} = 3.1(2)$ s at 20 µW, $\tau_{ph} = 11.2(3)$ s at 10 µW and $\tau_{ph} \gg 11.2$ s at laser excitation power $\ll$10 µW; the 95 % confidence intervals are given as error). I could not determine the photostability for the two measurements with the lowest excitation powers because the fluorophores were very photostable and sufficient statistics could not be acquired in a reasonable time. This high photostability explains the similarity of the tetraAtto633 measurements at 2.5 µW to the simulations of approximately the same brightness ($p = 1 \times 10^{-3}$) without photobleaching. The experiments also showed that Atto647N is more photostable ($\tau_{ph,20\mu W} = 8.6$ s (0.3 s)) than Atto633 under the same illumination conditions. This exceptional photostability of Atto647N is well known and is also demonstrated in later experiments Section 6.1.

The brightness-photostability parameters for both dyes that were used in the experiments already imply that they are indeed well suited for CoPS according to the criteria derived in the previous section (compare with Figure 20). Namely, the average photostability times are much higher than the minimal analysis periods that are required for the respective brightness according to simulations. Thus, photobleaching during the analysis period should not lead to a significant decrease in label numbers.

As a next step, I inspected the label number precision of the experimental data as second indicator for the quality of CoPS analysis. As already defined above, I used half the interquartile range as a robust measure for the precision (see Equation 14). The precision increases with the analysis period, but then levels off to about $\frac{IQR}{2} = 0.8$ and 0.5 for the measurements at the lower and higher laser powers (see Figure 23 and Figure A.11). This lower limit may reflect the variation of label numbers of the tetraProbes due to non-perfect labeling. Thus, I used the lowest obtained precision as a benchmark. Similar to the definition of the plateau of valid label number estimates, the minimum of the three point moving average of the precision was determined

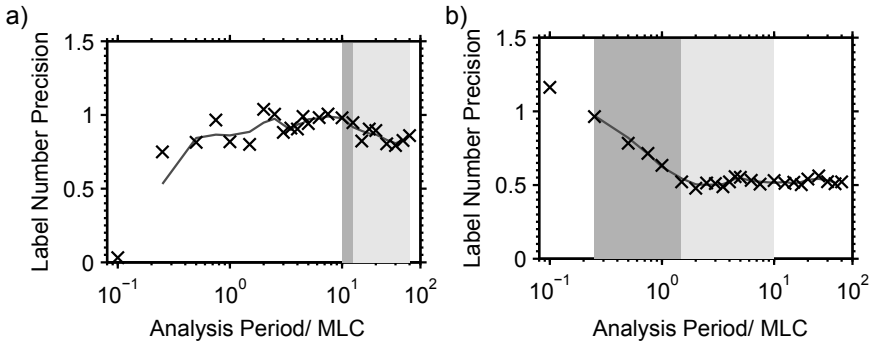

FIGURE 23: Precision of label number estimates for experiments with tetraPobes and varying laser excitation power. a)/ b) Precision for experiments with tetraAtto633 and 2.5 µW/20 µW laser excitation power at 640 nm and a repetition rate of 20 MHz with varying analysis period. The plateau of valid CoPS estimates is shaded in dark grey and a precision $\frac{IQR}{2}$ with MA $\leq$ 1.15 MA_{min} is indicated in light grey.

and all measurements with MA $\leq$ 1.15 MA_{min} were identified. Since the true average label number was unknown, it was not possible to use the same 20 % criterion as for the simulations.

Changes in variation of CoPS estimates could also be observed for time-resolved measurements of single tetraProbe molecules. Figure A.13 to Figure A.17 show that CoPS quantification with Atto633 and Atto647N allows following dynamic changes in emitter number as the labels are photobleaching. Here, the variation of label number estimates seems to decrease further for higher analysis periods even if the precision of the ensemble of measured tetraProbe molecules, described above, no longer does. This pureley reflects the increased precision of measured photon statistics at longer analysis periods.

The results of CoPS analysis for measurements with the tetraProbes and varying laser excitation power are summarized in Figure 18. The mean detection probabilities for the respective laser excitation power (see Figure 18 a)) are mainly used as reference for easier comparison with the simulations with varying brightness.

The minimum analysis period for valid label number estimates with the tetraAtto633 probe decreases with increasing brightness as expected (see Figure 24 b)). The maximum analysis periods for the two experiments with highest brightness deviate from the maximum evaluated analysis period and decrease with increasing brightness due to a notable decrease in photostability. When the precision criterion detailed above is enforced, all minimum analysis times are increased, but they still generally decrease with the brightness. The minimum analysis period for the Atto647N measurements deviates

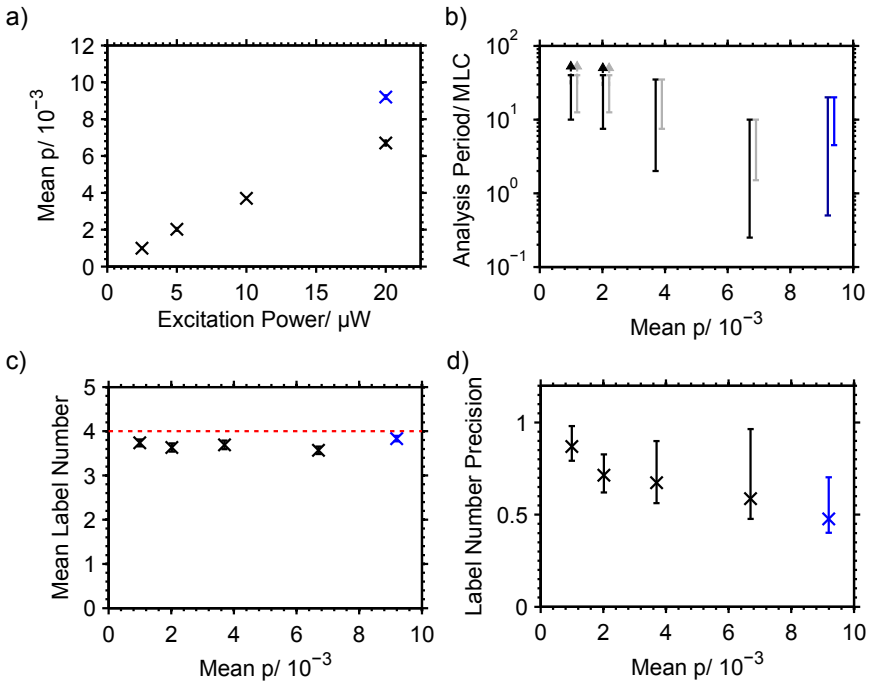

FIGURE 24: CoPS analysis providing valid label number estimates for experiments with tetraProbes and varying laser excitation power. All results for tetraAtto633 are indicated in black and for tetraAtto647N in blue. Laser excitation was at 640 nm with a repetition rate of 20 MHz. a) Estimated detection probabilities (mean and standard deviation of estimates in the recognized plateau of label number estimates) for different laser excitation powers. b) The range of analysis periods for valid label number estimates (dark) and for label number precision $\frac{IQR}{2}$ with MA $\leq$ 1.15 $\mathrm{MA}_{\mathrm{min}}$ (light). c) Comparison of estimated label numbers (mean and standard deviation of estimates in the recognized plateau of label number estimates) for different mean detection probabilities (laser excitation powers). The dotted red line indicates the designed label number $N = 4$. d) Mean label number precision with errors indicating the extrem values.

from that of the Atto633 measurmeents at the same laser power by one analysis period increment and the maximum analysis period is larger due to the higher photostability. It is not expected to obtain the exact same optimal analysis periods for the different dyes because the true variation of the label number and the photophysical heterogeneity of the dyes may be different. Also, the analysis periods are sampled at preselected, distinct intervals because computational time had to be considered. Still, results for minimum analysis periods for different dyes of the same brightness should conform within a certain error.

The mean and best label number precision of the tetraProbes increase from about $\frac{IQR}{2} = 0.9$ and 0.8 to about $\frac{IQR}{2} = 0.6$ and 0.45 for tetraAtto633 with increasing brightness and down to $\frac{IQR}{2} = 0.5$ and 0.4 for tetraAtto647N, much like it was shown for the simulations (see Figure 24 d) and Figure 14 b)).

The mean valid label number estimates for the tetraAtto633 probe in Figure 24 c) are all just below $N = 4$; these similar results are another indicator for correct label number estimation. All experimental findings substantiate that Atto633 is another suitable dye for Cops across the range of tested laser excitation powers, i.e. for almost an order of magnitude different fluorophore brightness and photostabilities.

A comparison of the results for experimental data with the simulations of varying brightness reveals that the minimum analysis period for measurements is at least as high as for the simulated data. Deviations are negligable at high brightness and tend to increase as the laser excitation power in experiments is lowered. This may be connected to static and dynamic heterogeneity of dye brightness in single tetraProbe molecules that increases the variance of photon statistics in the experimental data. As well, the measured distributions of CoPS parameter estimates are always a convolution of the probe molecules' distribution with the pure distribution of CoPS estimates for a perfectly homogeneous sample. This also affects the absolute precision of CoPS label number estimates which is about $\Delta N = 0.2$–0.3 worse than in the simulations.

When we experimentally investigated the counting range of CoPS [148] using DNA origami, we obtained similar minimal analysis periods as in the experiments with tetraAtto633. Then, the detection efficiency was $p \approx 2 \times 10^{-3}$ for 18 Atto647N dyes on DNA origami and saturation of label number estimates was reached for analysis periods $t_{acq} \geq 3\,\text{MLC}$ or 150 ms.

Overall, CoPS analysis of real experimental data displays the same features as revealed for simulated data in Section 5.1.

5.3 BRIGHTNESS AND PHOTOSTABILITY ARE DETERMINING

In this chapter, I performed simulations and experiments to investigate the influence of fluorophore brightness and photostablity on CoPS analysis. I focussed on a label number of four in the simulations since it matched the DNA based tetraProbe used in later experiments.

It turns out that CoPS delivers valid label number and brightness estimates for all tested detection probabilities as low as $p = 0.5 \times 10^{-3}$ and up to $p = 10 \times 10^{-3}$. The simulations confirmed that the precision of label number estimates increases with the analysis period and with the simulated fluorophore brightness, as expected.

However, the minimal analysis period for sensible CoPS estimates has a non-linear dependency on the brightness; it differs notably from several tens of milliseconds to seconds (see Figure A.1). This behaviour has not been revealed before. At the lowest simulated p, the minimum analysis period is in the seconds regime and no longer practical for measuremets of a large sample of single molecules. This marks a baseline for the brightness of fluorophores. It was also revealed that the time resolution for CoPS analysis of dynamic processes can be considerably higher than the previously established $\sim$2 MLC to 3 MLC or $\sim$100 ms to 150 ms [148, 156].

Results for an experimentally relevant fluorophore brightness suggest that the optimal analysis parameters are mainly independent of the label number. This is supported by our earlier measurements with DNA origami and 6, 12 or 18 Atto647N dyes [148]. For a full confirmation of unchanging characteristics of CoPS estimates with varying label numbers, simulations for different brightness values remain to be done.

CoPS analysis parameters can now be optimized either to reach maximum possible time resolution or maximum precision based on the newly gained insight. The label number precision increases with $\sqrt{\#\mathrm{LC}} \cdot p$ in limit of low $N \cdot p \ll 1$ [147]. It is therefore advisable to increase the molecular brightness rather than to measure at lower p and longer analysis period. This holds at least as long as the response of brightness and photostability to changes in excitation power remain antiproportional.

Photobleaching poses a natural upper limit to the analysis period t_{acq}. As long as the time to collect mDE statistics is much shorter than the average photostability time τ_{ph}, photobleaching can be neglected. In theory, 90 % of labels remain fluorescent if t_{acq} is an order of magnitude smaller than τ_{ph} for monoexponential photobleaching. Fluorophore brightness and photostability can be easily measured; knowing the minimum analysis period for a certain brightness, suitable

dyes for CoPS can be readily identified based on sufficient resistance to photodestruction during said time.

Overall, CoPS analysis of real experimental data displayed very similar behaviour as for simulated data. Here, brightness and photostability are inevitably connected and varied by changing the laser excitation power. The measured distributions of CoPS parameter estimates are always a convolution of the probe molecules' distribution with a distribution of CoPS estimates due to the fitting procedure. As well, static and dynamic heterogeneity of dye brightness in tetraProbe molecules probaby increases the variance of photon statistics in the experimental data. Therefore, minimal analysis periods were slightly higher and the absolute precision of CoPS label number estimates was about $\Delta N = 0.2 - -0.3$ worse than in the simulations. Atto633 proved sufficiently photostable at all brightness increments as did the standard CoPS dye Atto647N that was used for comparison at the highest illumination level. When we used DNA origami labeled with Atto647N to explore the counting range of CoPS [148], similar minimal analysis periods as in the experiments with tetraAtto633 were determined for the respective brightness.

The analysis of simulations and experiments in this chapter established criteria that render a dye suitable for CoPS. These guidelines can now be used to sort through the vast amount of available fluorophores. Based on a characterization of fluorophore brightness and photostability, I hope to identify several alternative labels compatible with CoPS.

6

ORGANIC DYES FOR COPS ACROSS THE VISIBLE SPECTRUM

Fluorescence quantification with CoPS in experiments prior to this study demonstrated the feasability of CoPS and characterized the accessible number range solely using the dye Atto647N and DNA based probes [146, 148]. Atto647N was selected for its superior brightness and its well known photophysical properties. In addition, use of an already established combination of enzymatic oxygen scavenging and reducing and oxidizing systems (ROXS) allowed for stable and long-lasting fluorescence emission.

Up to now, Atto647N is the spectroscopically ideal fluorophore for CoPS. However, specific counting applications might call for dyes with different properties, for example, excitation and emission wavelength, fluorescence lifetime, or cell permeability. Conceptually, there is no limitation in spectral parameters for CoPS. Identifying more suitable dyes for CoPS will greatly facilitate promoting this counting approach for applications. At the same time, possibilities for multiplexing will arise.

In the following, I screened fluorophores across the visible wavelength regime for applicability in CoPS and gained insight into differing fluorescence behavior. Specifically, the brightness and photostability were characterized to enable comparison between different dyes and to determine if the brightness-photostability parameters fall in the previously identified range of 'good´ CoPS conditions (see Chapter 5). *Most of the findings for the dyes in the red wavelength regime (see Section 6.1) were published in Grußmayer et al. [49]. The rationale of the next sections thus follows the argumentation given in the publication.*

For the CoPS experiments, a modular, double-stranded DNA probe, that is formed by a long fluorophore- and biotin-labeled single strand consisting of four repeats (termed REP_4) and by short fluorophore-labeled oligonucleotides (termed REP'), was used. Up to four REP' may hybridize to REP_4 to yield a DNA hybridization probe with a maximum of five fluorophores (see Figure 25 and Section 11.2). To achieve efficient hybridization and shift the label number distribution of probes to higher values, DNA hybridization probes were prepared with a REP' to REP_4 ratio of 20:1.

I selected dyes from different structural classes and with different fluorescent properties. The experiments were divided into three sets

according to the excitation wavelength and CoPS microscope settings. First, I explored fluorophores with spectra in the red wavelength region. In general, these candidates have high extinction coefficients and should be less prone to photobleaching than their counterparts in the green/yellow and blue/green part of the visible spectrum due to the lower energy of the absorbed photons [157].

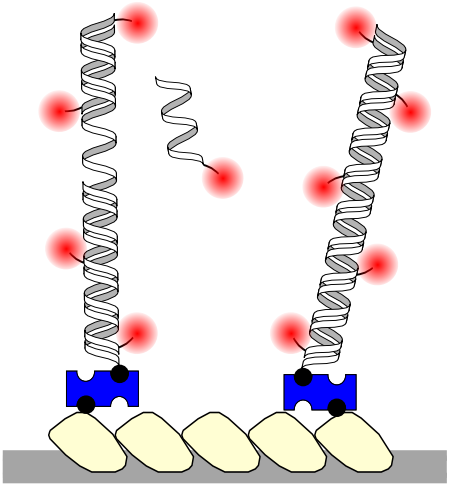

FIGURE 25: Scheme of DNA hybridization probe with up to five labels. Up to four small, labeled oligonucleotides may hybridize to a long, biotinylated and labeled DNA strand. The probes are immobilized via streptavidin (blue) on a glass surface coated with BSA (beige) and biotinylated BSA (beige with black dot).

6.1 THE RED WAVELENGTH REGIME

For the experiments in the red wavelength regime, I tested Atto633 (carborhodamine), Cy5 and AlexaFluor647 (further referred to as Alexa647; both indocarbocyanine dyes), AbberiorStar635 (rhodamine) and Silicon Rhodamine (further referred to as SiR; silicon rhodamine) in addition to Atto647N (carborhodamine) that was mainly used in prior CoPS experiments. While these organic dyes are spectrally very similar, they differ greatly e.g. in their fluorescence lifetime and hydrophobicity. The fluorescence properties are summarized in Table 4.

It should be noted that the experiments with all dyes but SiR were conducted consecutively in order to avoid changes in microscope detection efficiency. The SiR dye was brought to the attention of the single molecule and super resolution community only after I had already completed the initial measurement series [158, 159]. Its cell

permeability and potential fluorogenicity made it a very attractive choice of near-infrared dye for biological applications. For these reasons, I decided to perform additional experiments with SiR. The excitation pathway of the CoPS microscope was since modified and provided a reduced intensity at the laser focus for similar laser excitation power at almost identical excitation wavelength (640 nm in contrast to 635 nm). The fluorescence brightness of SiR was scaled for comparison with the remaining dyes by help of a reference measurement with Atto647N at the modified microscope setup.

The different DNA hybridization probes were immobilized at single molecule conditions using the same photostabilizing buffer (ROXS Red) for all dyes (see Section 12.6 and Section 12.3). The chosen buffer conditions prolonged photostability and completely prevented fast blinking events (∼millisecond off-time). Longer off-times occurred only sporadically (see Figure 26 a) at t∼3.2 s). To my knowledge, the dyes AbberiorStar635 and SiR have not been tested under ROXS conditions at the single molecule level before, whereas proper ROXS conditions for the remainder were known. At the microscope, a certain field of view was scanned, then the individual probe molecules were localized and CoPS photon statistics was subsequently acquired.

For each dye, one representative fluorescence intensity photobleaching trace and the label number estimates by CoPS are displayed in Figure 26. One could, in principle, estimate the brightness of the dyes from the mean intensities per photobleaching step. Since a coarse inspection of the data revealed that the brightness should be at least on the order of $p = 5 \times 10^{-3}$, an analysis period of $t_{acq} = 2.5$ MLC or 125 ms was chosen in accordance with the results for optimal CoPS analysis and previous publications (see Chapter 5 and [148]. The measurements of SiR with altered excitation showed lower brightness and higher photostability. To obtain dynamic CoPS estimates with similar variation in label number, I chose $t_{acq} =$ 10 MLC or 500 ms.

As expected from previous in-depth studies with ATTO647N, CoPS label number estimates dynamically follow the fluorescence intensity bleaching steps [146, 148]. The error bars for single estimates depicted in Figure 26 reflect the error estimation of an individual measurement based on the resampling method (see Section 12.8) [150, 151]. It should be distinguished from the CoPS error of number estimation that also includes the statistical variation among an ensemble of identical probe molecules [148]. The single trace data already indicates that the investigated dyes differ considerably in photostability. To put these findings on a broader statistical basis, I conducted CoPS mea-

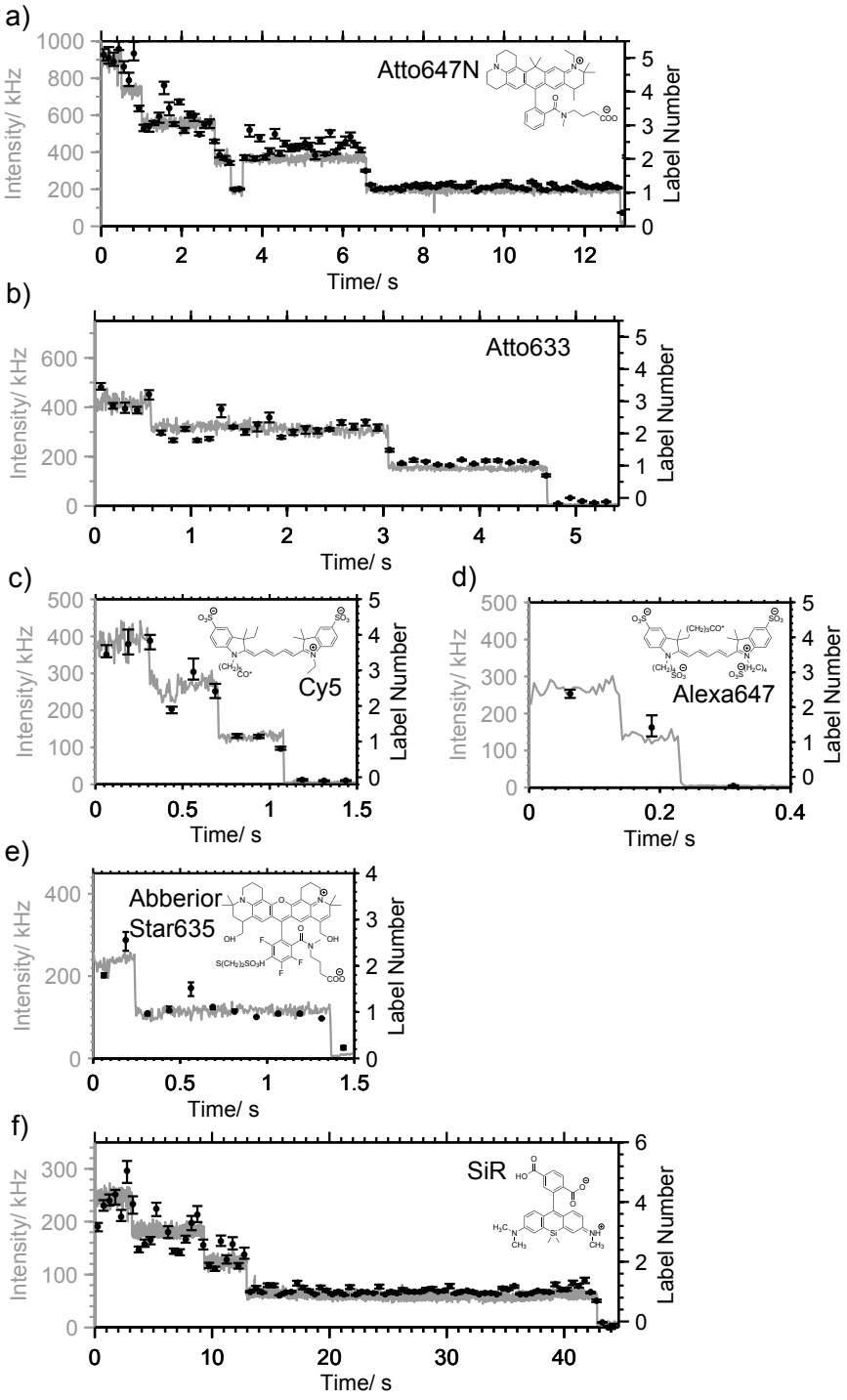

FIGURE 26: Single molecule CoPS analysis of DNA hybridization probes with dyes in the red wavelength regime. Modification of Figure 1 of [49]. a) Atto647N, b) Atto633, c) Cy5, d) Alexa647 and d) AbberiorStar635 with 10 µW laser excitation power at 635 nm and a repetition rate of 20 MHz. Time resolution (= analysis period τ_{acq}) of 2.5 MLC or 125 ms. f) SiR with 10 µW laser excitation power at 640 nm and a repetition rate of 20 MHz. Time resolution (= analysis period τ_{acq}) of 10 MLC or 500 ms. CoPS estimates correlate with intensity bleaching steps. Black: Label number estimates with error bars derived from resampling algorithm, grey: Intensity.

surements and analysis for many single DNA hybridization probes for each sample (N≥115, see Table 9) and performed photobleaching step analysis to determine the dye photostability.

For each sample, experiments were carried out at two different laser powers (5 µW and 10 µW). To minimize premature photobleaching, the field of view for localization of molecules was scanned at the lower laser excitation power. A survey of all data revealed that the brightness was expected to be at least about $p = 2 \times 10^{-3}$ except for SiR at 5 µW laser excitation power. Thus, the majority of data was directly subjected to CoPS analysis with an analysis period of $t_{acq} =$ 2.5 MLC or 125 ms. For simplicity, I chose one analysis period concurrend with results from previous publications and consistent with optimal CoPS analysis for the respective brightness (see Chapter 5 and [148]. In principle, one could use an even shorter analysis period for the first series of experiments at higher laser excitation power. The remaining measurements with SiR at half the laser excitation power were evaluated with $t_{acq} = 10$ MLC or 500 ms (compare Section 12.8).

The estimated detection probabilities for all samples rise with the laser excitation power as expected (see Figure 27). The increase in brightness is not always twofold due to fluorescence saturation effects mentioned earlier (see Section 5.2). Atto647N and Atto633, the two fluorophores that were already found suitable for CoPS in Section 5.2, have the highest brightness under the chosen measurement conditions. The relative magnitude of detection probabilities for the different fluorophores, including the scaled data for SiR, agrees well with the respective brightness calculated from fluorescence properties (see Table 8).

There is no obvious indicator that increased laser illumination results in CoPS analysis with reduced label number estimates due to photobleaching. The median of the label number distribution remains almost unchanged for most dyes. Only the DNA hybridization probes with Alexa647 and SiR display slightly lower label number estimates for higher excitation power. The respective label number distributions for all samples are shown in Figure B.21. Exactly identical distributions would only be expected for very large data sets and when photobleaching plays no role.

Photostability is one of the critical parameters for CoPS analysis (see Section 5.1.3 and Section 5.1.4) and was evaluated by manually identifying photobleaching steps (see for example, Figure 26 b) ∼0.6 s, 3 s and 4.7 s). The resulting photostability times for the single fluorophores were combined in histograms and modeled with a single exponential decay to estimate the average photostability lifetime (τ_{ph}; see Figure B.19 and Figure 27 c)). It turns out that out of the ini-

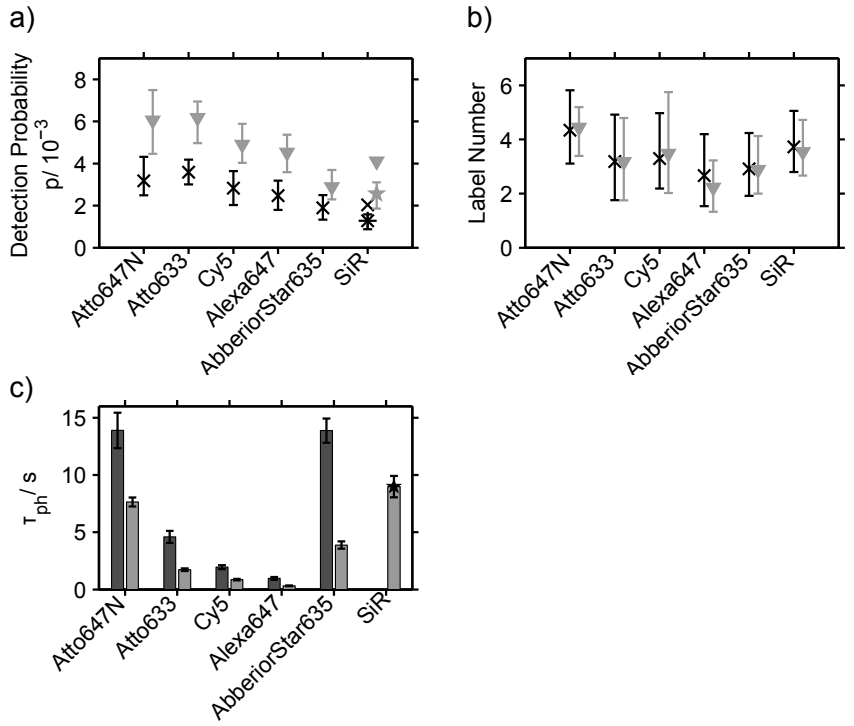

FIGURE 27: CoPS analysis of DNA hybridization probes with dyes in the red wavelength regime. Modification of Figure 2 of [49]. Black crosses/ light grey downward-pointing triangles: 5 µW/10 µW laser excitation power at 635 nm (640 nm for SiR (asterisk and star)) and a repetition rate of 20 MHz. a)/ b) Estimated detection probabilities/ label numbers (median with $Q_{0.25}$ and $Q_{0.75}$) for CoPS analysis with $t_{acq} = 2.5$ MLC or 125 ms ($t_{acq} = 10$ MLC or 500 ms for SiR with 5 µW). Scaled median detection probabilities for SiR (black cross and downward-pointing triangle). c) Average photostability lifetime τ_{ph} estimated by fitting a single-exponential decay to photostability time histograms derived from fluorescent traces. Errors indicate the 95 % confidence intervals of the fit parameter τ_{ph}.

tial experiment series at 635 nm laser excitation, Alexa647 is most prone to photobleaching, with photostabilities increasing in the order of Alexa647<Cy5<Atto633<AbberiorStar635≤Atto647N in agreement with previous reports [21]. The photostability of SiR at 10 µW was higher than for all other dyes; τ_{ph} could not even be determined at the lower laser illumination because the fluorophores were too photostable to accumulate sufficient statistics in a reasonable time. However, the corresponding brightness at the different illumination conditions was also reduced which resulted in a higher minimal analysis period. The timescale for photobleaching was one to two orders of magnitude longer than the applied analysis period for CoPS, except for Alexa647 at the higher laser excitation power.

All six tested dyes in the far-red wavelength regime seem suitable for CoPS. This significantly broadens the repertoire of available fluorophores for CoPS. It now comprises dyes that are frequently used for labeling of proteins in a biological context such as Cy5 or Alexa647 and even includes a cell permeable dye (SiR). If the application does not demand for specific properties, Atto647N is still the dye of choice due to its exceptional photostability at high brightness.

6.2 THE GREEN/ YELLOW WAVELENGTH REGIME

The following section is dedicated to experiments with dyes in the green/yellow wavelength regime. I chose Cy3B (bridged cyanine), Atto550, Atto565 and AttoRho6G (rhodamine), AlexaFluor532 (further referred to Alexa532, carborhodamine) and Atto532 (rhodamine) for test measurements. These dyes cover a wider spectral range and are ideally excited either with a 561 nm or a 532 nm laser (see Table 5).

The only available pulsed green laser had a wavelength of 532 nm. The laser power for Atto550 and Atto565 was thus adapted to compensate for the mismatch in laser excitation wavelength and to achieve comparable brightness of the dyes (see Table 10). Since the dyes differ considerably in their excitation and emission spectra, obtained brightness values would have been difficult to compare in any case.

The approach was the same as for the experiments with dyes in the red wavelength regime. Different DNA hybridization probes were immobilized at single molecule conditions using a photostabilizing buffer (see Section 12.6 and Section 12.3). Since the optimal ROXS buffer conditions were not known for all dyes, I screened six different buffers together with practical student Anne Schöffler [160]. We varied both the enzymatic oxygen scavenging system and the reducing and oxidizing agents. The best conditions for all dyes contained the protocatechuic acid and protocatechuate-3,4-dioxygenase system (= PCD) that has the advantage of causing almost no pH drop over the course of an experiment when the starting pH is close to 8. It also reaches lower oxygen concentrations than the common glucose, glucose oxidase and catalase system (= GOC) that I used in previous experiments[161, 162]. As redox components, a combination of methylviologen and propyl gallate worked well; only Cy3B showed a notable improvement using ascorbic acid instead of propyl gallate.

The chosen buffer conditions prolonged photostability, but complete control of photophysics could not be obtained in all cases (see Figure 28). Cy3B and Alexa532 were nicely stabilized except for rare, long off-times (∼seconds timescale). Atto550 and Atto565

displayed almost no fast blinking (∼millisecond off-time), but frequently entered a dimmer fluorescent states with time, which rendered identification of photobleaching steps difficult. Similar observations were made for other DNA constructs labeled with a single dye (personal communication D. Brox). For AttoRho6G on the other hand, fast blinking was not completely prevented, but the dye showed no other fluctuations in fluorescence intensity. Atto532 often presented residual, dim fluorescence at the end of intensity traces.

For each dye, one representative fluorescence intensity photobleaching trace and the label number estimates by CoPS are displayed in Figure 28. The laser excitation power was adjusted to obtain a brightness on the order of $p = 3 \times 10^{-3}$. However, Alexa532 and Atto532 were too prone to photobleaching at that brightness so that the laser power had to be lowered and only a brightness on the order of $p = 1 \times 10^{-3}$ to 2×10^{-3} was reached. The analysis periods for dynamic CoPS measurements were chosen as $t_{acq} = 10\,\text{MLC}$ or 500 ms for the dyes with a brightness in the same range as SiR (see Section 6.1). For the dimmer Alexa532 and Atto532, the analysis period was increased to $t_{acq} = 50\,\text{MLC}$ or 2.5 s to obtain a similar variation in label number as for the other dyes.

CoPS label number estimates dynamically follow the fluorescence intensity bleaching steps much like it was previously shown for dyes in the red wavelength regime (see Section 6.1 and [146, 148]). The error bars for single estimates depicted in Figure 26 again reflect the error estimation of an individual measurement based on the resampling method [150, 151] as explained in detail in Section 12.8. Not all steps can be resolved in the intensity photobleaching traces of Alexa532 and Atto532; CoPS estimates reasonable numbers for the Atto550 and Atto565 traces which would be very difficult by photobleaching step analysis due to very different brightness increments. It is also obvious that the photostability of the dyes that were studied differs considerably as indicated by the length of the exemplary traces in Figure 28.

As for the dyes in the red wavelength regime, I performed CoPS measurements of many single DNA hybridization probes for each sample at two different excitation powers (N≥107, see Table 11). To minimize premature photobleaching, the field of view for localization of molecules was scanned at the lower laser excitation power. At first, I started with 6 µW and 12 µW, conditions that corresponded to the same photon flux as for the dyes in the red wavelength regime. I chose only 6 µW for measurements with Alexa532 and Atto532 because either rapid photodestruction took place at higher laser excitation power or the brightness was marginal when illumination was

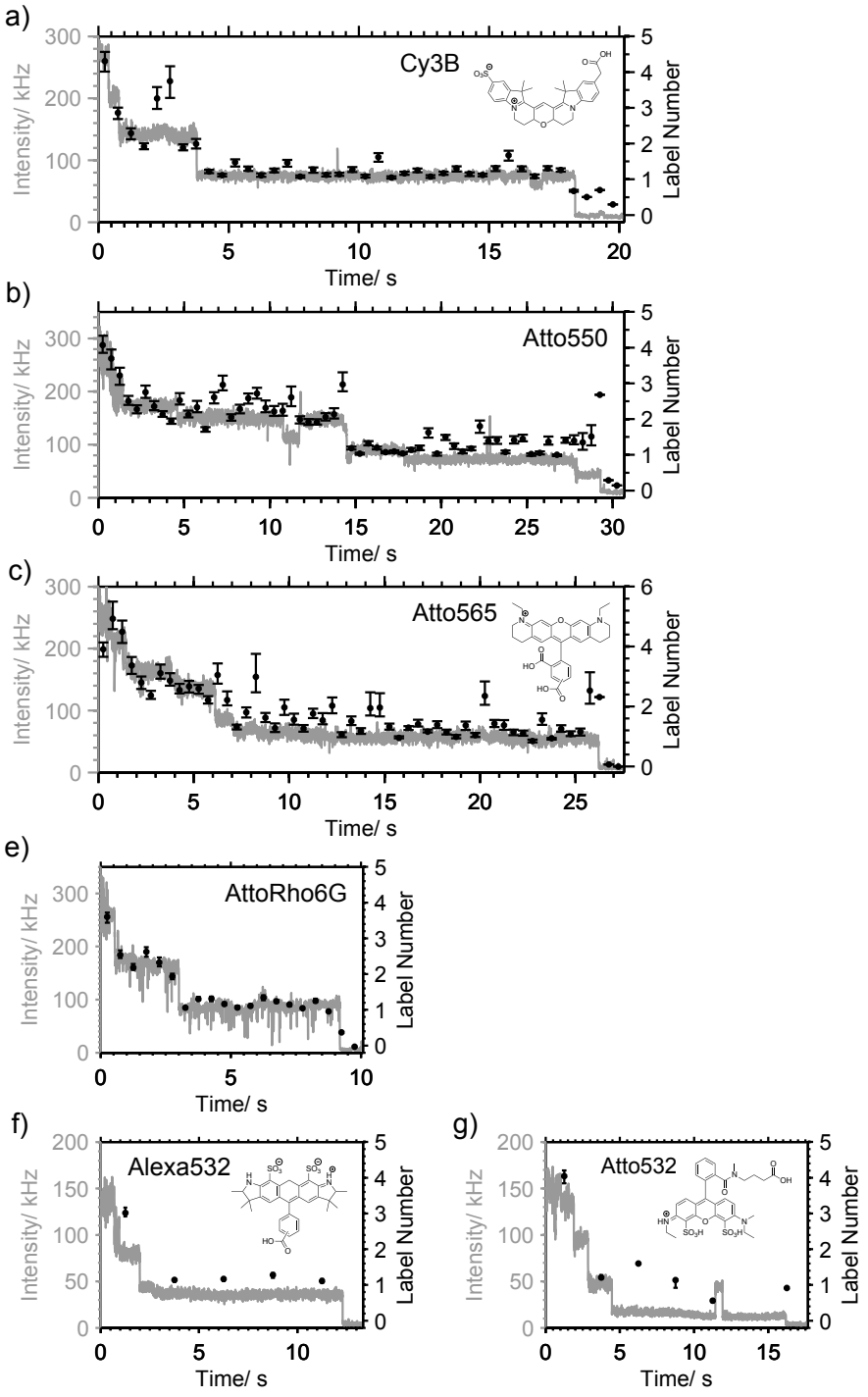

FIGURE 28: Single molecule CoPS analysis of DNA hybridization probes with dyes in the green/yellow wavelength regime. a) Cy3B, b) Atto550, c) Atto565, d) AttoRho6G, e) Alexa532 and f) Atto532 with e), f) 6 µW, a), d) 12 µW and b), c) 24 µW laser excitation power at 532 nm and a repetition rate of 20 MHz. Time resolution (= analysis period τ_{acq}) of 10 MLC or 500 ms for a)–d) and 50 MLC or 2.5 ms for e) and f).CoPS estimates correlate with intensity bleaching steps. Black: Label number estimates with error bars derived from resampling algorithm, grey: Intensity.

reduced. As mentioned above, Atto550 and Atto565 were poorly excited at 532 nm, so the laser excitation power was increased to 12 µW and 24 µW. A careful study of dye photostability completed the parameter set to judge eligibility of the dyes for CoPS.

As previously mentioned, the brightness can be estimated from the hight of individual photobleaching steps. An overview of all data revealed that the brightness was expected to be at least about $p = 2 \times 10^{-3}$ for the measurements at the higher laser excitation power. Thus, CoPS analysis was performed right away with an analysis period of $t_{acq} = 2.5$ MLC or 125 ms as for most of the data in the red wavelength regime. At the lower laser excitation power, the brightness was presumably between $p = 1 \times 10^{-3}$ to 2×10^{-3}. Consistent with optimal CoPS analysis for $p \geq 1 \times 10^{-3}$ (see Section 5.2), an analysis period of $t_{acq} = 10$ MLC or 500 ms was chosen as for evaluation of measurements for SiR at 5 µW.

The estimated detection probabilities for the samples increases almost twofold when the laser excitation power is doubled (see Figure 29 a)). The highest brightness under the chosen measurement conditions is reached by AttoRho6G with $\sim p = 3 \times 10^{-3}$ followed by Cy3B, Atto550 and Atto565. In fact, Cy3B reaches almost exactly the same brightness values as SiR although the product of its quantum yield and extinction coefficient at the excitation wavelength is higher (compare Table 10 and Table 8). For Alexa532 and Atto532 a detection probability of only about $p = 1.5 \times 10^{-3}$ was reached because the laser excitation power could not be increased due to severe photobleaching. In general, the measured brightness of the dyes in the green/yellow wavelength regime is lower than for those in the red. This can be explained in part by the sensitivity of the detectors that decreases with the detection wavelength in the visible spectrum; the peak quantum yield of the APDs lies around 700 nm [163]. In addition, measurements were performed at the CoPS setup with modified excitation pathway (and presumably more extended focus) as were the measurements with SiR (see Section 10.1 and Chapter 4).

The label number estimates corresponding to the just discussed detection probability estimates are displayed in Figure 29 b). The median of the label number distribution remains almost unchanged for Atto550 and Atto565. The DNA hybridization probes with Cy3B and AttoRho6G display slightly lower label number estimates for higher excitation power. Exactly identical distributions would only be expected for very large data sets and when photbleaching plays no role at all (compare Figure B.22). The results of photobleaching step analysis (data not shown) for the latter two dyes also shows a corresponding slight decrease in label numbers. Close to 50 % of the traces of

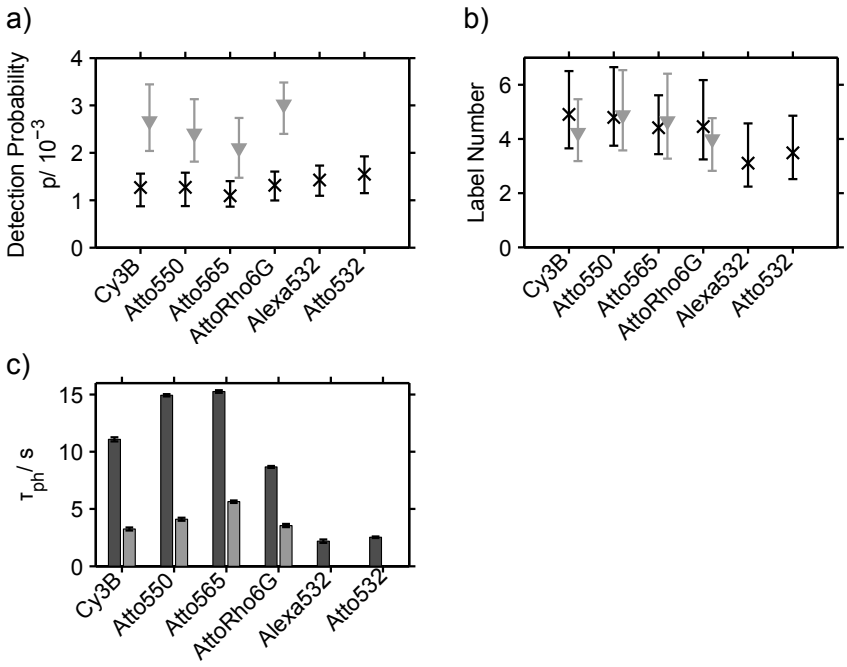

FIGURE 29: CoPS analysis of DNA hybridization probes with dyes in the green/yellow wavelength regime. Black crosses/ light grey downward-pointing triangles: low and high laser excitation power (6 µW and 12 µW for Cy3B, AttoRho6G, Alexa532 and Atto532, 12 µW and 24 µW for Atto550 and Atto565) at 532 nm and a repetition rate of 20 MHz. a)/ b) Estimated detection probabilities/ label numbers (median with $Q_{0.25}$ and $Q_{0.75}$) for CoPS analysis with $t_{acq} = 10$ MLC or 500 ms for low and $t_{acq} = 2.5$ MLC or 125 ms for high laser excitation power. c) Average photostability lifetime τ_{ph} estimated by fitting a single-exponential decay to photostability time histograms derived from fluorescent traces. Errors indicate the 95 % confidence intervals of the fit parameter τ_{ph}.

the former two dyes could not be evaluated for photobleaching step analysis; they displayed greatly varying step sizes and appeared to enter dim states with time as mentioned above (see Figure 28 b) and c)). This variation in dye brightness could potentially influence CoPS analysis of the ensemble of traces if it occured during the first analysis period. Sorting the traces revealed that the detection probability for all traces of Atto550 and Atto565 is somewhat reduced as compared to those with clear photobleaching steps (see Figure B.23). This effect is only on the order of $\Delta p = 0.1$; it may be due to the difference in photophysics of the underlying data or simply occur because of different positioning of the probe molecules in the focus of the microscope. The corresponding label number estimates show the opposite trend that could as well result from true differences in label numbers of the subset of probe molecules. This question of influence of photo-

physics on CoPS analysis could be answered by measurements of a more defined sample, say a tetraProbe as used in Section 5.2.

As emphasized earlier, photostability is a critical parameter for CoPS analysis (see Section 5.1.3 and Section 5.1.4) and was evaluated by manually identifying the time of photobleaching of individual dyes. Here, only the traces with clearly identifiable photobleaching steps were used. The resulting photostability times for the single fluorophores were combined in histograms and modeled with a single exponential decay to estimate the average photostability lifetime (τ_{ph}; see Figure B.19 and Figure 29 c)), exactly as for the dyes in the red wavelength regime. Atto565 and Atto550 are most photostable, with photostabilities decreasing in the order of Atto565$\geq$Atto550>Cy3B>AttoRho6G$\gg$Atto532$\geq$Alexa532. The timescale of photobleaching are one to two orders of magnitude higher than the minimal analysis period except for the measurements with Alexa532 and Atto532.

As previously mentioned, Cy3B has almost identical detection probabilities as SiR in the red wavelength regime. The photostability at the higher laser power of SiR is about three times that of the corresponding Cy3B measurement and, in fact, similar to that of Cy3B at the lower laser power (and half the brightness). It has to be noted, though, that the sensitivity of the APD in the green/yellow wavelength regime is only about 90 % of that in the red. Atto647N, the most photostable red dye, has similar or higher average photostability times than all dyes in the green/yellow wavelength regime at the respective measurement conditions despite an at least twofold increase in brightness.

The measurements show that CoPS is, in general, feasible in the green/yellow wavelength regime. Out of the tested dyes, Cy3B seems most suitable for its ´clean‘ photophysics and relatively high photostability. Measurements with Alexa532 and Atto532 should be avoided due to their low photostability and low brightness. The green dyes have a worse balance between brightness and photostability than the red dyes. Wherever applicable, red dyes should be preferred for CoPS. Altogether, I showed for the first time that CoPS is possible in a second wavelength channel. This opens up exciting perspectives for two-color counting experiments with organic dyes as fluorescent labels.

6.3 THE BLUE/ GREEN WAVELENGTH REGIME

I also investigated dyes with spectra in the blue/green wavelength regime, namely Atto488 (rhodamine), Alexa488 (rhodamine), OregonGreen488 and OregonGreen514 (both fluorinated fluorescein)

using the DNA hybridization probe. These dyes at lower wavelengths are generally the least photostable, have lower extinction coefficients and generally higher fluorescence quantum yields than the dyes in the green/yellow and red wavelength regime (compare Table 4, Table 5 and Table 6). The four organic dyes are spectrally similar and even have similar fluorescence lifetime. However, the OregonGreen dyes are more sensitive to changes in pH. The fluorescence properties are summarized in Table 6. The available pulsed blue laser at 470 nm unfortunately does not optimally excite the dyes, which further reduces the expected brightness (see Table 12). Still, it would be beneficial to identify suitable dyes for a third color option for CoPS.

I discovered that I could not use the glucose, glucose oxidase and catalase system (= GOC) that is part of ROXS Red for oxygen scavenging, since both enzymes employ colorful cofactors (flavin adenine dinucleotide and a heme group, respectively) that lead to increased fluorescence background that interferes with CoPS analysis when excited at 470 nm. As an alternative I chose the protocatechuic acid and protocatechuate-3, 4-dioxygenase system (= PCD) mentioned above that was previously reported to work with Alexa488 [161]. I also screened different antifading media including Mowiol with 1,4-diazabicyclo[2.2.2]octane (DABCO) and Vectashield (data not shown) [157], but found that a combination of PCD with 1 mM methylviologen (MV) and 1 mM ascorbic acid (AA), termed ROXS Blue MV/AA, greatly reduces fast blinking (∼millisecond off-time) and further prolonges dye photostabilities (for details refer to Section 12.3). It should be noted that protocatechuic acid itself may act as reducing agent [164]

As illustrated in Figure 30, CoPS analysis is in principle possible in the blue/green wavelength regime. I observed a reduced brightness with respect to measurements with all dyes in the red and green/yellow wavelength regime at comparable excitation photon flux. This is due to the inferior properties of the dyes and because the sensitivity of the APD detectors for 'green' photons is only about 75 % of that for 'red' photons. The shown fluorescence traces are not typical in terms of photostability; generally, premature photobleaching occured even at excitation powers as low as 3.3 µW. The photostability in measurements with 3.3 µW, 6.75 µW and 13.5 µW was at times difficult to quantify because photobleaching steps could barely be identified. All average photostability lifetimes τ_{ph} were below 1 s (see Figure B.20).

CoPS measurements with labelled DNA in the current conditions are not providing reliable number estimates mainly due to limited photostability of the blue/green fluorophores. The necessary analysis

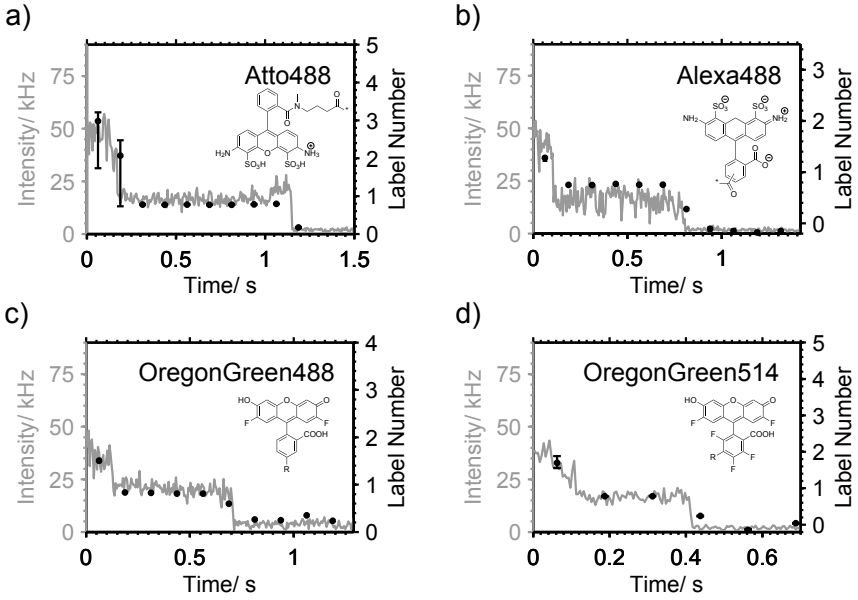

FIGURE 30: Single molecule CoPS analysis of DNA hybridization probes with dyes in the blue/green wavelength regime. a) Atto488, b) Alexa488, c) OregonGreen488 and d) OregonGreen514 at 6.75 µW laser excitation power at 470 nm and a repetition rate of 20 MHz. Time resolution (= analysis period τ_{acq}) of 2.5 MLC or 125 ms. CoPS estimates correlate with intensity bleaching steps. Black: Label number estimates with error bars derived from resampling algorithm, grey: Intensity.

period for CoPS is on the order of or even higher than the observed photostability times. To this end, I screened eight more ROXS buffers based on PCD oxygen scavenging together with practical student Martine Haan. Unfortunately, no significant enhancement of photostability could be observed and the additionally tested bodipy and Dy485XL dyes proved even less photostable [165].

6.4 RECOMMENDED ORGANIC DYES FOR COPS ANALYSIS

In a nutshell, all six tested dyes in the red wavelength regime, several of the selected dyes in the green/yellow regime and none of the dyes in the blue/green regime were deemed suitable for CoPS under the experimental conditions.

This conclusion was made from a careful analysis of the brightness, .i.e., the estimated detection probalility, and the respectively obtained label number estimates as well as the susceptibility of the fluorophores-DNA constructs to photodestruction.

According to the criteria laid out in Chapter 5, a certain brightness of the dye allows for a certain minimum analysis period to be applied for sensible estimation of the label number of an ensemble of probe molecules. To reduce the variance in label number estimates, both of an ensemble of probe molecules and of time-dependent CoPS estimates of single probe traces, the analysis period can be prolongued. A dye is considered suitable for CoPS if the obtained brightness allows for a minimum analysis period that is much lower than the average photostability time of the fluorophores. If this is the case, photobleaching is negligable; otherwise, CoPS experiments can still be performed, but a loss of labels due to photobleaching has to be taken into account.

In general, dyes in the red wavelength regime have very high extinction coefficients and medium quantum yields, in the green/yellow regime medium to high extinction coefficients and medium to high quantum yields and in the blue regime extinction coefficients are reduced and quantum yields increased (compare Table 4, Table 5 and Table 6). In addition, the sensitivity of detectors varies with the wavelength; the APDs that were used in these experiments have a peak quantum yield around 700 nm [163] which decreases with the wavelengths. Also, photostability is thought to decrease with the excitation wavelength [157, 166].

The dye with the highest measured brightness and corresponding photostability was Atto647N, the fluorophore that was mainly used for CoPS so far. If the application does not require a different fluorophore, it is still the best choice for CoPS. For the green/yellow dyes, brightness values similar to those of the dimmer red fluorophores were reached, albeit at lower photostability (compare e.g. SiR and Cy3B). In this wavelength regime I could not gain absolute control over dye photophysics in all cases. A prerequisite for CoPS is that all dyes on a probe can be treated with the same detection probability. As long as this condition is fullfilled, fast blinking on a timescale much slower than the analysis period should not influence CoPS estimates and long off-times in the seconds range lead to an apparent reduction in label number. Out of the investigated dyes for a second wavelength channel, Cy3B seems most suitable for its ´clean‘ photophysics and relatively high photostability. Unfortunately, no dye in the blue/green wavelength regime could be identified for CoPS. All dyes were dimmer than the previously investigated ones and much more prone to photodestruction.

A prospective improvement for organic dyes in the lower wavelength regimes lies, e.g., in the use of a 561 nm or a tunable pulsed laser to better match the excitation maxima. The extinction coefficient

ϵ_λ at the maximum is, e.g., about three and 2.5 fold higher than ϵ_λ at the current excitation wavelength for Atto488 and Atto550, respectively. The least excitation power for sufficient molecular brightness is needed for excitation at the maximum, which generally results in least photobleaching and reduces background photons [167, 168]. The photostability might also increase at higher excitation wavelengths by reducing absorption to higher excited electronic states [167]. As well, the current APDs could be exchanged for detectors with higher photon detection efficiency in the lower wavelength regime, e.g., such as the τ-SPAD fast with about 1.75 fold higher detection efficiency at 500 nm (PicoQuant, Berlin, Germany). The combined effect of the above mentioned measures on dye photostability can only be revealed in experiments, but the estimated increase in detection probability ($\sim 3 \cdot 1.75 \approx 5$ fold for Atto488) puts CoPS in the blue/green wavelength regime into perspective.

Altogether, experiments in this chapter showed that CoPS is feasible with many dyes in the red and green/yellow wavelength regime. Conceptually, there is no limitation in spectral parameters for CoPS, but in practice, reduced photostability towards the blue end of the spectrum restricts the use of organic dyes. Having identified different suitable fluorophores, a whole toolbox can be supplied to expand the applicability of this counting method and provide possibilities for multiplexing.

7

LABEL NUMBER ESTIMATION WITH FLUORESCENT MARKERS

Quantifying the number of molecules in a complex, e.g., to infer the oligomeric state of active signaling units of cell membrane receptors, by fluorescence based techniques requires specific labeling of the proteins of interest. A multitude of different labeling schemes have been proposed, each approach with its advantages and downfalls (see discussion in Section 2.1.1). A precise knowledge of the overall labeling stoichiometry is essential for the determination of absolut protein numbers.

As a first demonstration of CoPS in a biological context, I set out to determine the label number distribution of organic dyes on different routinely used fluorescent markers *in vitro*. I investigated SNAP-tag, anti-GFP antibodies, anti-GFP nanobodies and streptavidin. This was the first step towards in depth biological studies. *The research presented in this section was published in Grußmayer et al. [49], hence I am following the narrative of the publication*.

I chose SNAP-tag, a small DNA repair enzyme that can be genetically fused with the target protein and covalently labeled with a fluorophore modified O^6-benzylguanine (BG) substrate [26–28], as a reference with a nominal label number of one. SNAP-tag labeling is efficient *in vitro* and *in vivo* and was previously used in single-molecule studies and for super-resolution microscopy [169–171]. Immunostaining with antibodies is a common procedure to image protein distributions in fixed cells [17]. Thus, I opted for a monoclonal anti-GFP antibody (anti-GFP Ab) as a second marker in addition to SNAP-tag. Antibodies have the disadvantage of larger size which may limit the achievable resolution. This ´linker-error‘ problem can be circumvented by the use of nanobodies, small single-domain antibodies, that are therefore important for super-resolution imaging [30, 172] Here, I again went for the anti-GFP variant of a camelid nanobody. As a last marker I chose streptavidin, a protein tetramer with four high affinity binding sites for the small vitamin biotin. This combination of binding partners is frequently used for surface immobilization *in vitro* and was also my method of choice to prepare single molecule surfaces for the DNA based probes of Section 5.2 and Section 6.1. Streptavidin-biotin binding was also applied, e.g., for staining of cell surface proteins in living cells [173].

Anti-GFP Ab, anti-GFP nanobody and streptavidin were covalently modified with fluorophores by a simple coupling of amine reactive NHS-esters. This is often referred to as unspecific labeling because the targeted lysine residues frequently occur in proteins thus labeling can occur at multiple random sites. The label number can be adjusted by the dye-to-protein ratio and reaction pH, but depends on the reactivity of the NHS-esters and the structure and properties of the fluorophore and protein. It may even be possible to selectively target the amino-terminus of a protein [39, 40, 43, 44]. Here, I used the standard CoPS fluorophore Atto647N and in addition Alexa647, for it is often applied in biological studies. Both dyes were deemed suitable for CoPS, albeit care has to be taken to minimize photobleaching of Alexa647 (see Section 6.1).

At first, I will present the label number distributions determined with CoPS and compare them with the commonly used degree of labeling, a measure of the relative concentrations of label and protein determined by ensemble absorption spectrometry. Then, I will focus on the spectroscopic changes of the dyes as they are coupled to the marker proteins and discuss the influence on CoPS measurements.

7.1 LABEL NUMBER DISTRIBUTION OF FLUORESCENT MARKERS

Immobilization of fluorescent markers could be conveniently achieved by binding to their protein target or, in the case of SNAP-tag, via a genetically fused His_6-tag and an anti-His_6 antibody (see Figure 31 a), b), e) and f)). For measurements, I used again ROXS Red for photostabilization. The field of view was scanned with laser excitation powers $\leq 3\,\mu W$ to avoid premature photobleaching of labels and photon statistics for CoPS were acquired at $5\,\mu W$. I used the same analysis period of 2.5 MLC or 125 ms for photon statistics accumulation as for the measurements with the respective dyes on DNA (compare Section 12.8). CoPS analysis revealed remarkable differences in the distribution of actively emitting labels among different samples.

Figure 31 c), d), g) and h) displays the label number distribution of the different fluorescently labeled markers. As expected, SNAP-tag has a narrow distribution with a predominant label number of one, regardless of the label (Figure 31 c)). The low probability to observe different label numbers may most likely be attributed to the error of CoPS estimation. SNAP-tag has a very weak tendency to form dimers (personal communication K. Johnsson) and it is also possible that two tags bound to one anti-His_6 antibody, but I deem this unlikely at the chosen protein concentrations.

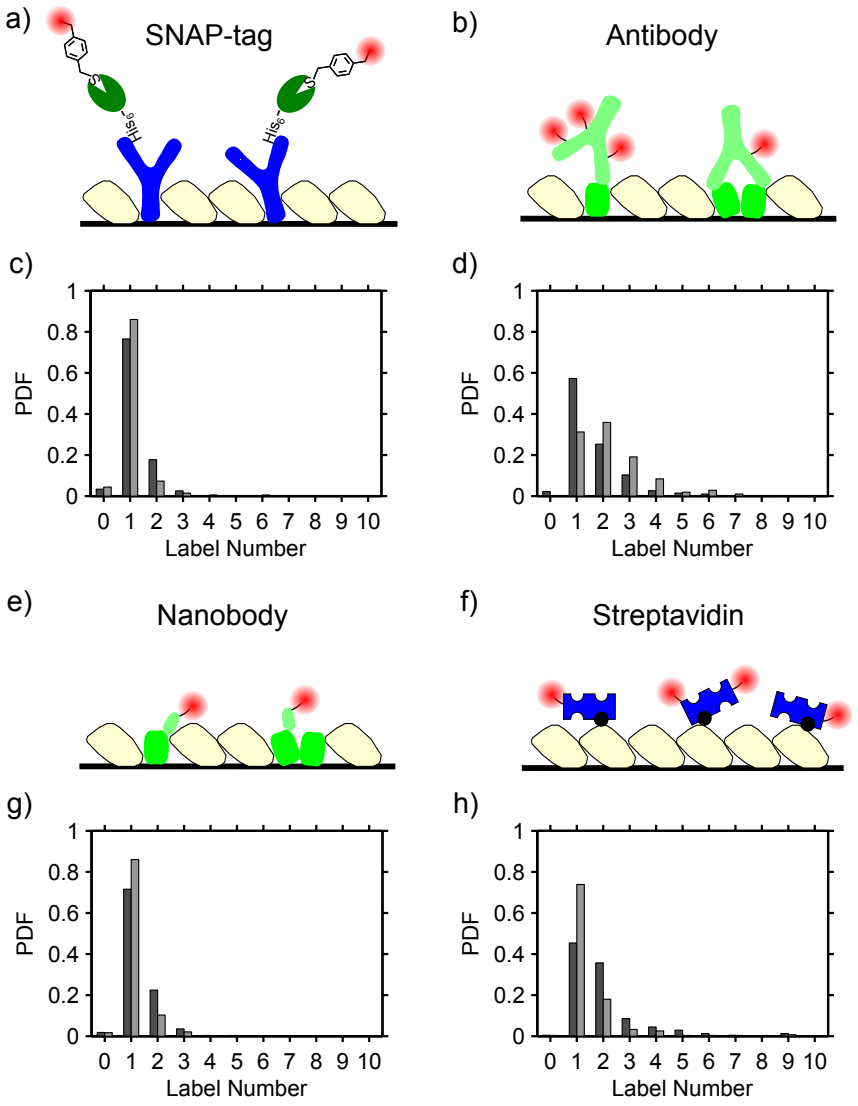

FIGURE 31: Label number distribution of fluorescent markers. Immobilization schemes and normalized label number distributiuons (PDF). Laser excitation power 5 µW at 640 nm with a repetition rate of 20 MHz, FOV-scan $\leq$3 µW. Analysis period 2.5 MLC or 125 ms. Dark grey: Alexa647 label, light grey: Atto647N label. a), c) BG-dye (red) labeled SNAP-tag (dark green) immobilized via His_6-tag and anti-His_6 antibody (blue) on a BSA (beige) coated surface. b), d) Labeled anti-GFP antibody (light green-red) immobilized bound to eGFP (green). e), g) Labeled anti-GFP nanobody (light green-red) bound to eGFP (green). f), h) Labeled streptavidin (blue–red) bound to biotinylated BSA (black–beige)).

In contrast, label number distributions of anti-GFP Ab are much broader and skewed to the right; label numbers up to around six are observed (Figure 31 d)). The labeling efficiency is influenced by the dye-to-protein ratio during the reaction. Anti-GFP Ab-Alexa647 shows lower label numbers than anti-GFP Ab-Atto647N, also because labeling occurred with a 3.3-fold lower dye-to-protein ratio (3:1 compared with 10:1). When the amount of dye is the same, label number ditributions are almost identical (see Figure C.24).

The label number distributions of nanobodies have a prevailing peak at one and resemble those of SNAP-tag rather than those of the antibodies (Figure 31 g)). This is remarkable especially for the Alexa647 label that was used in large excess over the nanobody (40:1). A possible explanation for the low label number lies in the small number of reactive amine groups per nanobody. The 13 kDa molecule has only three lysines and one amino-function at its N terminus. Either only one of those residues is fully available for labeling or a higher number of labels per protein interfere with its functionality, as already discussed for regular antibodies [45]. Because of the immobilization procedure, only labeled and functional markers are considered. Nieuwenhuizen et al. used the same nanobodies for quantitative localization microscopy, also labeled it with Alexa647 and their analysis confirmed the emitter number of one [174].

Streptavidin displays again a wider spread of label numbers (Figure 31 g)); the distribution for Alexa647 (6:1 dye-to-protein ratio) is somewhat in between that of the Ab label number distributions in Figure 31 d) and the distribution for Atto647N tends to lower label numbers. An interesting question for future studies is whether these differences between ATTO647N and Alexa647 are due to dye–dye interactions or due to different reactivities in the labeling reactions. With ´unspecific‘ labeling, dyes may come into close proximity and energy transfer processes such as singlet–singlet annihilation could result in a loss of active emitters.

Next, I compared the label numbers obtained by single molecule CoPS studies with the commonly used degree of labeling (DOL). The DOL computes the average number of dyes per protein by measuring their relative concentrations in an ensemble absorption measurement (seeSection 10.2). Since the exact molecular weight and sequence of the anti-GFP antibody was unknown, I referred to the average properties of IgG Ab (ϵ=210 000 $\mathrm{M}^{-1}\,\mathrm{cm}^{-1}$) as an approximation. The label number distributions from Figure 31 were characterized by the corresponding average label number (ALN) along with quantiles. A summary of the results is given in Table 1.

TABLE 1: Comparison of single-molecule CoPS measurements from Figure 31 with ensemble absorption measurements of label numbers per protein. Table 1 of [49]. Degree of labeling (DOL) measured by ensemble absorption spectroscopy with a relative error of 20 % (see Section 10.2). Average label number (ALN) with standard error of the mean (SEM) and standard deviation (σ) determined from CoPS analysis and median of the label number (MLN) distribution with 15.9 and 84.1 % quantiles.

	SNAP-tag	Anti-GFP antibody	Anti-GFP nanobody	Streptavidin
Alexa647				
DOL±ΔDOL	0.9±0.2	2.1±0.4	1.1±0.2	2.4±0.5
ALN±SEM(σ)	1.21±0.04 (0.55)	1.70±0.05 (1.00)	1.32±0.03 (0.61)	1.94±0.07 (1.32)
MLN($Q_{0.159}$, $Q_{0.841}$)	1.1 (0.8, 1.7)	1.4 (0.9, 2.5)	1.2 (0.8, 1.8)	1.5 (1.1, 2.6)
Atto647N				
DOL±ΔDOL	0.8±0.2	2.9±0.6	0.3±0.1	1.9±0.4
ALN±SEM(σ)	1.05±0.04 (0.55)	2.22±0.09 (1.26)	1.12±0.03 (0.42)	1.50±0.07 (1.22)
MLN($Q_{0.159}$, $Q_{0.841}$)	0.9 (0.8, 1.3)	1.9 (1.0, 3.4)	1.0 (0.8, 1.4)	1.1 (0.9, 1.8)

The DOL and the average/median label number (ALN/MLN) rely on complementary methods, that is, the former uses absorption measurements and the latter detects fluorescence (photon statistics) for analysis. The ensemble absorption measurement will always take into account unlabeled protein and remaining dye in solution that is not covalently bound. Fluorescence, on the other hand, only observes active emitters on labeled protein and, by proper dilution and immobilization, is able to assign label numbers even to single molecules. DOL, ALN, and MLN values do not indicate deviation from 1:1 stoichiometry for SNAP-tag samples. Indeed, efficient labeling is achieved with both BG-substrates. The narrow distribution of label numbers of anti-GFP nanobody-Alexa647 with little skew (Figure 31 g)) is confirmed by the DOL measurement. The DOL value of $\sim$0.3 for anti-GFP nanobody-Atto647N provided by the supplier is lower than the ALN/MLN of around one, which suggests a significant fraction of unlabeled protein in the mixture. The MLN is smaller than the ALN for the protein tags with broader label number distributions. This reflects the skew of the distributions with tails to higher label numbers. The antibody and streptavidin samples for both dyes have a DOL value that is larger than the ALN value.

When I had a closer look at the corresponding absorption spectra, I discovered that they differed from the spectra of the respective free dyes and labeled oligonucleotides. In addition, I registered diverse photophysics of single fluorophores on labeled markers during CoPS data acquisition, although the experimental conditions were the same as for single molecule measurements with DNA probes. These findings are addressed in detail in the next section (Section 7.2).

The DOL calculation is based upon the known properties of the free dye. It may only provide a rough estimate of the number of labels per protein if the extinction coefficient of the dye and protein change upon labeling. Despite these shortcomings, DOL measurements are widely applied because the method is simple and there is a lack of convenient alternatives [42, 44, 175, 176]. The DOL value most likely overestimates the number of fluorescing dyes per protein in this case due to the observed changes in the absorption of the conjugated dyes (Section 7.2). Concurrently, the number of absorbing dyes (regardless of their ability to fluoresce) are underestimated [175]. Also, the DOL measures the relative concentration of dye-to-protein regardless of the quality of the labeled protein. It was previously shown that the fraction of functional antibodies decreased as a result of increased labeling [45]. In our single molecule studies we used an inherent quality control by immobilizing the fluorescent markers via their target protein. It is advisable to investigate the number of labels per marker in an environment similar to that of the fluorescent reporter in action. Using the same quantification method to investigate the fluorescent marker and to determine the number distribution of the target has the additional advantage of shared estimation uncertainties.

7.2 INFLUENCE OF MARKER PROTEINS ON LABEL NUMBER ESTIMATIONS

It is well known that the photophysical properties of dyes are subject to changes in their environment. Sometimes this influence can be useful and fluorophore may be turned, e.g., into sensors. Here, a change of dye properties upon conjugation to marker proteins is generally unwanted, but cannot be completely prevented.

Indeed, the ensemble spectra of dye-conjugated markers differ from those of the respective free dyes. A general characteristic of the free dye absorption spectrum is a shoulder to the left of the absorption maximum. Upon labeling, a blue-shifted absorption peak appeared at $\sim$610 nm for the conjugates with Alexa647 and a more pronounced peak at $\sim$606 nm for Atto647N conjugates. The additional absorbing dye species is not fluorescent as revealed by fluorescence excitation spectra (see Figure C.25). The relative height of the blue-shifted peak for Atto647N conjugates rises from the streptavidin to the antibody sample, just like the discrepancy between DOL and ALN values. SNAP-tag conjugates do not display such secondary peaks. Blue-shifted absorption peaks have been reported previously for organic dyes and were attributed to dye aggregates that form with increasing labeling. The dyes are presumably

quenched due to stacking or H-aggregate formation [38, 40, 42, 175, 177]. These findings were supported by a measured decrease of the relative quantum yield of protein conjugates with respect to free dye already at low DOL [42].

I did not only observe a non-fluorescent fraction of labels, but noticed heterogeneous photophysics of the remaining active emitters. This was interesting because measurements with DNA probes did not reveal such behaviour although the same experimental conditions were used. Most importantly, there was no substantial difference in photostability for Alexa647 samples, while the photostability was reduced for Atto647N-conjugates (see Figure B.19 b)). The average photostability lifetimes were still significantly higher than the analysis period in all cases so that CoPS measurements were not impaired.

In general, Atto647N was influenced more by the protein environment than Alexa647 ($\geq$45 % blinking, see Table 2). Fast blinking ($\sim$millisecond timescale) and brightness fluctuations occured for both dyes in all samples (see Figure 32, Figure C.26 and Figure C.27). The largest fraction of blinking Alexa647 labels was by far observed for the specific coupling to SNAP-tag (49 %).

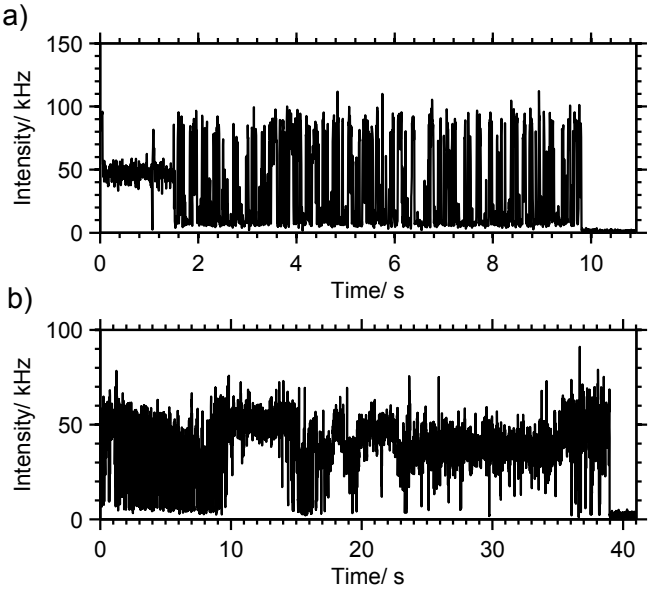

FIGURE 32: Differences in photophysical behaviour of protein-conjugated dyes. From Figure S6 and S7 of [49]. Excitation laser power 5 µW at 640 nm with a repetition rate of 20 MHz. a) Stable fluorescence emission followed by on/ off blinking for anti-GFP antibody-Alexa647. b) On/ off blinking and fluctuating fluorescence emission for anti-GFP antibody-Atto647N.

Possible explanations for this diverse behaviour are, e.g., transient dye-protein interactions that temporarily hinder the action of ROXS

TABLE 2: Classification of photophysical heterogeneity of protein conjugated dyes. Table S4 of [49]. Percentage of fluorescent transients that display rapid fluctuations in intensity along with the total number of investigated transients in brackets.

Blinking (total) / % (#)	SNAP-tag	Anti-GFP antibody	Anti-GFP nanobody	Streptavidin
Alexa647	49 (234)	7 (459)	19 (354)	28 (343)
Atto647N	62 (207)	60 (182)	71 (243)	1.1 (0.9, 1.8)

compounds or fluorescence quenching due to the specific amino acid microenvironment of the dye. Fortunately, heterogeneous photophysics did not have a significant effect on label number estimates. Distributions excluding fluorescence transients with blinking were almost identical to those using all probe molecules. (see Figure 33, Figure C.28 and Figure C.29).

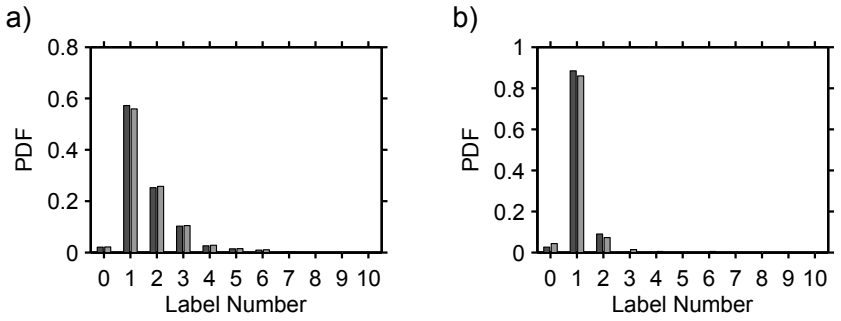

FIGURE 33: Fluorophore blinking does not significantly influence the label number distribution of fluorescent marker. Normalized label number distributions (PDF) for excitation laser powers of 5 µW at 640 nm with a repetition rate of 20 MHz. Analysis period 2.5 MLC or 125 ms. Dark grey: Non-blinking, light grey: All. a) anti-GFP antibody-Alexa647, b) SNAP-tag-Atto647N.

Determining the label number distribution of fluorescent markers and the same time observing the photophysical effects of dye-protein conjugation gave valuable insight for application of CoPS to biological systems. Indeed, the labeling method is of utmost importance, should be chosen with care and calls for thorough characterization under conditions identical or close to those of the main experiments. For absolut quantification of protein numbers it will be of advantage to use a marker with predominantly one label. This was the case e.g. for SNAP-tag with an efficient labeling protocol and for anti-GFP nanobodies-Alexa647 when they were labeled with a large excess of

dye. Still, antibodies are commonly used for staining of proteins in cells. One should keep in mind that the measured number distribution will then be a convolution of the protein number distribution with the label number distribution of the antibody. I found heterogeneous dye photophysics among all investigated samples, mainly stable fluorescence emission or blinking on a millisecond timescale. It turns out that CoPS estimation is not hampered by fluctuations in brightness that occur on a timescale much faster than the analysis period. The results of the previous sections show a promising perspective for CoPS to answer biological questions.

8

EXCITONS IN CONJUGATED POLYMERS

Single molecule fluorescence spectroscopy (SMFS) and fluorescence microscopy in general are widely applied for the investigation of biological systems. However, this is not the only realm where these methods help advance our understanding of soft condensed matter.

The first application of SMFS to organic semiconductors — so called conjugated polymers (CP) (see Section 2.1.2) — occured in 1997 by Vanden Bout and Barbara et al. and revealed highly dynamic photoluminescence (PL) blinking of single polymer chains [178]. The observations provided a first microscopic understanding of the limited quantum yield of these materials. Since then, fluorescence microscopy shed light on the photophysics of conjugated polymers that depends crucially on the chromophoric order (see Section 2.1.2).

Here, I used counting by photon statistics to study the photophysical properties of the model CP poly(3-hexylthiophene) in a Zeonex matrix together with Florian Steiner and Jan Vogelsang from the group of Prof. Lupton at Regensburg University. After establishing proper measurement conditions we quantified the number of independent emitters in dependence of P3HT chain length. In the next step, we investigated the dynamics of P3HT PL. Estimation of both the number and the brightness of emitters over time allowed to distinguish possible mechanisms of P3HT photoluminescence quenching. Our collaborators provided and prepared the investigated samples and shared their expertise in single molecule CP research and I performed all experiments and CoPS analysis in Heidelberg. *We are currently in the process of publishing our findings in Grußmayer et al. [179] and most of the results presented in the following are part of the publication.*

8.1 THE NUMBER OF INDEPENDENT EMITTERS IN POLY(3-HEXYLTHIOPHENE)

Measurements of P3HT photon statistics are challenging because the PL yield upon excitation with a blue laser is low. Conventional experiments with two detectors were not able to determine the degree of antibunching for single polymer chains and reported only ensemble averages [65]. CoPS measurements with organic dyes on DNA at similar blue 470 nm laser excitation were also not successful primarily

due to limited photostability at comparably low brightness that were additionally hampered by the bad detection efficiency of the APDs in that wavelength regime (see Section 6.3). However, the PL emission spectrum in Zeonex is very broad and reaches much farther into the red part of the visible spectrum (~500 nm to 800 nm) than for typical fluorophores [65].

P3HT was immobilized in a Zeonex matrix at single polymer chain molecule conditions (for details, refer to Section 12.7). I first evaluated PL saturation in scanned images upon increasing laser excitation power at 470 nm to find the best excitation conditions without promoting extensive photobleaching (see Figure D.30 and Section 10.1). We chose 2 µW laser excitation for the following measurement series of P3HT samples in Zeonex with different number averaged molecular weight M_n.

P3HT was fractionated by gel permeation chromatography against a polystyrene standard to yield six samples with low polydispersity index and M_n from 19 kDa to 110 kDa (see Section 12.7). I scanned surfaces of immobilized polymer, identified PL spots and subsequently measured the photon statistics of about 200 to 500 chains per M_n. To estimate the photostability of P3HT, I modeled the summed intensity of the different samples with a biexponential decay. All amplitude weighted average photostability times were between ~10 s to 35 s (see Table 15), at least two orders of magnitude larger than the photostability times of the organic dyes that were excited with the same laser (see Section 6.3). Thus, data analysis for CoPS seemed feasible.

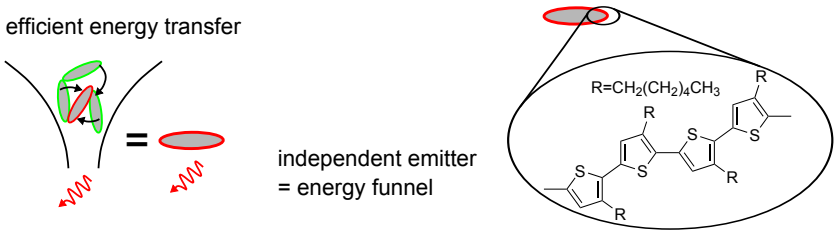

FIGURE 34: Independent emitters in conjugated polymers. Efficient energy funneling to energetically lower-lying chromophores due to singlet-singlet annihilation in a certain area of a conjugated polymer leads to photon emission of a single quantum system. Independent emitter symbolized by grey ellipsoid with red border. Modification of Scheme 1 of [179].

It is important to recall that photon statistics reflects the number of active, independent PL emitters. As mentioned before in Section 2.1.2, efficient energy transfer may take place among chromophores on the polymer chain that are in close proximity. We define one emitter as

an area of the polymer chain where efficient singlet-singlet annihilation leads to funneling of the energy to an energetically lower-lying chromophore that behaves as a single quantum system (compare Figure 34). The number of emitters then serves as an indicator of polymer chain conformation. CoPS estimates this number of independent emitters and their brightness with the assumption that all emitters contribute equally to the photon statistics. A variation in brightness of individual emitters of up to 20 % in simulations lead only to moderate deviations of the estimated emitter number [147].

I varied the analysis period for CoPS to ensure proper estimations because assessment of the expected PL brightness from PL traces was not as straightforward as for the organic dyes (data not shown). It turned out that the brightness of the samples was either around $p \sim 1 \times 10^{-3}$ or between $p \sim 2 \times 10^{-3}$ to 2.5×10^{-3} (see Figure D.32 b)). We assign the higher PL yield to samples where low amounts of oxygen were present to quench the triplet state as was observed in previous experiments in the Lupton group. As expected, photobleaching was more prominent in samples with higher PL yield. We chose an analysis period of 5 MLC or 250 ms which resulted in independent emitter number estimates of dim and bright samples of the same molecular weight that agreed well with each other (see Figure D.32 b) and compare Section 12.8).

Counting by photon statistics revealed the number of independent emitters in dependence of the chain length as shown in Figure 35 a). The initial increase in emitter numbers is approximately proportional to the chain length up to a molecular weight of $M_n \sim 60$ kDa. The slope of the fitted red line through the origin provides an estimate for the average size of an emitter of ~8.5 kDa. The number of emitters subsequently saturates for M_n 60 kDa at about 6 to 7 emitters (dashed line). The error bars reflect the lower and upper quartiles of the emitter number distribution. The shape of the distribution reflects the heterogeneity of one molecular weight sample (compare PDI in Table 7) convoluted with the distribution of CoPS estimates inherent to the fitting algorithm.

We attribute the saturation at higher molecular weights to increased self-folding of longer P3HT chains embedded in Zeonex as depicted in Figure 35 b). Better unfolding of long P3HT chains can be reached only in solution, i.e. in non-polar toluene, whereas strong folding occurs in poor polar solvents, such as poly(methylmethacrylate), and can even lead to energy transfer to a single energy funnel that displays perfect antibunching [53]. Unfolded chains or chains with the same degree of folding occur in the molecular weight regime with a linear increase in emitter number. This means that

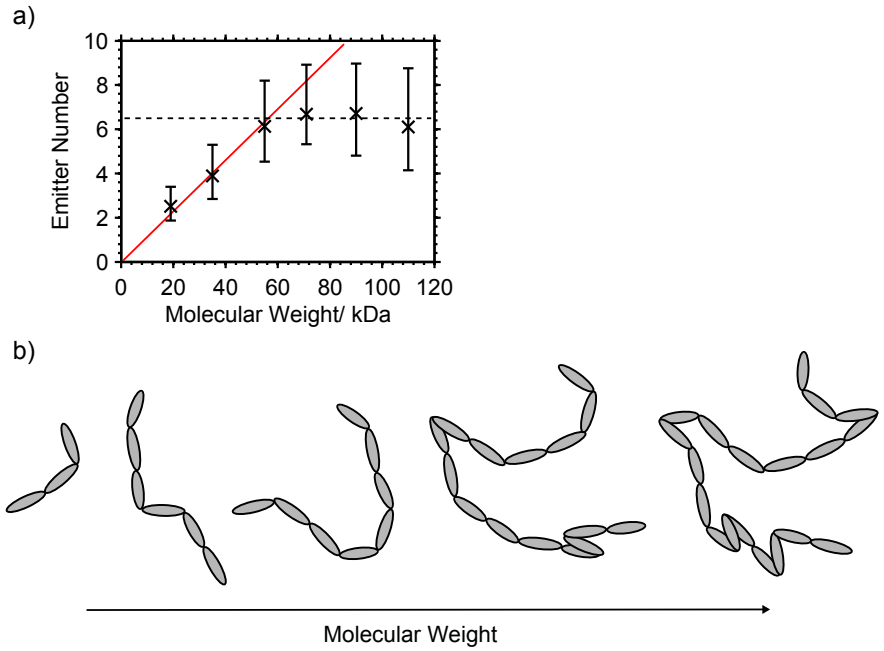

FIGURE 35: The number of independent emitters in dependence of the number average molecular weight of poly(3-hexylthiophene) (P3HT). a) Single P3HT chains embedded in Zeonex were excited at 470 nm with an excitation power of 2 µW and a repetition rate of 20 MHz. The median emitter number is displayed along with the lower and upper quartiles as error bars for CoPS estimates with an analysis period of 5 MLC or 250 ms. The slope of the fitted red line through the origin is 1 emitter / 8.5 kDa, and the dashed line is a constant of 6.5 emitters fit to the last four data points. Modification of Figure 1 of [179]. b) Possible conjugated polymer (CP) chain conformations with single chromophores as grey ellipsoids. Self-folding of the CP is increased as the chain exceeds a certain length.

the average size of ∼8.5 kDa (∼50 P3HT monomers) per emitter is either equivalent to the size of an absorbing chromophore or it is the smallest unit in which efficient singlet-singlet annihilation takes place in P3HT.

8.2 PHOTOLUMINESCENCE QUENCHING OF POLY(3-HEXYLTHIOPHENE)

So far it was possible to dynamically follow, e.g., PL intensity, anisotropy, or PL lifetime of single conjugated polymers. PL blinking has been observed already in the very first SMFS measurement of CPs and was explained by intramolecular energy transfer to a polymer defect, presumably a positive charge on the polymer chain [144, 178, 180, 181]. This quenching site acts as a trap for successively

excited excitons that are funneled towards the positive charge. The trap may affect different amounts of material depending on polymer morphology and even intermolecular quenching is possible[60, 65, 182, 183]. The quenching strength is thought to reflect the area that is influenced [184]. It is obvious that PL quenching impacts the performance of organic semiconductor devices and was thus subject of many studies [178].

At least two main types of trap states in CPs have been suggested: so called shallow trap states, [185–187] in which charge mobility is high and a large area is influenced, and so called deep trap states, in which the charge is confined and affects only little material [185–189]. Figure 36 a) illustrates the case of a shallow trap that affects all six independent emitters at the same time, assuming that screening of the whole polymer chain is faster than the average PL lifetime. This process leads to partial PL quenching that results in a reduced average brightness, but does not alter the number of independent emitters. In contrast, a deep trap (Figure 36 b)) completely quenches few emitters but does not affect the rest of the polymer chain. This corresponds to lower emitter numbers with unchanged molecular brightness.

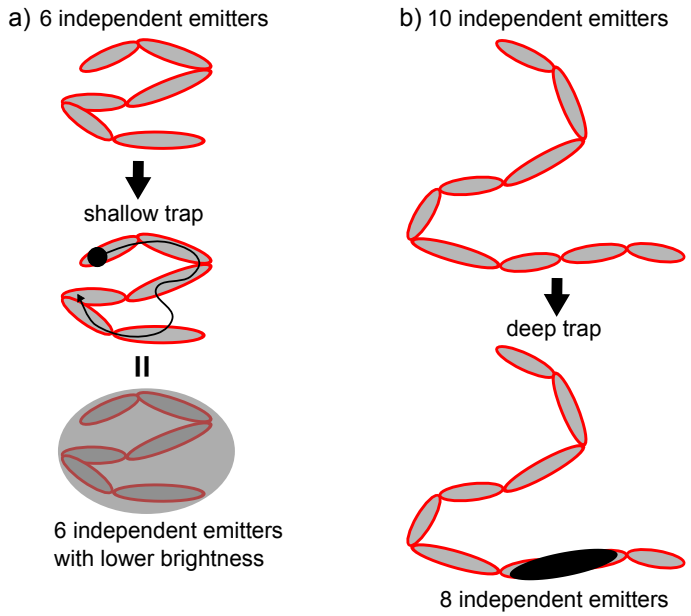

FIGURE 36: Different possible photoluminescence quenching mechanisms in conjugated polymers. Modification of Scheme 1 of [179]. a) Model of a shallow trap state with a highly mobile charge (black dot) that moderately quenches all (here: six) emitters (grey ellipsoids with red border). b) Deep trap state with a confined charge (black ellipsoid) that completely prevents PL of few (here: two) emitters (grey ellipsoids with red border).

The efficient measurement of photon statistics with the four detector CoPS setup enables following the dynamic changes of both the number of independent emitters and the photon detection probability of CPs for the first time. This information allows, in principle, to distinguish between the two proposed quenching mechanisms. To this end, we closely examined the PL traces of the P3HT sample with a number average molecular weight of 110 kDa. In Figure 37, example PL traces with corresponding CoPS estimates are shown. In the first case, strong correlation between the PL intensity and the estimated detection probability on the sub-second timescale (see Figure 37 a)) is confirmed by the normalized cross-correlation that peaks strongly with Corr(I, p)$\sim$0.8 at a lag time of zero. In contrast, the cross-correlation curve of the PL intensity and the emitter number is flat and the emitter number appears almost constant over time. The second example (see Figure 37 b)) displays almost opposing characteristics: The emitter number changes are correlated with the PL intensity at sub-second timescales with Corr(I, N)$\sim$0.75. In both cases the changes in PL intensity are reversible, i.e., blinking is observed, which rules out a simple explanation based on photodestruction of chromophores. Additional examples of both kinds are presented in Figure D.34 and in Figure D.35.

According to the proposed quenching mechanisms, the P3HT chain in Figure 37 a) comprises a shallow trap, whereas the P3HT chain in Figure 37 b) contains a deep trap. I measured 365 single P3HT chains ($M_n = 110$ kDa), which were sorted according to their blinking behavior. PL traces were manually classified with respect to intensity dynamics assisted by random inspection of traces by CoPS analysis. Approximately 12 % of chains contained shallow traps, 40 % of chains showed smooth intensity fluctuations consistent with small changes in emitter number and the remainder could not be sorted unambiguously into one of the two categories. To resolve these ambiguities, a full time-resolved CoPS estimation for all traces and a systematic study of possible classification criteria, e.g. the degree of cross-correlation of PL intensity with CoPS estimates, would be required. However, this was beyond the scope of this study.

We hypothesize that the different queching mechanisms are associated with different chain morphologies. It is conceivable that a shallow trap is more easily formed in an ordered region, whereas a deep trap can also be formed in a disordered, molten globule like morphology. A highly ordered morphology can facilitate the mobility of charges [66, 190], which would enable screening of an entire region of the polymer chain and is characteristic of a shallow trap.

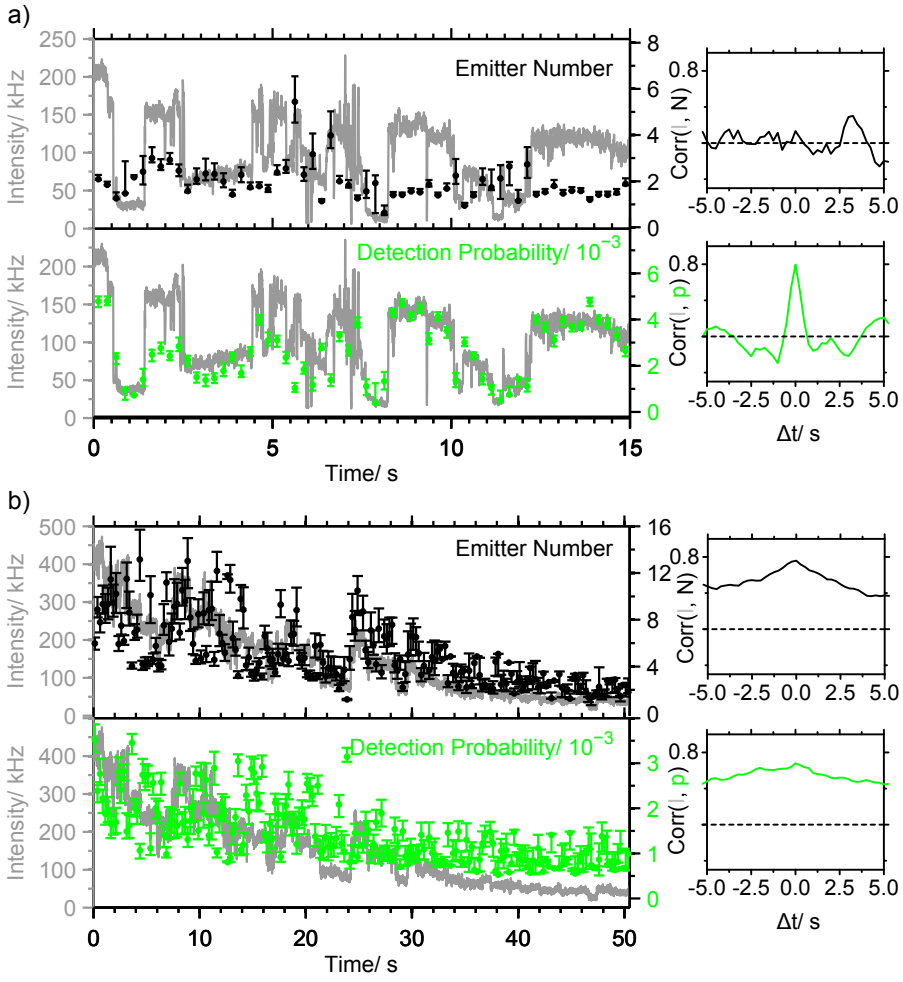

FIGURE 37: Different dynamical behaviour of photoluminescence in conjugated polymer chains due to quenching. Photoluminescence (PL) intensity traces (grey line) along with emitter number (black) and detection probability estimates (green) for single P3HT chains. Single P3HT chains embedded in Zeonex were excited at 470 nm with an excitation power of 2 µW and a repetition rate of 20 MHz. The analysis period was 5 MLC or 250 ms and the error bars were derived from resampling. On the right the correlation between PL intensity and emitter number (black line) or detection probability estimates (green line). Modification of Figure 2 of [179].

To conclude, we have performed a detailed investigation of the photon statistics of single CP chains. CoPs was for the first time applied in the field of soft condensed matter physics to study the device relevant polymer semiconductor material P3HT. This allowed us to determine 8.5 kDa (∼50 repeat units) as the average area of P3HT that contributes to a single emitter (energy funnel) by measuring the increase in emitter number with the molecular weight of polymer chains. CoPS proved even suitable to study the dynamic changes of emitter number and photon detection probability at the low photon flux of P3HT. These time resolved CoPS measurements enabled the investigation of PL blinking mechanisms. Two different types of quenching were proposed: positive charges that reside either in a shallow or in a deep trap state. Our quantification method in combination with measurements of ,e.g., PL spectra, PL lifetime and anisotropy offers a promising, new perspective to study photophysical processes of multi-chromophoric compounds.

Part III

SUMMARY, DISCUSSION AND OUTLOOK

9 SUMMARY, DISCUSSION AND OUTLOOK

Quantitative information, especially on the number of participants, is key to unravel molecular processes. Many diseases are associated with the formation of unwanted protein aggregates, while controlled oligomerization can provide advantages for biological structure and function [5, 191].

Counting by Photon Statistics (CoPS) is a single molecule fluorescence spectroscopy (SMFS) technique that provides quantification of fluorescent probes. CoPS exploits the photon antibunching effect, i.e. a dye as a quantum system may only emit one photon per excitation cycle. Modeling the number of registered multiple photon detection events (mDE) in a four-detector confocal microscope enables estimation of the number of independent emitters along with the photon detection probability p — a quantity proportional to the molecular brightness of a fluorophore. The method has a significantly extended counting range with respect to 'coincidence' analysis of photon pairs and does not require calibration (see Section 2.3).

The quality of CoPS estimates critically depends on the ability to accurately measure said photon statistics. Crucial parameters are the overall photon detection efficiency of the microscope setup, the brightness and photostability of the fluorophores in use and analysis parameters, most importantly the analysis period to collect multiple photon detection events.

I systematically addressed all these parameters to establish the best conditions for quantitative measurements and to explore the minimum requirements the method poses on fluorophores both in simulations and experiments. In the next step, I characterized many dyes according to the set criteria to provide a range of suitable fluorophores for CoPS.

This has transformed counting by photon statistics from a proof of concept quantification method using the model fluorophore Atto647N to a versatile counting technique with access to a whole toolbox of organic dyes. I successfully applied the counting technique to investigate two research questions in different fields of SMFS research, namely label number estimation with biological markers and photophysics of excitons in conjugated polymers.

9.1 A GUIDE TO CHOOSING FLUOROPHORES FOR COPS

Atto647N was so far chosen to demonstrate the feasibility of CoPS and to verify the extended counting range as compared to 'coincidence analysis' (see Section 2.3). It has excellent specroscopic characteristics and the photophysics can be well controlled, yet labeling of biological specimen has been found challenging due to the hydrophobicity of the dye [192]. Also, specific applications might, e.g., call for cell permeability, different fluorescence lifetimes or a different spectral channel. It follows that a significant extension of the range of suitable dyes is a crucial prerequisite to apply CoPS in different fields of research. In order to identify suitable fluorophores it is essential to establish a connection between the necessary photostability and molecular brightness for reliable CoPS analysis.

A systematic variation of brightness and analysis parameters in simulations revealed a prominent non-linear dependency of the minimal analysis period on fluorophore brightness for sensible estimation (see Section 5.1.1). The lowest simulated p calls for analysis periods in the seconds regime, whereas much shorter periods down to several tens of milliseconds are possible at high p (laser cycles are converted to seconds assuming a laser repetition rate of 20 MHz). In contrast to previous findings [148, 156], reliable CoPS estimates were possible for all tested detection probabilities, although the long minimum analysis time at the lowest brightness was not suitable for timely measurements. This discrepancy likely arose because previously, analysis periods were not extended far enough. Also, inaccuracies in the implementation of prior simulations were revealed. I showed that the analysis period can be up to ten times shorter than the previously established $\sim$2 MLC to 3 MLC or $\sim$100 ms to 150 ms [148, 156] which opens new possibilities for time resolved quantification. More importantly, the results proof that it is vital to adjust analysis parameters to the properties of the dyes.

Brightness and photostability are inevitably connected in experiments and can be tuned by the laser excitation power. A higher laser excitation power increases fluorophore brightness but leads to faster photobleaching. Experiments with a DNA based probe with four labels showed a non-linear dependence of minimal analysis period on laser excitation power. These findings were consistent with the results of simulations. The increased variance in photon statistics due to heterogeneity among dyes lead to slightly higher minimal analysis periods and somewhat worse absolute precision of CoPS label number estimates. The simulations and experiments also confirmed the

increase in emitter number precision with increasing analysis period and molecular brightness [147, 148, 156].

Photobleaching poses a natural upper limit to the analysis period t_{acq} and ultimately leads to a decrease in estimated numbers. Quantification is not impaired as long as the time to collect mDE statistics is much shorter than the average photostability time τ_{ph}. The necessary photostability for a certain brightness and tolerated photobleaching loss was estimated by modelling photodestruction of fluorophores as monoexponential decay and using the minimal analysis period as input parameter.

The molecular brightness and photostability are easily accessible properties of fluorophores. The established minimum analysis periods for a certain brightness now allow identification of suitable dyes based on sufficient resistance to photodestruction during said time. I characterized 16 organic dyes across visible spectrum, 10 of which turned out to be well suited for CoPS.

In general, the estimated molecular brightness was higher in the red wavelength regime than in the green/yellow wavelength regime, followed by the very dim blue/green fluorophores that are so far not eligible for CoPS. This trend is already reflected by the calculated brightness $B_\lambda = \epsilon_\lambda \cdot Q_f$ (compare Table 8, Table 10 and Table 12) and amplified by the wavelength dependent sensitivity of the detectors; the APDs have a peak quantum yield around 700 nm [163] which decreases with the wavelength. The photostability mainly decreased with the excitation wavelength. This could be explained by the increased energy of absorbed photons and by photobleaching via higher excited states that cannot be influenced by photostabilizing buffers [157, 166].

Altogether, I could establish a repertoir of suitable fluorophores for photon statistics analysis covering a wide spectral range from the green/yellow to the red to near infra-red wavelength regime. This opens up exciting possibilities for dual color investigations, e.g., to analyze relative stoichiometries in multi-component complexes or protein-protein interactions. Potential users can now choose from dyes that are frequently used in biological applications such as Cy3B, Cy5 or Alexa647 and I could even identify a cell permeable dye. If experimentally permitted, Atto647N is still the dye of choice due to its outstanding photostability at high brightness. The experiments confirmed that there is no conceptual limitation in spectral parameters for CoPS, but in practice, reduced photostability restricts applications at lower wavelengths.

A possible up to five fold increase in photon detection probability by improved excitation and detection conditions could make CoPS

feasible also in the blue/green wavelength regime, but the effect on dye photostability can only be revealed in experiments (Section 6.4). Recently, Grimm et al. discovered that modification of organic dyes with azetidine results in a substantial increases in brightness and photostability [193]. This could be combined with the attachement of triplet state quenchers to enhance photostability and has the potential to work in a cell [154, 194, 195].

We can now supply a toolbox of fluorophores for CoPS along with instructions for use. This turns counting by photon statistics into a readily available quantification method with possibilities for multiplexing and time resolved measurements.

9.2 APPLICATIONS OF COPS IN BIOLOGY AND MATERIALS SCIENCE

As a first application of CoPS in a biological context, I have determined the label number distributions of two organic dyes on four different markers (Chapter 7). These markers are commonly used to stain target proteins in cells; information about the overall labeling efficiency is essential to relate the quantified number of labels to the absolute number of target proteins.

SNAP-tag was covalently labeled with fluorophore modified O^6-benzylguanine substrates and CoPS experiments revealed a predominant label number of one, as expected. The other markers were randomly labeled by coupling of amine reactive NHS-esters to lysine residues or the amino-terminus. This resulted in broader and more skewed label number distributions that shifted to higher numbers when the dye to protein ratio was increased for both anti-GFP antibodies and streptavidin. A surprising finding was the prominent peak at one label per anti-GFP nanobody even when Alexa647-NHS-ester was added at 40 fold excess.

I also registered diverse blinking of single fluorophores and a slightly reduced photostability of one of the organic dyes. Fortunately, the change of fluorescence characteristics upon labeling did not have a significant effect on label number estimates. However, ensemble spectrometer measurements revealed a non-fluorescent fraction of dyes.

Analyzing the label number distribution of fluorescent markers and monitoring the photophysical effects of dye-protein conjugation at the same time provided valuable insight for the applications of CoPS, e.g., to quantify proteins in cells in the near future. Using a marker with predominantly one label, such as SNAP-tag or anti-GFP

nanobodies in this study, facilitates quantification of absolute protein numbers.

Several ongoing projects in the laboratory aim for quantification of proteins in cells using CoPS, including two-color applications to study interactions of a cell surface receptor and its intracellular kinase binding partner [196]. Initial measurements to study the number of vinculin molecules in focal adhesions, structures important for cell migration and morphogenesis [197, 198], revealed that fixation introduces high fluorescence background with two photon detection events already without staining of cells. First tests with living cells showed reduced background that can be modeled as a dim fluorophore, but complications arise by cell movement. Also, photostability of fluorophores in living cells cannot be improved by buffer systems. We are currently optimizing fixation and staining protocols with different cell lines to reduce background photons.

I could demonstrate the versatility of CoPS by venturing into the field of organic semiconductors. I studied the photophysics of poly(3-hexylthiophene) (P3HT), a device relevant conjugated polymers (CP) (see Section 2.1.2), in experiments that were performed in collaboration with the Lupton group at Regensburg University (see Chapter 8).

CP have a complex relation between chain structure, the number of absorbing chromophores and the number of active emitters [64, 65]. CoPS analysis revealed that the number of independent emitters of single P3HT chains embedded in Zeonex follows a saturation-like curve with increasing molecular weight. This behaviour can be explained by increased self-folding of the polymer chain. From the initial linear increase in emitter number we have estimated that energy funneling to a single emitter through singlet-singlet annihilation occurs from an area of the polymer corresponding to about 8.5 kDa ($\sim$50 repeat units).

The increased sensitivity and counting range of CoPS enabled these measurements despite the challenging low photoluminescence emission of P3HT. More importantly, CoPS delivers both time-dependent emitter number and molecular brightness estimates which allowed us to investigate PL dynamics in P3HT. Here, we could distinguish between blinking that corresponds to changes in photon detection probability and blinking that reflects mainly changes in emitter number. We hypothesize that this behaviour indicates two different, previously proposed quenching mechanisms.

As this study of conjugated polymers has demonstrated, CoPS is ideally suited to investigate multichromophoric systems and represents a highly valuable tool for material science in general. I also started using CoPS for the characterization of fluorescent core-shell

nanoparticles that were prepared by Eugene Mahon from UT Dublin. The aim of the project is to study how variations in nanoparticle preparation influence the number and properties of the enclosed fluorophores. The application of single molecule techniques to solve problems in materials science has so far been limited [51] and we added a new tool for future studies.

9.3 COMPARISON OF COPS WITH ALTERNATIVE FLUORESCENCE QUANTIFICATION APPROACHES

In addition to CoPS, there are several alternative approaches for fluorescence quantification that all have their strengths and limitations (see Section 2.2 and Section 2.3). Here, I would like to compare their features and focus on time resolution, fluorophores, accessible counting range and general applicability with emphasis on single molecule techniques.

The time resolution of CoPS depends strongly on the molecular brightness and is typically on the order of several tens to 250 ms for the experiments that I presented. The natural unit of the analysis time is the number of laser cycles to collect photon statistics and is converted to absolute time via division by the laser repetition rate. The absolute time resolution of CoPS can thus be increased by faster laser repetition rates. However, the dead time of APD and electronics ($\sim$100 ns) eventually leads to a loss of photons, i.e. a reduction of the detection probability. In addition, the time between laser pulses has to be sufficiently long to ensure relaxation of fluorophores to the ground state before the next laser cycle $\tau_f \ll \tau_{\text{laser repetition}}$ and higher laser repetition rates require higher average excitation power to maintain the same energy per pulse which can lead to higher population of triplet states and increase photobleaching.

In comparison, fluorescence intensity or FRET based quantification can be even faster than CoPS, because the two methods only measure mean photon emissions. Fluorescence detection is typically image based which allows parallel measurement of many molecules or complexes of interest; the time resolution is mainly determined by the frame rate of the camera in the range of a few milliseconds [199]. However, FRET is generally restricted to smaller complexes (N=4 or 5) due to the limited distance for energy transfer. Intensity measurements require a reference for calibration. The intensity of a single flurophore can also be obtained by analyzing the photobleaching step size of the investigated complex, but this prevents dynamic measurements as the sample is necessarily destroyed during the imaging pro-

cess. This is also the case for photobleaching step analysis and localization microscopy based counting (compare Section 2.2).

When it comes to suitable fluorophores, CoPS requires a certain fluoprophore brightness and photostability and I could identify many suitable organic dyes in this work (see Chapter 6). Fluorescent proteins (FPs), which are used by other quantification methods, are generally less bright and photostable. In addition, the mechanism of photodestruction of chromophores is poorly understood [200] and most available data on the photobleaching of FPs was not collected under CoPS conditions. This is why FP are no promising candidates for CoPS and have not been screened so far. In contrast, intensity quantification is less demanding and FRET based methods also work with all kinds of fluorophores, provided that suitable FRET pairs can be identified. Photobleaching step analysis and localization microscopy can also be performed with organic dyes or FPs. High S/N is crucial for quantification by photobleaching step analysis because otherwise bleaching events may become masked by noise. For this, extremely high NA objectives in combination with expensive cover slips are often used to achieve TIRF illumination of a thin layer above the coverslip and still, only a low number of photobleaching steps can be resolved [78, 79]. Localization microscopy only works with photoactivatable or photoswitchable proteins [201] and extensive characterization of photophysical parameters is required to obtain absolute protein numbers (compare Section 2.2).

The counting range of CoPS has been experimentally verified in the range of about 1–20 emitters and was subject of previous work. It is significantly higher than the typical counting range of up to four or five emitters for photobleaching step analysis and FRET based quantification. Intensity reference measurements can determine much higher average numbers, but lose the ability to quantify single probe molecules due to high variations in intensity [67, 74–76]. Localization microscopy based quantification is also not restricted to small numbers and was used to count to more than 100 [35] but requires significantly more effort to determine absolute numbers.

In this respect, CoPS is unique because it can provide time resolved estimations of fluorescence emitter number and brightness without calibration. Some of the popular ensemble quantification methods like fluorescence intensity distribution analysis [95], photon counting histogram [96] and the number and brightness method [97] can also provide emitter number and brightness, but they all require calibration. None of the other single molecule methods was applicable in the experiments with conjugated polymers because there was

no reference to calibrate intensity measurements or localization microscopy data. Photobleaching steps were mainly hidden due to complex photophysics and a high number of emitters. This emphasized the strength of photon statistics analysis: it is directly based on quantum mechanics, provides the number of active and independent emitters and their brightness and does not require calibration.

9.4 COUNTING BY PHOTON STATISTICS — READY TO USE

For a fluorescence quantification method to become popular, its implementation should be straightforward. Previous work focused on a robust implementation of the analysis and characterization of the extended counting range [156]. I could link fluorophore molecular brightness and the necessary photostability to provide a guideline for choosing fluorophores and can offer a range of suitable organic dyes. Moreover, analysis parameters can now be reliably adjusted either for maximum time-resolution or precision as the application demands (see Chapter 5).

The microscope setup needed for CoPS is a well aligned point scanning (confocal) microscope with appropriate filter sets and a detection pathway that is equally split towards four APDs with time correlated single photon counting (TCSPC) capability. Before I started my first experiments, I improved the detection efficiency of the setup in our laboratory more than three- to fourfold and later on facilitated multicolor measurements by remodelling the excitation pathway to couple all lasers into a single fibre (see Chapter 4). A high overall detection efficiency is key for all single molecule applications and can be reached by using the minimal necessary optical elements of high quality, including high NA objectives and a suitable choice of confocal pinhole, if necessary. The tremendous implications of a high photon detection efficiency for photon statistics analysis became clear in the following simulations and experiments (Chapter 5). The overall detection efficiency depends on the wavelength mainly due to quantum efficiency variation of the detectors. It is currently optimized for detection in the red to near-infrared wavelength regime for the CoPS microscope but alternative detectors optimized for shorter wavelengths exist.

Such confocal setups with multiple detectors and TCSPC electronics are typically accessible in advanced single molecule laboratories and are used, e.g., for polarization sensitive FRET measurements [202–205]. In the meantime, commercial solutions are also available. Often, regular confocal setups can be upgraded with APD detectors and TCSPC electronics. Several companies offer a 'fluorescence correlation spectroscopy add-on' or 'STED add-on' that includes

the necessary hardware and software for analysis. In principle, we can now provide a 'CoPS add-on' that renders a common confocal microscope ready for fluorescence quantification.

At the moment we are working on a variant of CoPS that measures photon statistics of diffusing molecules in solution with the confocal setup. Solution based CoPS should open the method to quantification of probes that cannot be immobilized and make it even more versatile. We are currently working on an extended CoPS model/algorithm that takes into account the spatial variation of the photon detection probability that results from probe diffusion. It will probably not allow quantification of single probe molecules because of short diffusion times through the confocal volume, but should consequently suffer much less from photobleaching. Solution based CoPS is similar, in this respect, to fluorescence intensity distribution analysis [95] or photon counting histograms [96], but should retain the advantage of being calibration free.

9.5 PERSPECTIVES FOR IMAGING BASED PHOTON STATISTICS MEASUREMENTS

For conventional CoPS, four-detector TCSPC data is successively acquired and processed from diffraction limited fluorescent probes. The acquisition of 2D photon statistics could enable much higher throughput by parallelized measurement of probes. In the simplest case of probe immobilization under single molecule conditions, one could proceed much like before by analyzing one data stream from the pixel location of each spot. Appreciation of the whole 2D information would require incorporating the shape of the point-spread function in the analysis. Extending the CoPS model function and including more sophisticated image analysis might enable emitter number and molecular brightness maps, e.g., for the interior of a cell. We also envision that the additional 2D mDE information can be used to enhance image resolution. A related approach has recently demonstrated improved resolution in simulations and for images of quantum dots using pixel photon number correlations with an emCCD camera [206, 207].

Straightforward 2D imaging can be performed with the current system by confocal scanning of the field of view, as previously demonstrated for 'coincidence' analysis [133]. However, data acquisition for a 256 px $\times$ 256 px image with a pixel dwell time of 50 ms (or 1 MLC at a laser repetition rate of 20 MHz) lasts more than 1 h, whereas the successive measurement of 200 isolated probes for the same analysis period takes only a few minutes. Camera based photon analysis

could solve this problem. The principle idea is to use four corresponding pixels or a photon number resolving camera to measure mDE events. Sample illumination by a high power pulsed laser could be achieved in TIRF or spinning disk configuration for optical sectioning and background suppression [208].

State of the art single photon sensitive electron multiplying CCD cameras at present offer only frame rates on the order of 1 kHz and scientific complementary metal oxide semiconductor (sCMOS) cameras still lack sensitivity [199]. Promising alternatives are so called APD arrays and CMOS single photon avalanche diode arrays (CMOS SPADs). They currently suffer from high dark count rates and low overall detection efficiencies due to low fill factors [199, 209, 210].

Detector development is rapidly advancing and recently widefield TCSPC imaging with MHz frame rate was achieved by combining an image intensifier with a conventional sCMOS camera to enhance the detection efficiency [211]. However, the data ouput is huge and would require processing of several tens of GB if 1 MLC are acquired for 256 px $\times$ 256 px CoPS imaging. Single photon detection is sparse imaging, most pixels will not register signals in one frame. I expect that data could be reduced by about one to two orders of magnitude — at least to that of a scanned TCSPC image — if only active pixels are read out. This requires additional per pixel logic for zero suppression, which at present severely limits single photon sensitivity [199]. This challenge could be met by a concerted effort of the detector development and single molecule communities.

Part IV

MATERIALS AND METHODS

10

EQUIPMENT

10.1 COUNTING BY PHOTON STATISTICS MICROSCOPE SETUP

The microscope used for CoPS measurements was a custom-built confocal microscope setup with an extended four-detector Hanbury-Brown and Twiss detection scheme. In brief, fluorescence was excited and collected with a high numerical aperture objective (alpha Plan-Fluar 100x/1.45 oil, immersion oil Immersol 518F n_e = 1.518 (23 °C), both Carl Zeiss, Jena, Germany) and isolated from excitation laser light by a dichroic mirror on a Zeiss Axiovert S100 TV microscope stand (Carl Zeiss, Jena, Germany) (see Figure 38). The fluorescence photons pass a telescope array that may hold a pinhole for confocal detection (two achromatic doublet lenses with a focal length of f = 50 mm) and a notch filter to further block the scattered excitation laser light. The detection path was then divided by three 50:50 beam-splitters to create four equal beam paths with the fluorescence photons focussed on avalanche photodiodes (APDs, SPCM AQR-14, Perkin-Elmer, Waltham, USA) (see Figure 38 c)). It was possible to insert filters to narrow the wavelength of the detected photons (e.g. bandpass filters and shortpass filters) both before the detection beam was split or directly in front of each APD. The detected photons were registered by a SPC 134 system that consists of four synchronized TCSPC-cards SPC 130 (Becker & Hickl, Berlin, Germany) which are controlled by a NI SCB-68 Connector Block (National Instruments, Austin, USA). Stage and photon-counting cards were run by custom LabView software (National Instruments, Austin, USA) for synchronized data acquisition. The microscope was equipped with a piezo-stage (piezoelectric scanner P561.3CL with E-503 LVPZT amplifier, E-509.C3A PZT servo-controller for capacitive sensors and E-516.i3 20-bit DAC Interface/Display, Physik Instrumente, Karlsruhe, Germany) for scanning and positioning objects in the confocal observation volume with nanometer precision.

All lasers were operated at 20 MHz repetition rate by the multichannel picoseconds pulsed diode laser driver PDL 808 Sepia or by the single channel PDL 800-B (PicoQuant, Berlin, Germany). Initially, an open beam path for the excitation pathway (see Figure 38 a)) was set up. A 635 nm pulsed picosecond laser diode with random polarization (fibre coupled LDH-P-635, PicoQuant, Berlin, Germany) passed

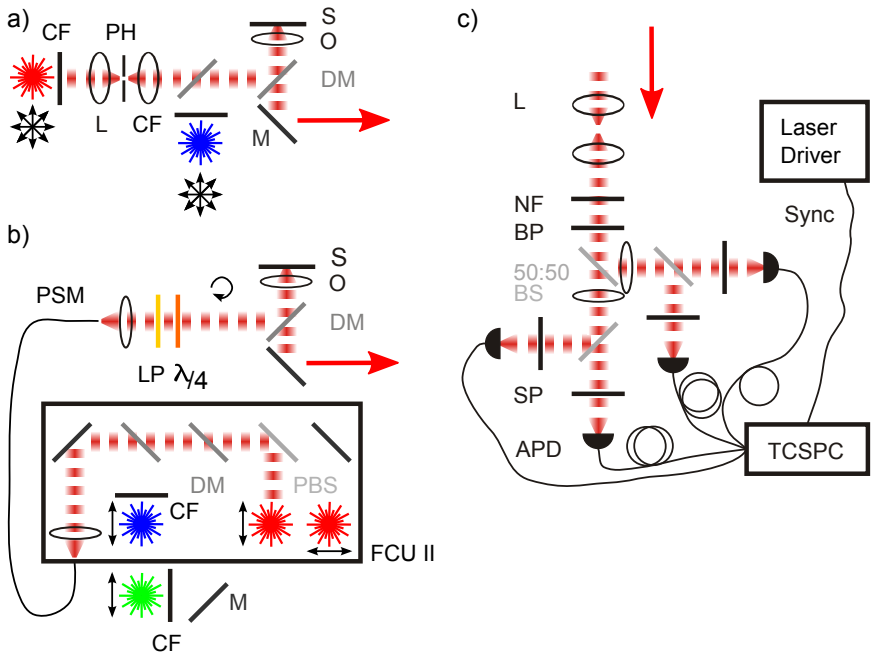

FIGURE 38: Scheme of the CoPS setup. a) Excitation with open beam path and unpolarized 635 nm and 470 nm lasers. The 635 nm laser profile is cleaned up by a telescope array and a pinhole. CF laser cleanup filter, PH pinhole, L lens, M mirror, DM dichroic mirror, O objective, S sample. b) Excitation with a fibre coupling unit. Two orthogonally polarized 640 nm lasers, a 532 nm and a 470 nm linear polarized laser are combined into one polarization maintaining single mode fibre (PSM). The laser beam is collimated, circularly polarized by a quarter waveplate and directed into the microscope. PBS polarizing beam-splitter, LP linear polarizer, FCU II fibre coupling unit. c) Detection pathway with an extended four-APD Hanbury-Brown and Twiss detection scheme. Fluorescence filters may be inserted at different positions. NF notch filter, BP bandpass filter, BS beam-splitter, SP shortpass filter.

a cleanup filter HQ 635/10 and a telescope lens array with a pinhole for laser beam shaping (two achromatic doublet lenses with a focal length of f = 16 mm and f = 60 mm, pinhole diameter 100 µm) before it was combined with a 470 nm pulsed picosecond laser diode with random polarization and cleanup filter z473/10 (fibre coupled LDH-P-C-470, PicoQuant, Berlin, Germany) via AT 505 DC Strahlenteiler. While the open beam path was used, the detection contained three 50:50 beam-splitters BS016 (Thorlabs, Munich, Germany).

The first experiments with the DNA hybridization samples with dyes in the red wavelength regime used this 635 nm open beam path excitation in combination with dichroic mirror Dual Line Strahlenteiler z488/633, dual notch filter 488/635 and bandpass filter ET Bandpass 685/70 (all AHF Analysentechnik, Tübingen, Germany). The experiments with the DNA hybridization samples with dyes in the blue/green wavelength regime used this 470 nm open beam path excitation in combination with dichroic mirror HC Laser-Strahlenteiler BS R488, single notch filter zet473NF and bandpass filter Laser-Sperrfilter HQ 530/60 (all AHF Analysentechnik, Tübingen, Germany).

Later on, the excitation pathway was modified to contain blue and red laser diodes in a fibre coupling unit (FCU II, PicoQuant, Berlin, Germany) and a green laser that is also directed into the box where all lasers are combined and coupled into a single polarization maintaining single mode fibre. Specifically, two orthogonally linear polarized 640 nm pulsed picosecond laser diodes (LDH-P-C 640B, PicoQuant, Berlin, Germany) were combined by a polarizing beam-splitter cube. Next, the 532 nm Pico TA picosecond pulsed amplified diode laser with second harmonic generation was cleaned up by filter z532/5 and added using dichroic mirror 560dxcr, followed by the linear polarized 470 nm pulsed picosecond laser diode cleaned up by filter z473/10 (LDH-P- 470 with fibre coupling removed) and added via AT 505 DC Strahlenteiler. The laser beam was collimated after exiting the polarization maintaining fibre (Kollimator MB 02, Linos now Qioptiq Photonics, Göttingen, Germany) and circularly polarized (achromatic quarter-wave plate, 450 nm to 800 nm, Thorlabs, Munich, Germany) before entering the microscope. While the fibre coupling unit was used, the detection contained three 50:50 beam-splitters G335-520-00 (Qioptiq Photonics, Göttingen, Germany).

For the experiments with the DNA tetra fluorophore samples and the DNA hybridization sample with SiR this 640 nm FCU II excitation was used in combination with dichroic mirror Dual Line Strahlenteiler zt532/640rpc, triple notch filter 488/532/631-640 and four bandpass filters ET Bandpass 685/70 (all AHF Analysentechnik,

Tübingen, Germany). For the experiments with the DNA hybridization sample with dyes in the green/yellow wavelength regime we used this 532 nm FCU II excitation in combination with dichroic mirror Strahlenteiler 530dcxr, triple notch filter 488/532/631-640, bandpass filter BrightLine 582/75 and four shortpass filters 694/SP HC Kurzpass-Filter BrightLine (all AHF Analysentechnik, Tübingen, Germany). For the experiments with proteins labeled with dyes in the red wavelength regime this 640 nm FCU II excitation was used in combination with dichroic mirror Triple Line Strahlenteiler z488/532/633, triple notch filter 488/532/631-640 and bandpass filter ET Bandpass 685/70 (all AHF Analysentechnik, Tübingen, Germany). For the experiments with conjugated polymers this 470 nm FCU II excitation was used in combination with dichroic mirror HC Laser-Strahlenteiler BS R488, single notch filter zet473NF and four shortpass filters 694/SP HC Kurzpass-Filter BrightLine (all AHF Analysentechnik, Tübingen, Germany).

10.2 ENSEMBLE SPECTROMETRY

All ensemble spectrometry was performed in Ultra-Micro Cells for fluorescence made of Quartz SUPRASIL with a light path of 3 mm (Hellma Analytics, Müllheim, Germany). Concentrations were kept low to prevent reabsorption effects and the absorbance was generally around 0.1. Ensemble UV-Vis absorption measurements with a Cary 500 Scan UV-Vis spectrometer were mainly used to calculate the degree of labeling (DOL) of the DNA and protein samples described in Section 11.2 and Section 12.5. Absorption measurements were baseline corrected against pure solvent. The DOL was computed as the relative concentration of fluorophores and DNA or protein in the solution using the known molar exctinction coefficients (ϵ) via Lambert-Beers' law (see Equation 1 and Equation 21) and can be found in Table 9, Table 11, Table 13 and Table 1. To calculate the concentration of DNA or protein, the absorption (A) of the organic dye at 260 nm or 280 nm needs to be substracted. It is typically computed via the known proportion of the maximum absorption of the dye, i.e. the correction factor (CF).

$$\begin{aligned} \mathrm{DOL} &= \frac{A_{max}/\epsilon_{max}}{A_{DNA/protein}/\epsilon_{DNA/protein}} \\ &= \frac{A_{max} \cdot \epsilon_{DNA/protein}}{\left(A_{260\,\mathrm{nm}/280\,\mathrm{nm}} - \mathrm{CF}_{260\,\mathrm{nm}/280\,\mathrm{nm}} \cdot A_{max}\right) \cdot \epsilon_{max}} \end{aligned} \tag{21}$$

Ensemble fluorescence excitation and emission spectra were obtained on a Cary Eclipse 500 fluorescence spectrometer (both spectrometers Varian, Darmstadt, Germany) with the excitation and emission slit set to 5 nm.

10.3 SOFTWARE

TABLE 3: Software Used in This Work

Name	Description/ Application	Provider
Matlab R2011a/ R2013a/ R2014a	data analysis, simulations and plotting	MathWorks (Ismaning, Germany)
Tex Live 2014	typesetting of dissertation	TeX Users Group
Inkscape	open-source vector graphics editor/ compilation of plots into figures and creation of vector graphic schemes	Inkscape Community

11

REAGENTS

All reagents were purchased from Sigma-Aldrich (Taufkirchen, Germany) unless stated otherwise and were generally of the highest available purity for molecular biology application. Pure water for buffer preparation was provided by a Milli-Q®Integral Water Purification System (Merck Millipore, Darmstadt).

11.1 FLUOROPHORES

All Atto dyes were purchased from Atto-Tec (Siegen, Germany) as active NHS-ester, Cy5-NHS-Ester from GE Healthcare (Freiburg, Germany), all AlexaFluor dyes (here: Alexa dyes) were purchased from Invitrogen Life Technologies (Darmstadt, Germany) as active NHS-esters. AbberiorStar635-NHS-Ester was bought from Abberior (Göttingen, Germany), Cy3B-NHS-Ester from GE Healthcare (Freiburg, Germany) and Silicon Rhodamine (SiR) from Spirochrome (Stein am Rhein, Switzerland). All dyes were solved at $2\,\mathrm{mg\,ml^{-1}}$ in anhydrous dimethylformamide (DMF) or dimethyl sulfoxide and stored at $-20\,^{\circ}\mathrm{C}$.

TABLE 4: Properties of Fluorophores in the Red Wavelength Regime.
[1]In aqueous solution from [158]

	MW / $\mathrm{g\,mol^{-1}}$	λ_{abs} / λ_{em} / nm / nm	ϵ_{max} / $\mathrm{M^{-1}\,cm^{-1}}$	Q_f	τ_f / ns	CF_{260}	CF_{280}
Atto647N	843	644/669	1.5	0.65	3.5	0.06	0.05
Atto633	749	629/657	1.3	0.64	3.3	0.05	0.06
Cy5	791.99	649/670	2.5	>0.28	1	0.05	
Alexa647	1300	650/665	2.39	0.33	1	0	0.03
Abberior Star635	992	634/654	0.6, 0.63	0.51	2.8	0.26	0.42
SiR	569.7	652/674	1.0[1]	0.39		0.15	0.1

11.2 DNA OLIGONUCLEOTIDES

Oligonucleotides for the DNA hybridization probe were custom synthesized and high performance liquid chromatography (HPLC) purified by Sigma-Aldrich (Taufkirchen, Germany). The probe

TABLE 5: Properties of Fluorophores in the Green/ Yellow Wavelength Regime

	MW / $g\,mol^{-1}$	λ_{abs} / λ_{em} / nm / nm	ϵ_{max} / $M^{-1}\,cm^{-1}$	Q_f	τ_f / ns	CF_{260}	CF_{280}
Cy3B	771	559/570	1.3	>0.67	2.8	0.09	0.08
Atto550	791	554/576	1.2	0.8	3.6	0.24	0.12
Atto565	708	563/592	1.2	0.9	4	0.34	0.16
AttoRho6G	711	535/560	1.15	0.9	4.1	0.22	0.19
Alexa532	721	532/554	0.81	0.61	2.5	0.24	0.09
Atto532	1081	532/553	1.15	0.9	3.8	0.22	0.11

TABLE 6: Properties of Fluorophores in the Blue/ Green Wavelength Regime. [1]Information courtesy of biomers.net

	MW / $g\,mol^{-1}$	λ_{abs} / λ_{em} / nm / nm	ϵ_{max} / $M^{-1}\,cm^{-1}$	Q_f	τ_f / ns	CF_{260}	CF_{280}
Atto488	981	501/523	0.9	0.8	4.1	0.25	0.10
Alexa488	643	495/519	0.71	0.92	4.1	0.3	0.11
OregonGreen 488 (6-Isomer)[1]	509.38	495/516	0.82	0.92	4.1		0.12
OregonGreen 514[1]	609.43	506/526	0.85		4.2		0.19

consists of a 94 bases long, biotinylated DNA strand with four 23 bases repeats (REP4) and the complementary small 23 bases oligonucleotide (REP') so that up to four REP' molecules can bind to one REP4 molecule. This probe was used in the very first CoPS experiment [146]. Sequences are given 5'-3'. REP4: C6 Amine-AAC GAG GAG GAC CCC TAT CCC AAA ACG AGG AGG ACC CCT ATC CCA AAA CGA GGA GGA CCC CTA TCC CAA AAC GAG GAG GAC CCC TAT CCC AA-Biotin. REP': C6 Amine-TTG GGA TAG GGG TCC TCC TCG TT. REP4 and REP were labeled with different dyes in the red and green/yellow wavelength regime according to the protocol provided in Section 12.4. REP' labeled with Atto488, OregonGreen488 and OregonGreen514 was custom synthesized, labelled and high performance liquid chromatography (HPLC) purified by biomers.net (Ulm, Germany).

The tetra probes consist of the 94 bases long, biotinylated REP4 strand described above and the complementary strand (REP4'). I designed the tetraProbe and it was first used by Anton Kurz [148]. REP4' contains four 2'-O-Propargyl uridine (pU) bases that are coupled to the respective azide modified dye by biomers.net (Ulm, Germany). The sequence is given 5'-3'. REP4': (pU)TG GGA TAG GGG TCC TCC

TCG TT(pU) TGG GAT AGG GGT CCT CCT CGT T(pU)T GGG ATA GGG GTC CTC CTC GTT UTG GGA TAG GGG TCC TCC TCG TT.

DNA probes were formed by adding the respective two complementary DNA strands in either a 1:20 ratio (0.1 µM DNA hybridization probes, REP4:REP') or a 1:1 ratio (1 µM tetra probe, REP4:REP4') in 1x phosphate buffer solution (PBS) followed by hybridization through heating to 90 °C for 4 min and subsequent cooling to 25 °C (1 °C in 30 s) in a thermocycler (PTC-100, MJ Research, Waltham, USA).

12

METHODS

12.1 PREPARATION OF SNAP-TAG AND EGFP

His-tagged SNAP-protein preparation was performed as described in [212]. His-tagged eGFP was produced and purified as follows. In short, an updated version of a pETM vector containing an N-terminal His6-eGFP fusion [213] was transformed in E.Coli strain BL21-Gold(DE3). Cells were cultivated in LB medium containing $50\,\mu g\,ml^{-1}$ kanamycine at 30 °C to OD600 = 0.4 and expression was induced by 1 mM IPTG for 4 h at 30 °C. Proteins were isolated using Protino ®Ni-IDA-Kit 2000 packed columns (MACHEREY-NAGEL, Düren, Germany) according to the procedure described by the manufacturer and dialyzed against PBS with Slide-A-Lyzer Dialysis Cassettes 3.5K MWCO (Thermo Fisher Scientific, Bonn, Germany). For storage at −80 °C, 10 % glycerol was added and samples were frozen until use.

12.2 PREPARATION OF BENZYLGUANINE SUBSTRATES FOR SNAP-TAG

Coupling of amine modified benzylguanine (BG-NH2, New England Biolabs, Frankfurt, Germany) with the NHS ester of the respective dye was performed in DMF in the presence of N,N-diisopropylethylamine (DIPEA) as catalyst. The concentration of BG-NH2 was 500 µM with a 1.2 fold excess of activated dye and the reaction took place at 30 °C for 3 h in the dark with continuous shaking. Reversed-phase (HyperClone 5µ ODS(C18) 120 Å column, Phenomenex, Aschaffenburg, Germany) HPLC (Agilent, Waldbronn, Germany) with 0.1 M triethylammonium acetate buffer with a 30 min gradient from 0 % to 75 % acetonitrile in water was performed to purify the BG-dye conjugate from free dye. BG-dye conjugates were confirmed by ESI-TOF mass-spectrometry (Bruker ApexQe hybrid 9.4 T FT-ICR, Bruker, Billerica, MA, USA).

12.3 REDUCING AND OXIDIZING BUFFER SYSTEM FOR PHOTOSTABILIZATION

All experiments with labeled DNA probes and proteins were performed with an enzymatic oxygen scavenging system and reducing and oxidizing agents (ROXS) to stabilize dye fluorescence [21]. For dyes in the red wavelength regime a buffer termed ROXS Red was used and prepared as follows. The oxygen concentration of a 5x PBS buffer containing 300 mM glucose and 12.5 % (v/v) glycerol was initially depleted by vigorously introducing argon into the solution for at least 20 min with a syringe needle. Shortly before measurements 1 mM tris(2-carboxyethyl)phosphine (TCEP), 2 U μM^{-1} glucose oxidase and 250 U μM^{-1} catalase (GOC), the most commonly used oxygen scavenging system in single molecule experiments, and 1 mM methylviologen (MV) and 1 mM ascorbic acid (AA) as ROX agents were added. For dyes in the blue/green and green/yellow wavelength regime a buffer termed ROXS Blue was used and prepared as follows. The oxygen concentration of a 5x PBS buffer containing 12.5 % (v/v) glycerol was initially depleted by vigorously introducing argon into the solution for at least 20 min with a syringe needle. A different oxygen scavenging system was used to avoid fluorescence background caused by excitation of cofactors in GOC. Shortly before measurements, 2.5 mM protocatechuic acid and 50 nM protocatechuate-3,4-dioxygenase as oxygen scavenger and either 1 mM MV and 1 mM AA or 1 mM MV and 1 mM propyl gallate as ROX agents were added.

12.4 PREPARATION OF DNA HYBRIDIZATION PROBES

The two strands $REP4$ and REP' described in Section 11.2 were labeled with NHS esters of different dyes according to manufacturer's protocol provided by ATTO-Tec (Siegen, Germany). Reversed-phase HPLC (HyperClone 5µ ODS(C18) 120 Å column or Clarity 3µ Oligo-RP column, Phenomenex, Aschaffenburg, Germany and HPLC Series 1100, Agilent, Waldbronn, Germany) with 0.1 M triethylammonium acetate buffer with a 30 min gradient from 0 % to 75 % acetonitrile in water was used to purify labeled $REP4$ and REP'. The degree of labeling (see Section 10.2) for each oligonucleotide was determined by absorption spectroscopy (Cary 500 Scan, Varian, Darmstadt, Germany) and can be found in Table 9, Table 11, and Table 13.

12.5 PREPARATION OF LABELED PROTEIN

Coupling of proteins with NHS-ester of the respective dye took place in PBS buffer with the pH adjusted to pH 8.3 using 1 M sodium bicarbonate solution. The activated dye was added in excess to the protein solution followed by incubation at RT for 30 min to 1 h in the dark. Reaction of SNAP-tag with BG-dye substrates was performed in SNAP dialysis buffer (100 mM NaCl, 1 mM dithiothreitol, 20 % glycerol, 40 mM HEPES pH 7.9) for 40 min at 37 °C in the dark. Labeled protein was separated from excess unreacted dye by gel filtration chromatography with illustra NAP-5 Columns (GE Healthcare, Freiburg, Germany) according to manufacturer instructions. In case of His-tagged protein, Protino ®Ni-IDA-Kit 150 packed columns (MACHEREY-NAGEL, Düren, Germany) were used and afterwards buffer was exchanged by dialysis against PBS with Slide-A-Lyzer dialysis cassettes (Thermo Fisher Scientific, Bonn, Germany) of adequate molecular weight cutoff. The DOL for each labeled protein was determined by absorption spectroscopy (Cary 500 Scan, Varian, Darmstadt, Germany). 0.1 % BSA was added to labeled nanobody and antibodies as a stabilizer for short term storage of samples at 4 °C until use.

Concentrations and protein: the ratio of dye to NHS-ester for the different samples were the following. 10 µM SNAP-tag, ratio 1:3 with respective BG-dye conjugate; 1 mg ml^{-1} anti-GFP nanobody (GFP-Trap, ChromoTek, Planegg-Martinsried, Germany), ratio 1:40 Alexa647-NHS-Ester; 1 mg ml^{-1} streptavidin, ratio 1:6 Alexa647-NHS-Ester; 1 mg ml^{-1} anti-GFP antibody (monoclonal antibody to GFP, Acris Antibodies, Herford, Germany), ratio 1:3 with respective dye-NHS-Ester and additionally 1:10 with Atto647N-NHS-Ester.

12.6 IMMOBILIZATION OF DNA PROBES AND PROTEINS

Lab-Tek chambered coverslides were used for all experiments. The chambers were cleaned with hydrofluoric acid (0.1 M) for 5 min, followed by 3 washes with 1x PBS and the procedure repeated once. Then, a mix of different proteins was deposited on the glass for specific immobilization of the respective probes. 0.1 nM to 1 nM solutions of probe molecules were incubated in the chamber until a spot density of ∼30 per 20 µm x 20 µm field of view was reached. All experiments were performed with an enzymatic oxygen scavenging system and reducing and oxidizing agents (ROXS) for photostanilization of fluorophores as described in Section 12.3. The Lab-Tek chambers

were sealed with Parafilm M®(Brand, Wertheim, Germany) to prevent reentering of oxygen from ambient air.

For immobilization of biotinylated DNA hybridization probes and tetra probes, BSA and BSA-Biotin (20:1 ratio, 5 mg ml^{-1}) was incubated for 30 min at RT or over night at 4 °C. After 3 washes with 1x PBS, 10 µg ml^{-1} to 100 µg ml^{-1} streptavidin was incubated for 20 min followed by another set of 3 washes. Labeled streptavidin was directly immobilized on BSA and BSA-Biotin (20:1 ratio, 5 mg ml^{-1}) surfaces prepared as just described. Labeled SNAP-tag was specifically immobilized on a layer deposited from 5 mg ml^{-1} BSA with 2 µg ml^{-1} anti-His antibody (anti His6, Roche Diagnostics, Mannheim, Germany) by incubation for 30 min at RT or over night at 4 °C and susequent 3 washes with 1x PBS. Labeled anti-GFP nanobody (GFP-Trap, ChromoTek, Planegg-Martinsried, Germany) or anti-GFP antibody (monoclonal antibody to GFP, Acris Antibodies, Herford, Germany) was captured by binding to eGFP. EGFP-BSA surfaces were prepared by incubation of 5 mg ml^{-1} BSA with 0.5 nM eGFP for 30 min at RT or over night at 4 °C followed by 3 washes with 1x PBS.

12.7 PREPARATION AND IMMOBILIZATION OF POLY(3-HEXYLTHIOPHENE)

Preparation and single molecule immobilization of Poly(3-hexylthiophene) (P3HT) was performed by Florian Steiner from the group of Prof. Lupton at Regensburg University much as described in [53, 65]. P3HT with a regioregularity of 95.7 %, weight average molecular weight M_w of 65.2 kDa and polydispersity index (PDI) of 2.2(EMD Chemicals Inc., Darmstadt, Germany) was fractionated and further purified by gel permeation chromatography (GPC) with a polystyrene standard to obtain 6 samples of different number averaged molecular weight M_n with a low PDI (see Table 7). The polydispersity index (see Equation 22) indicates the distribution of molecular mass in a given polymer sample; the number averaged molecular weight M_n (see Equation 24) is the arithmetic mean of the molecular weights of a polymer and larger polymers have a bigger contribution to the weight average molecular weight M_w (see Equation 23).

TABLE 7: Fractionation of Poly(3-hexylthiophene) by gel permeation chromatography

sample	1	2	3	4	5	6
M_n / kDa	19	35	55	71	90	110
PDI	1.56	1.20	1.11	1.09	1.09	1.09

$$PDI = \frac{M_w}{M_n} \tag{22}$$

$$M_w = \frac{\sum_i N_i M_i^2}{\sum_i N_i M_i} \tag{23}$$

$$M_n = \frac{\sum_i N_i M_i}{\sum_i N_i} \tag{24}$$

In brief, isolated chains of P3HT immobilized in a ∼200 nm thick Zeonex 480 (Zeon Europe, Düsseldorf, Germany) host-matrix were obtained by dynamically spin-coating at 2000 rpm from toluene. First, borosilicate glass cover slips (0.17 mm thickness) were cleaned in a 2 % Hellmanex III (Hellma Analytics, Müllheim, Germany) solution and rinsed with water. Then, glass cover slips were transferred into a UV-ozone cleaner (PSD Pro Series UV, Novascan, Ames, USA) to destroy residual fluorescent molecules. A 0.1 pM to 1 pM P3HT solution in toluene was mixed with a 6 % Zeonex/toluene solution for spin coating the coverslips. To prevent photo-oxidation, sample preparation occured in a glovebox filled with nitrogen and samples were sealed between two cover slips using Araldite®2011 two component epoxy paste adhesive (Huntsman Advanced Materials (Deutschland), Berkamen, Germany). The prepared samples were transported to Heidelberg in additional boxes that were flooded with nitrogen. Upon arrival, samples were stored in a glovebox until use.

12.8 COUNTING BY PHOTON STATISTICS — EXPERIMENTAL PROCEDURE AND ANALYSIS

In short, single molecule surfaces were scanned for CoPS experiments, probe molecule positions localized and subsequently photon statistics were acquired. Here, pulsed laser excitation is used in combination with a modified Hanbury-Brown and Twiss detection scheme with four detectors. Laser pulses were short and the spacing between

pulses was long compared to the fluorescence lifetime, such that each fluorophore in the focus emits at most one photon per laser cycle. A time correlated single-photon counting (TCSPC) unit records the photon arrival times for each avalanche photodiode (APD) and the number of multiple photon detection events (mDE) are calculated in data post-processing.

Specifically, mDE were calculated for a certain analysis period t_{acq} and non-linear regression of the model $P_m\left(N, p; i\right)$ to the mDE data with the Levenberg-Marquardt algorithm was performed. Background detection probabilities were typically estimated for each experiment and excitation laser power using the CoPS algorithm with $p_b = 0$ at the end of a trace when the fluorphores were photobleached. The resulting detection probabilities for estimated N=1 of 5–20 traces were averaged and used as input parameter p_b for the analysis. To achieve robust estimation of the number of emitters N and the detection probability p, the analysis period was divided into smaller analysis subperiods; randomly chosen 75 % of analysis subperiods provide subsamples for repeated CoPS parameter estimation. In addition, mDE of the analysis subperiods were weighted according to the intensity of the subperiod relative to the mean intensity of the analysis period such that the average number of emitters over the analysis period was estimated. The emitter number and detection probability for the analysis period are given as the median of the resulting parameter distributions and the quantiles $Q_{0.25}$ and $Q_{0.75}$ indicate the error of the estimated parameters for a single CoPS measurement.

For the first experiments conducted in the course of this thesis, namely the experiments with dyes in the red wavelegth regime in Section 6.1, dyes in the blue wavelength regime Section 6.3 and the label number distributions of fluorescent markers in Chapter 7, a constant analysis subperiod width of 0.2 MLC or 10 ms was used independent of the applied analysis period t_{acq}. Later, I discovered that it is better to use a constant number of analysis subperiods because otherwise subsampling does not properly reflect the distribution of estimated parameters when the analysis period is shortened. The effect on the estimated label numbers is insignificant for measurements with high brightness, nevertheless the error for individual measurements is underestimated (see Figure 39 and Figure A.18). The variance of the overall label number distribution of an ensemble of probe molecules is slightly underestimated and a higher fraction of CoPS fits do not converge for measurements with lower brightness for both shorter analysis periods and constant analysis subperiod, but the difference vanishes for appropriate (according to Section 5.2) analysis periods.

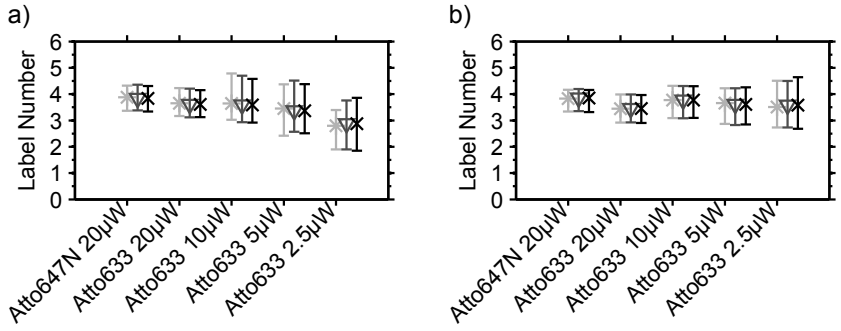

FIGURE 39: Comparison of CoPS analysis with constant analysis subperiod width and constant analysis subperiod number. Data from experiments with DNA tetraProbes with Atto647N and Atto633 described in Section 5.2. Excitation at 640 nm with a repetition rate of 20 MHz and laser power as indicated. Estimated label numbers (median with $Q_{0.25}$ and $Q_{0.75}$) for CoPS analysis with constant analysis subperiod of 0.2 MLC (light grey asterisks) and constant analysis subperiod number (50 for dark grey downward-pointing triangles and 100 for black crosses). a) Analysis period 5 MLC or 250 ms. b) Analysis period 0.5 MLC or 25 ms.

The CoPS model has to be provided with a background detection probability p_b, i.e. it is no fit parameter. For the simulated data the true, simulated background detection probability was used. For experimental data, p_b was typically determined by fitting the background photons at the end of a fluorescence trace after all fluorophores had already photobleached. The input p_b in the model was set to zero and the resulting detection probability for N=1 gave an estimate for the background detection probability. This process was repeated around ten times and the average p_b used as input for the CoPS model.

12.9 SIMULATIONS

A certain number of fluorescence traces of single probe molecules with a set number of independent emitters, i.e. dyes, were generated by Monte-Carlo simulation. A global random number generator (Mersenne Twister with a seed of zero) was used to successively simulate the individual traces. For each dye, photon detection in each simulated laser cycle was determined by comparing a certain detection probability p with a pseudorandom number drawn from a continuous uniform distribution between 0 and 1. In the following, photons were assigned to the four APDs in the extended Hanbury Brown and Twiss array according to pseudorandom integers drawn from the discrete uniform distribution on the interval [1, 4] (see Sec-

tion 2.3.2 and Figure 38). Fluorescence background was simulated as a single, dim fluorophore with detection probability p_b. After adding all detected photons per laser cycle and APD for the different dyes, only the macro time of one photon per laser cycle and APD was saved to mimick the dead time of the TCSPC electronics. A micro time reflecting the individual fluorescence lifetimes of the photons was not implemented as it is irrelevant for CoPS estimation. To better represent the experimental situation, photobleaching of the dyes was included in the simulation. For simplicity, only single exponential decay photobleaching characteristics was considered. Thus, for each dye, a pseudorandom number was drawn from the exponential distribution with mean photobleaching time constant τ_{ph} (in units of laser cycles) and photon detection from the dye was stopped when the macro time exceeded that number.

Part V

APPENDIX

A

UNRAVELLING THE INTERPLAY OF DYE PROPERTIES AND ANALYSIS PARAMETERS IN COPS ESTIMATIONS

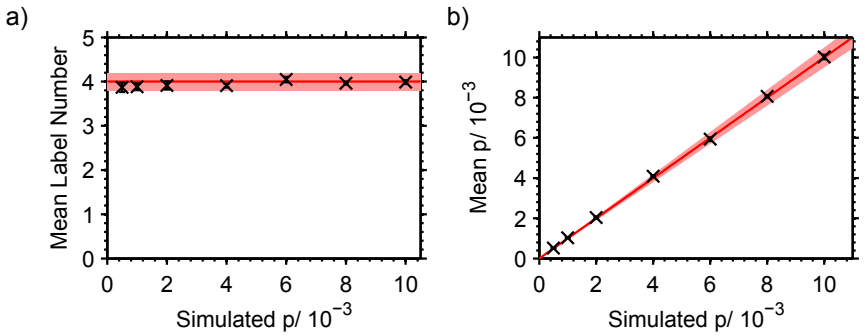

FIGURE A.1: CoPS analysis providing valid label number estimates for simulations with varying brightness. a), b) Comparison of estimated (mean and standard deviation of estimates in the plateau of valid label number estimates) with simulated detection probabilities and label number. The red line indicates the simulated detection probabilities and label number, respectively, with a 10 % window shaded in light red.

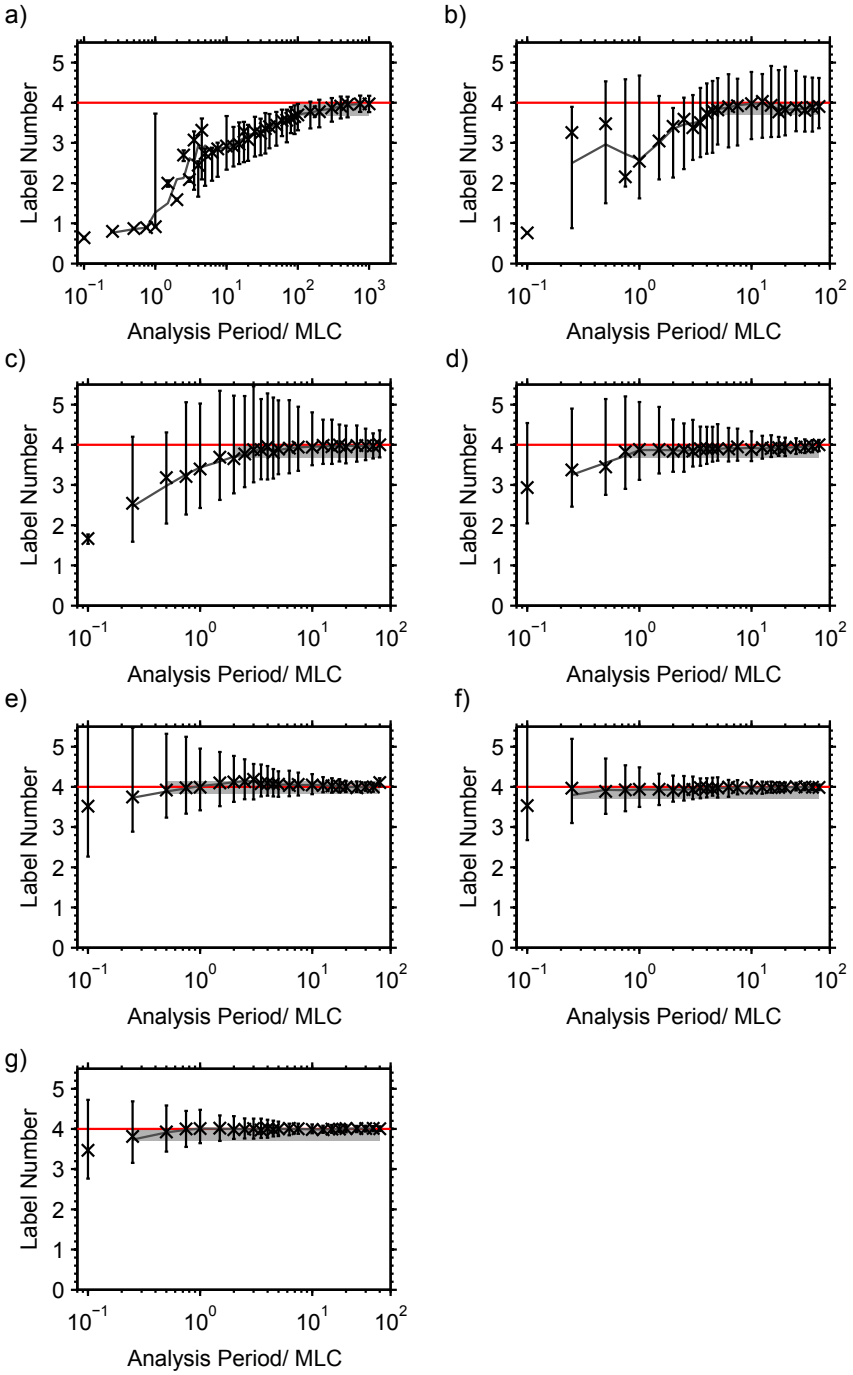

FIGURE A.2: Estimated label numbers for CoPS analysis of simulations with varying brightness. a)/ b)/ c)/ d)/ e)/ f)/ g) p = 0.5, 1, 2, 4, 6, 8 and 10×10^{-3} and p_b =0.5, 1, 2, 3, 4, 5 and 6×10^{-4}. The median label number estimate with $Q_{0.25}$ and $Q_{0.75}$ is shown in black. The dark grey line is the three point moving average of label number estimates and the plateau of valid CoPS estimates is shaded in grey. The red line indicates the simulated label number N=4.

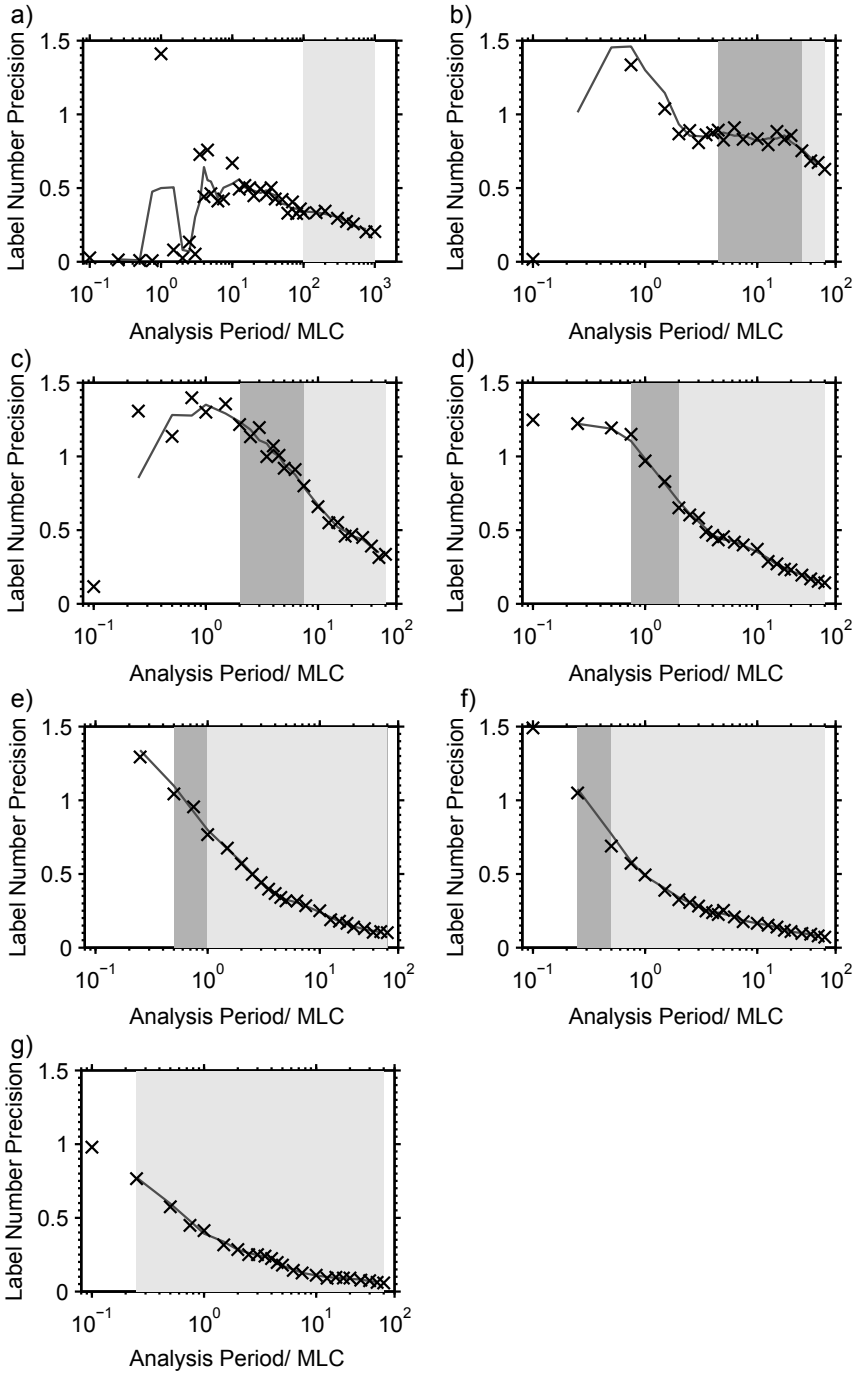

FIGURE A.3: Precision of estimated label numbers for CoPS analysis with varying brightness. a)/ b)/ c)/ d)/ e)/ f)/ g) $p = 0.5$, 1, 2, 4, 6, 8 and 10×10^{-3} and p_b =0.5, 1, 2, 3, 4, 5 and 6×10^{-4}. The dark grey line is the three point moving average of label number estimates and the plateau of valid CoPS estimates is shaded in grey. The red line indicates the simulated label number N=4. The plateau of valid CoPS estimates is shaded in dark grey, the dark grey line is the three point moving average of the precision of estimated label numbers and a precision $\frac{IQR}{2} \leq 20\,\%$ of simulated N is indicated in light grey.

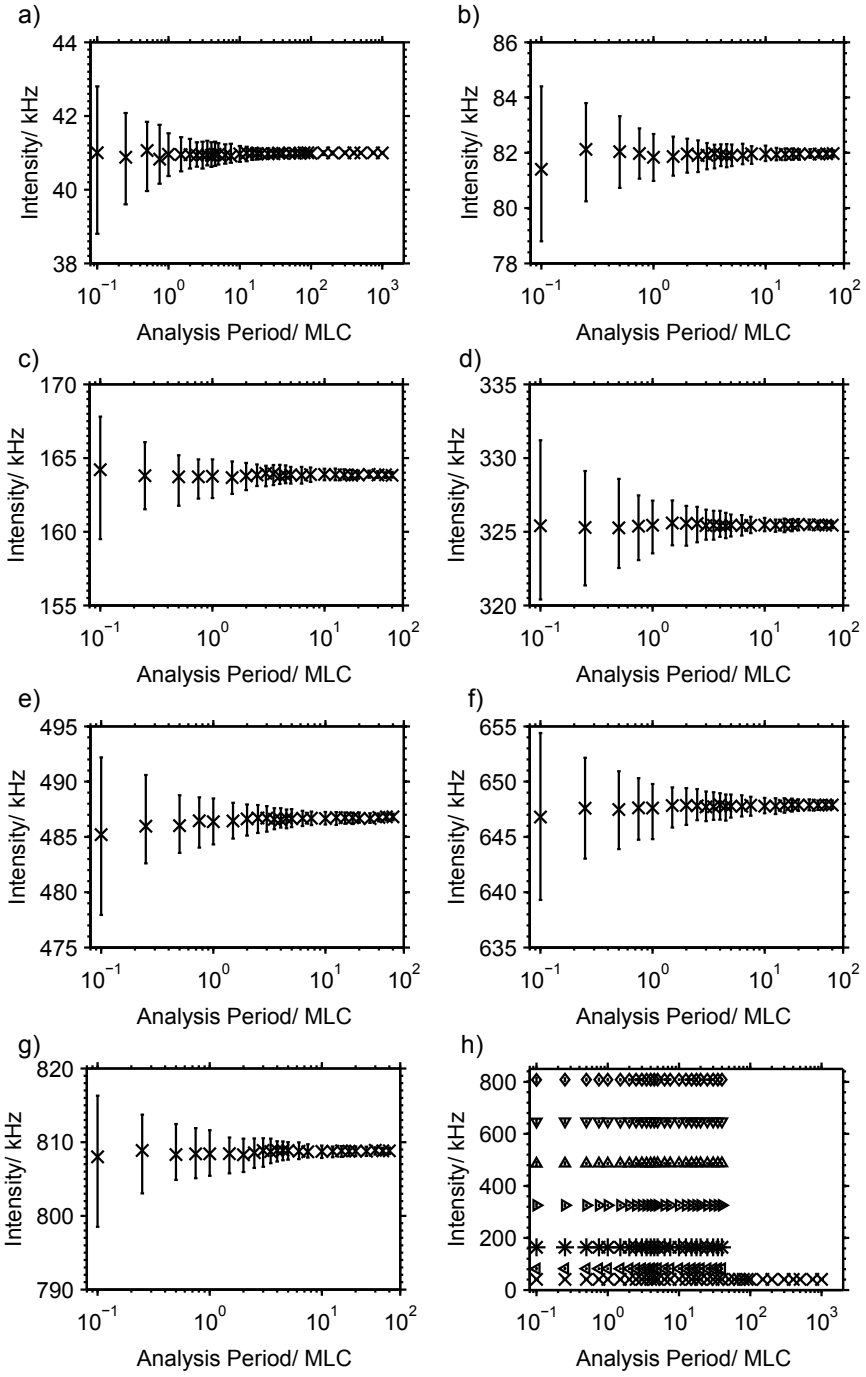

FIGURE A.4: Intensities for different analysis periods of simulations with varying brightness. a)/ b)/ c)/ d)/ e)/ f)/ g) $p = 0.5$, 1, 2, 4, 6, 8 and 10×10^{-3} and p_b =0.5, 1, 2, 3, 4, 5 and 6×10^{-4}. The median intensity with $Q_{0.25}$ and $Q_{0.75}$ is shown in black. h) Overview of the data in a) - g).

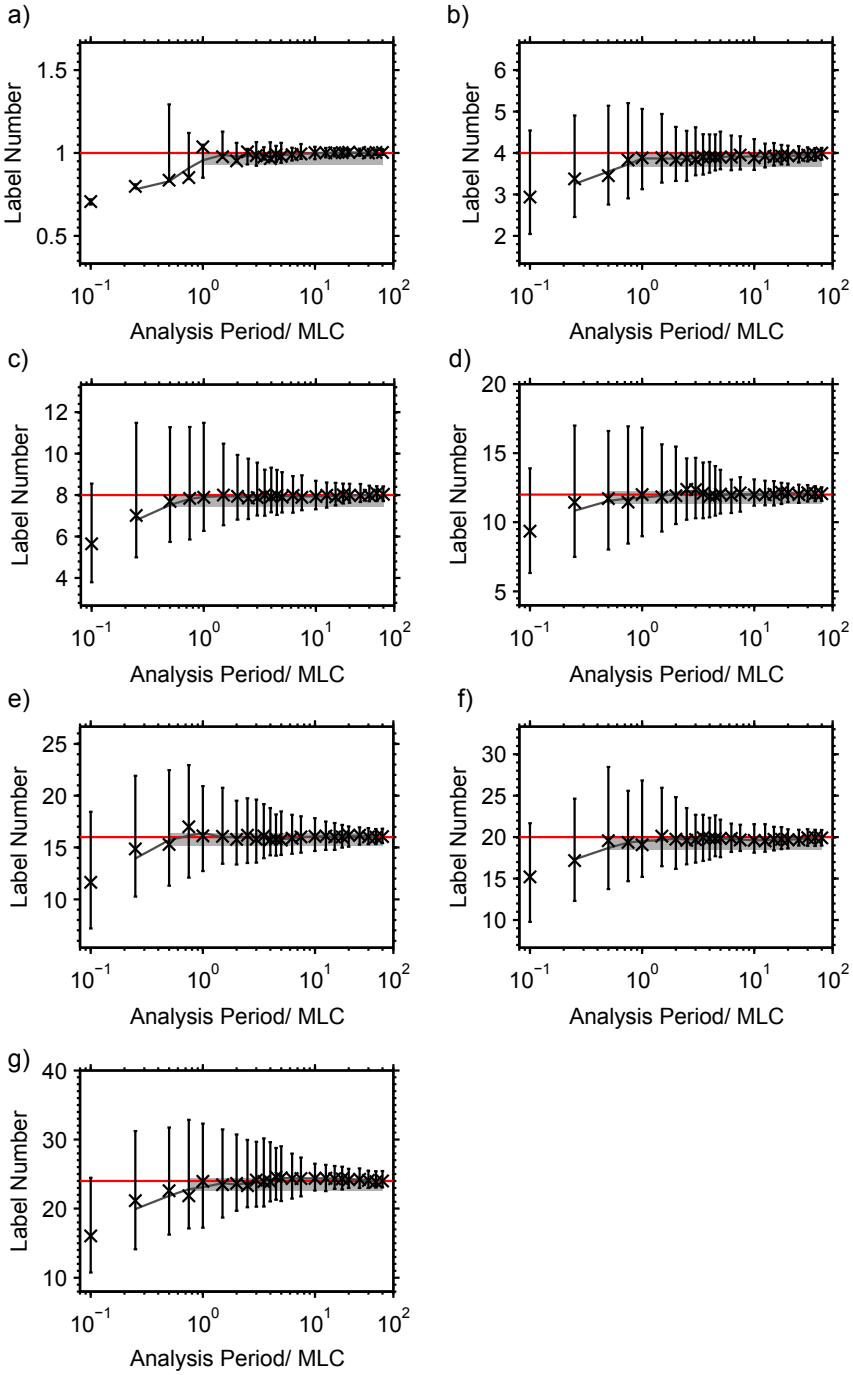

FIGURE A.5: Estimated label numbers for CoPS analysis of simulations with varying label number. a)/ b)/ c)/ d)/ e)/ f)/ g) Simulated parameters $p = 4 \times 10^{-3}$, $p_b = 3 \times 10^{-4}$ and N=1/ 4/ 8/ 12/ 16/ 20/ 24. The median label number estimate with $Q_{0.25}$ and $Q_{0.75}$ is shown in black. The dark grey line is the three point moving average of label number estimates and the plateau of valid CoPS estimates is shaded in grey. The red line indicates the simulated label number.

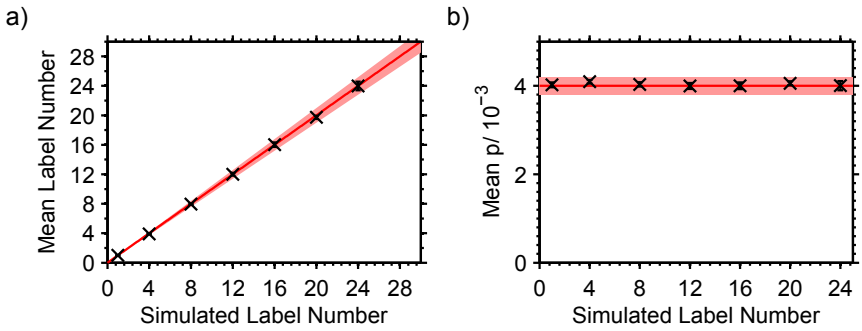

FIGURE A.6: Summary of CoPS analysis providing valid label number estimates for simulations with varying label number. a), b) Comparison of estimated (mean and standard deviation of estimates in the plateau of valid label number estimates) with simulated detection probabilities and label numbers. The red line indicates the simulated detection probabilities and label number, respectively, with a 10 % window shaded in light red.

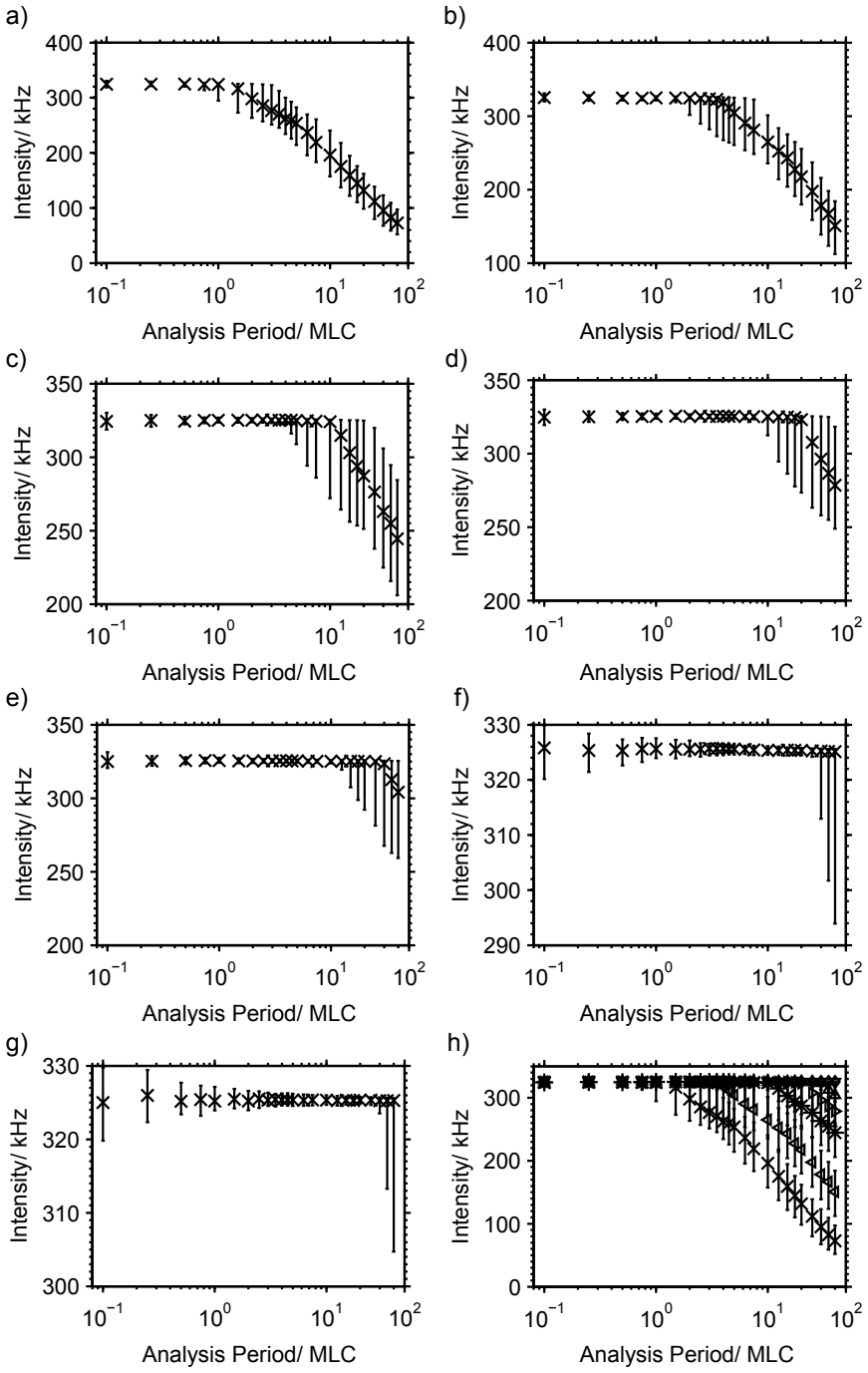

FIGURE A.7: Intensities for different analysis periods of simulations with varying photostability. a)/ b)/ c)/ d)/ e)/ f)/ g) Simulated parameters $p = 4 \times 10^{-3}$, $p_b = 3 \times 10^{-4}$ and τ_{ph}=10 MLC/ 20 MLC/ 60 MLC/ 100 MLC/ 200 MLC/ 300 MLC/ 400 MLC or 0.5 s/ 1 s/ 3 s/ 5 s/ 10 s/ 15 s/ 20 s. The median intensity with $Q_{0.25}$ and $Q_{0.75}$ is shown in black. h) Overview of the data in a) - g).

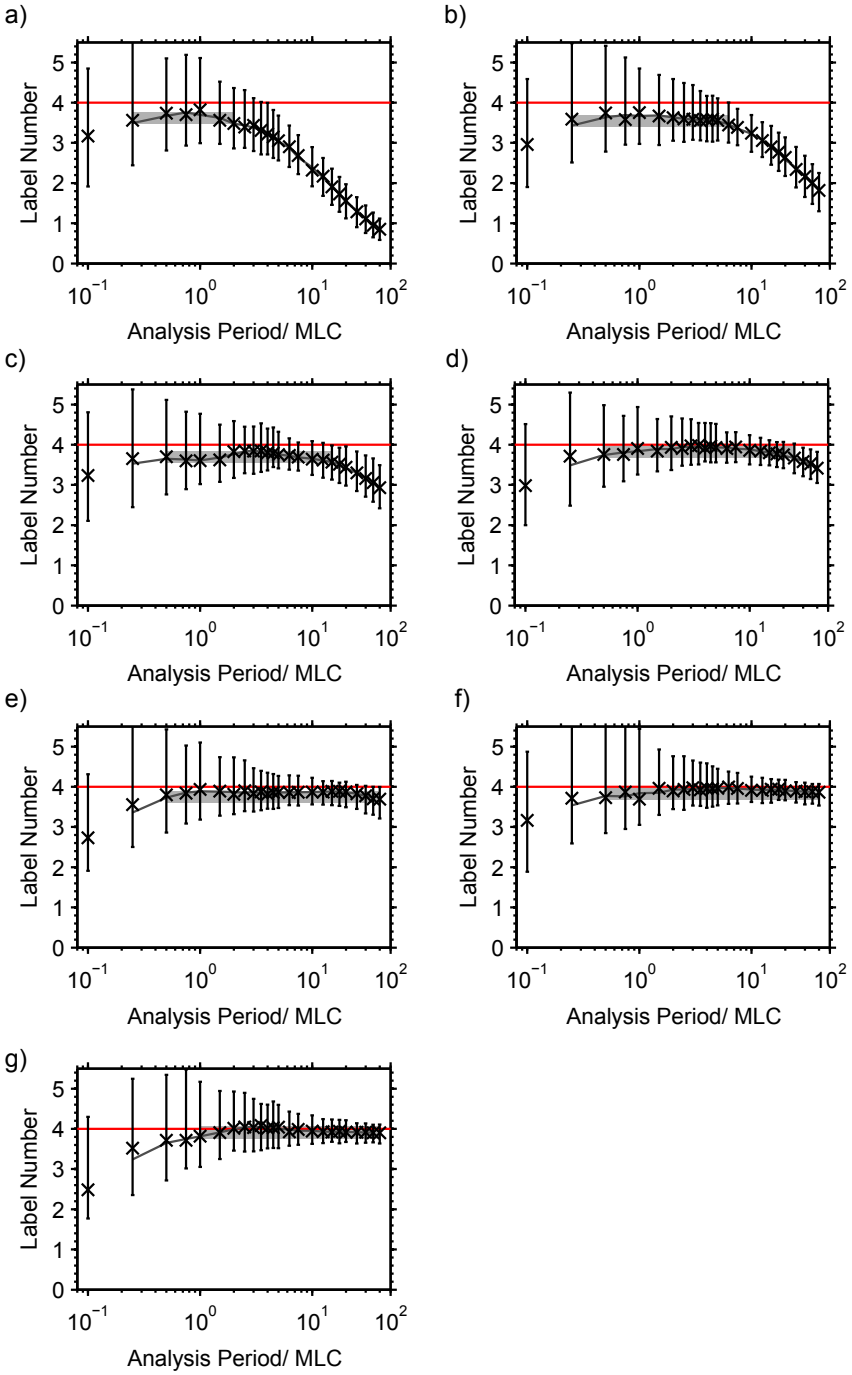

FIGURE A.8: Estimated label numbers for CoPS analysis of simulations with varying photostability. a)/ b)/ c)/ d)/ e)/ f)/ g) Simulated parameters $p = 4 \times 10^{-3}$, $p_b = 3 \times 10^{-4}$ and τ_{ph}=10 MLC/ 20 MLC/ 60 MLC/ 100 MLC/ 200 MLC/ 300 MLC/ 400 MLC or 0.5 s/ 1 s/ 3 s/ 5 s/ 10 s/ 15 s/ 20 s. The median label number estimate with $Q_{0.25}$ and $Q_{0.75}$ is shown in black. The dark grey line is the three point moving average of label number estimates and the plateau of valid CoPS estimates is shaded in grey. The red line indicates the simulated label number.

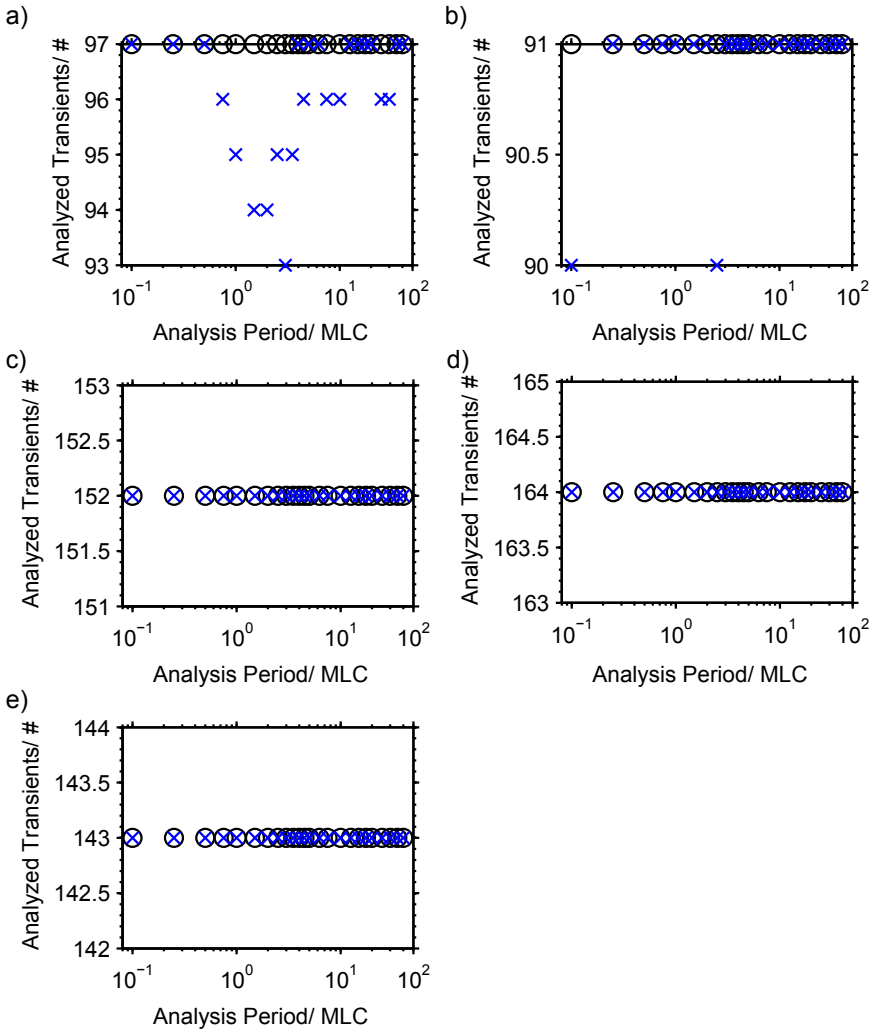

FIGURE A.9: Number of analyzed traces for CoPS analysis of tetraProbes with varying laser excitation power. a)/ b)/ c)/ d) Measurements with tetraAtto633 and 2.5 µW/5 µW/10 µW/20 µW laser excitation power. e) Measurements with tetraAtto647N and 20 µW laser excitation power. The repetition rate of the 640 nm laser was 20 MHz. Black circles: Number of traces submitted to CoPS analysis, blue crosses: Number of successfully fitted traces.

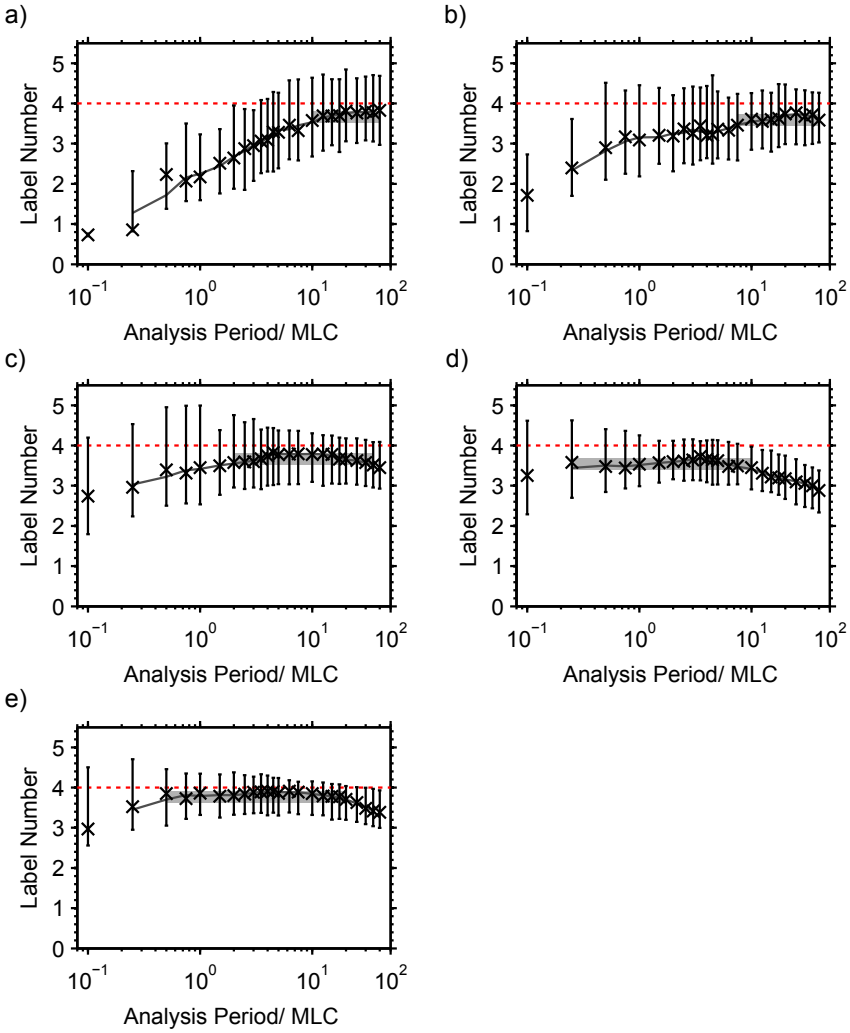

FIGURE A.10: Estimated label numbers for CoPS analysis with varying analysis period. a)/ b)/ c)/ d) Measurements with tetraAtto633 and 2.5 µW/5 µW/10 µW/20 µW laser excitation power. e) Measurements with tetraAtto647N and 20 µW laser excitation power. The repetition rate of the 640 nm laser was 20 MHz. The median label number estimate with $Q_{0.25}$ and $Q_{0.75}$ is shown in black. The dark grey line is the three point moving average of label number estimates and the plateau of valid CoPS estimates is shaded in grey. The dotted red line indicates the designed label number.

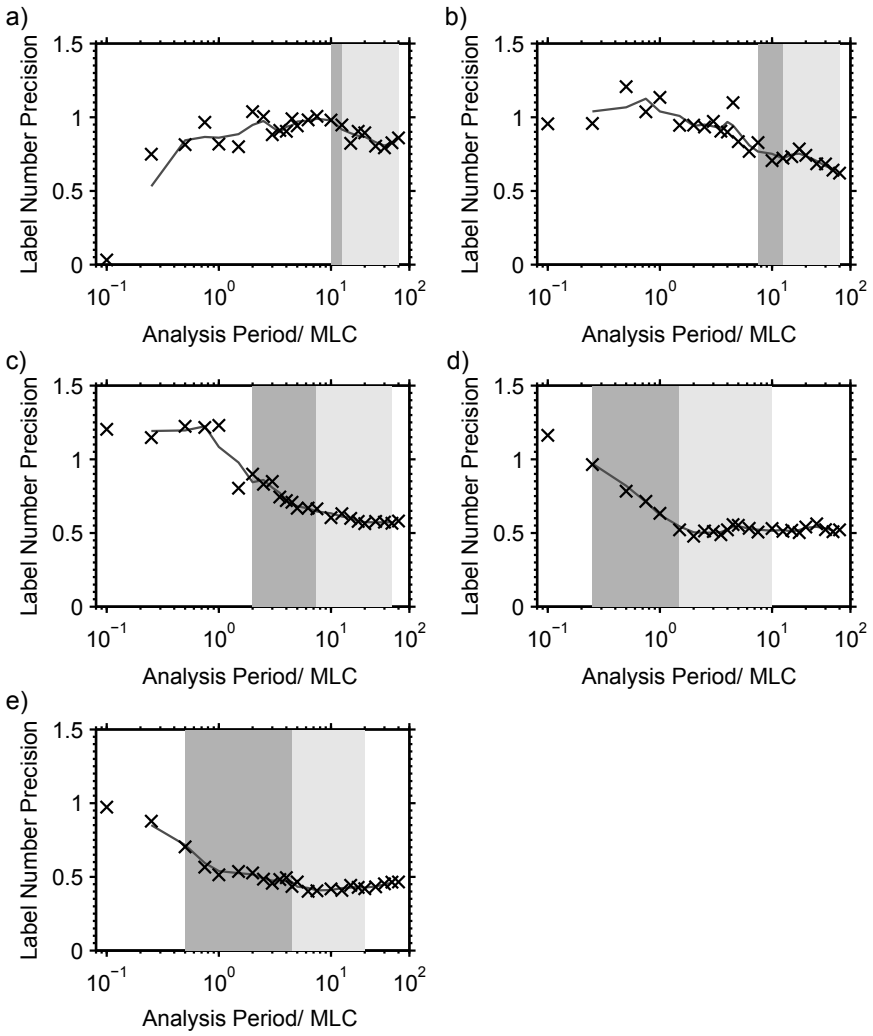

FIGURE A.11: Precision of estimated label numbers for CoPS analysis with varying analysis period. a)/ b)/ c)/ d) Measurements with tetraAtto633 and 2.5 µW/5 µW/10 µW/20 µW laser excitation power. e) Measurements with tetraAtto647N and 20 µW laser excitation power. The repetition rate of the 640 nm laser was 20 MHz. The plateau of valid CoPS estimates is shaded in grey, the dark grey line is the three point moving average of the precision of estimated label numbers and a precision $\frac{IQR}{2}$ with MA $\leq$ 1.15 MA_{min} is indicated in light grey.

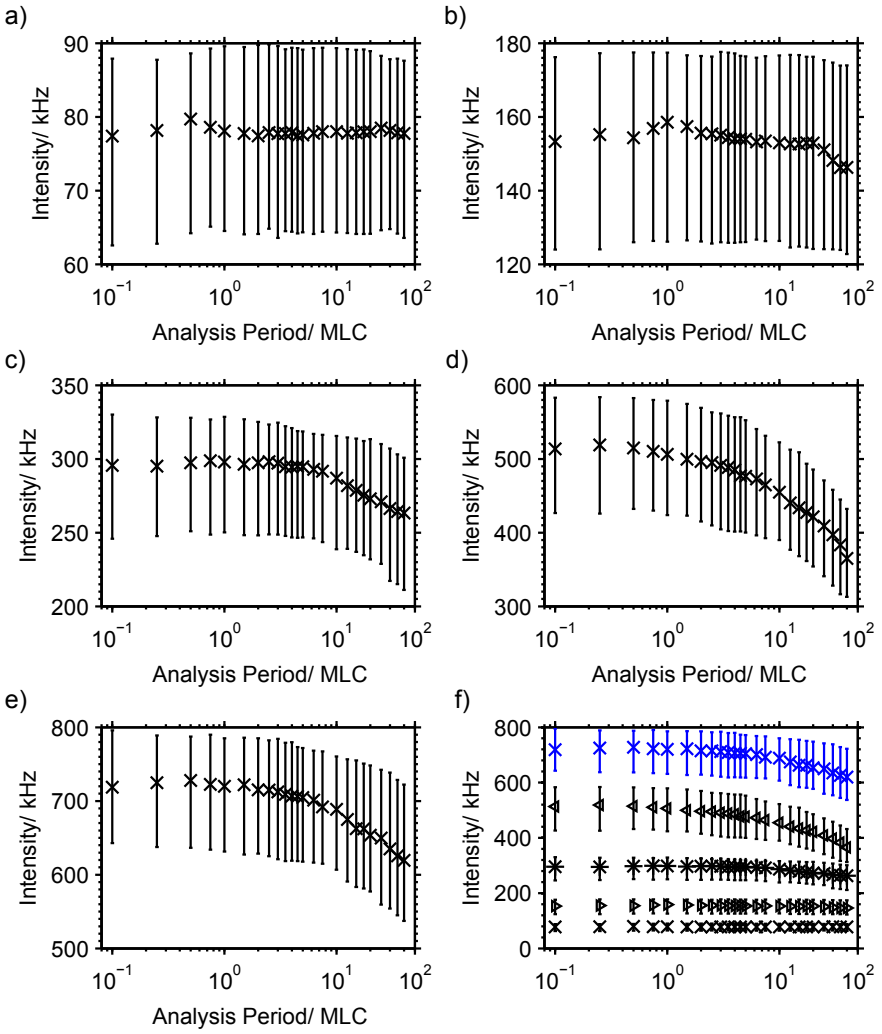

FIGURE A.12: Intensities for different analysis periods. a)/ b)/ c)/ d) Measurements with tetraAtto633 and 2.5 µW/5 µW/10 µW/20 µW laser excitation power. e) Measurements with tetraAtto647N and 20 µW laser excitation power. The repetition rate of the 640 nm laser was 20 MHz. The median intensity with $Q_{0.25}$ and $Q_{0.75}$ is shown in black. f) Overview of the data with tetraAtto633 presented in a) - d) in black, data with tetraAtto647N from e) in blue.

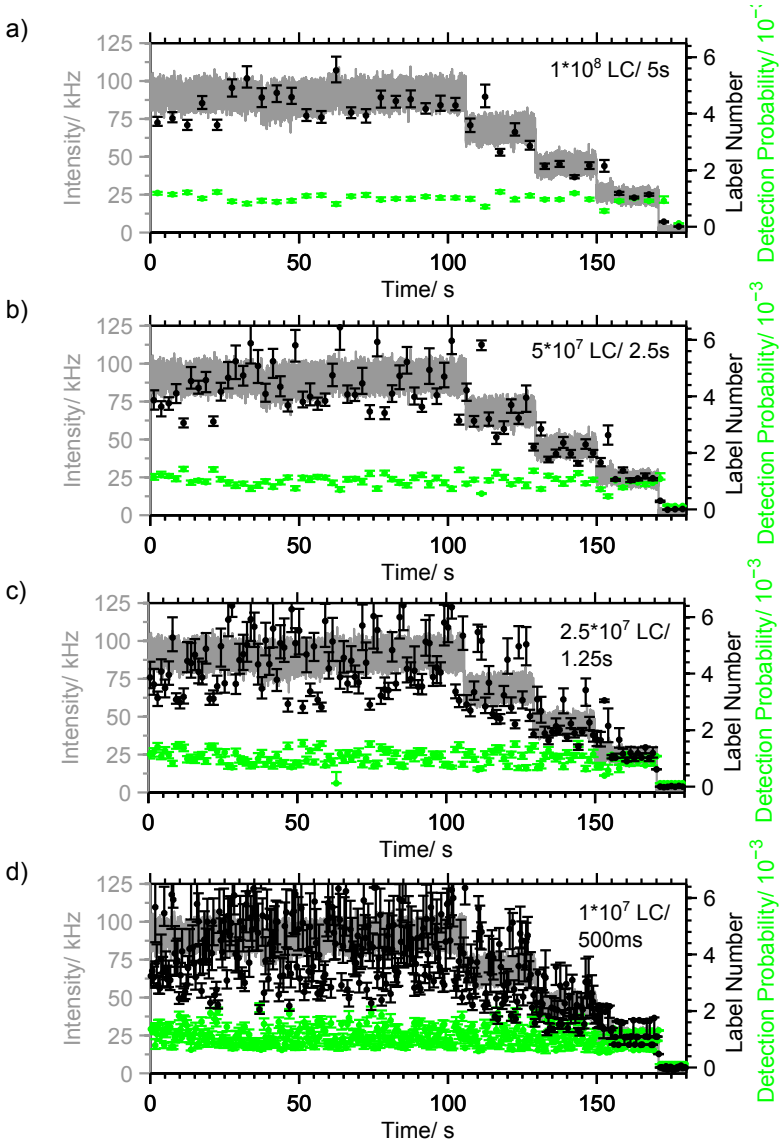

FIGURE A.13: Single molecule tetraAtto633 CoPS analysis with different analysis periods and 2.5 µW laser excitation power at 640 nm and a repetition rate of 20 MHz. CoPS estimates with a time resolution (= analysis period τ_{acq}) of 1×10^8 LC, 5×10^7 LC, 2.5×10^7 LC and 1×10^7 LC or 5 s, 2.5 s, 1.25 s and 0.5 s correlate with intensity bleaching steps. Black/green: Label number/ detection probability estimates with error bars derived from resampling algorithm, grey: Intensity.

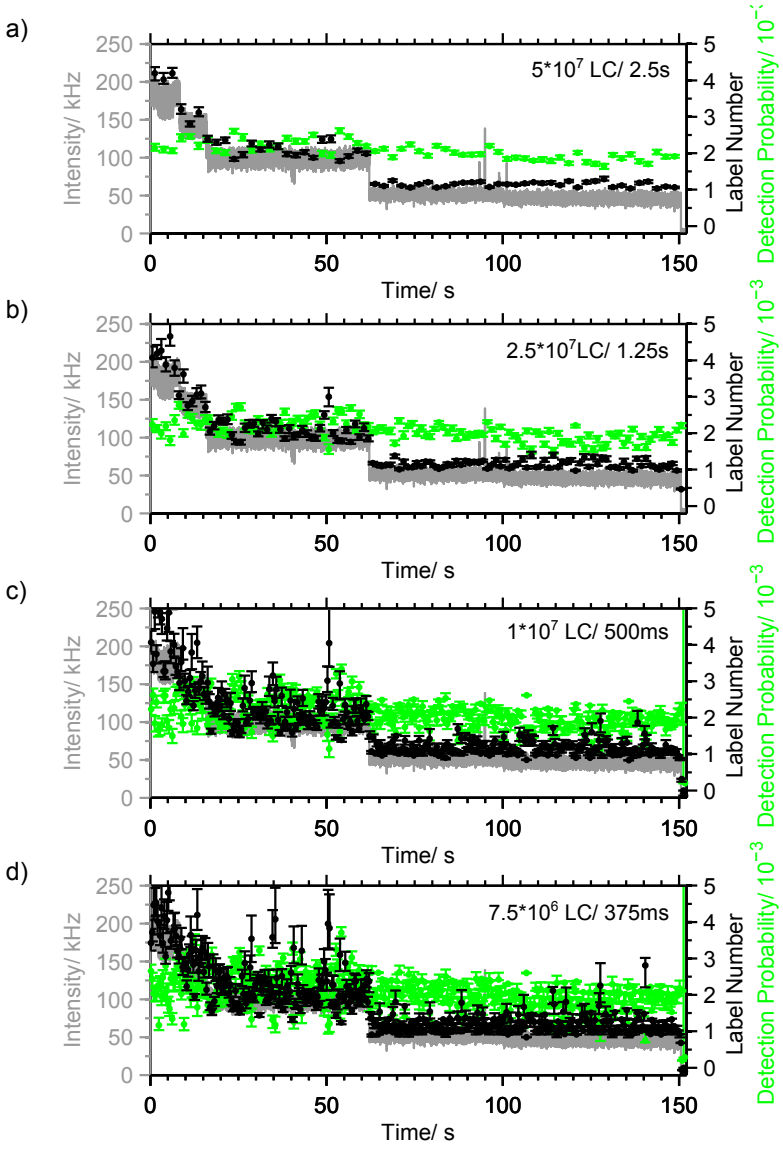

FIGURE A.14: Single molecule tetraAtto633 CoPS analysis with different analysis periods and 5 µW laser excitation power at 640 nm and a repetition rate of 20 MHz. CoPS estimates with a time resolution (= analysis period τ_{acq}) of 5×10^7 LC, 2.5×10^7 LC, 1×10^7 LC and 0.75×10^7 LC or 2.5 s, 1.25 s, 0.5 s and 0.375 s correlate with intensity bleaching steps. Black/green: Label number/ detection probability estimates with error bars derived from resampling algorithm, grey: Intensity.

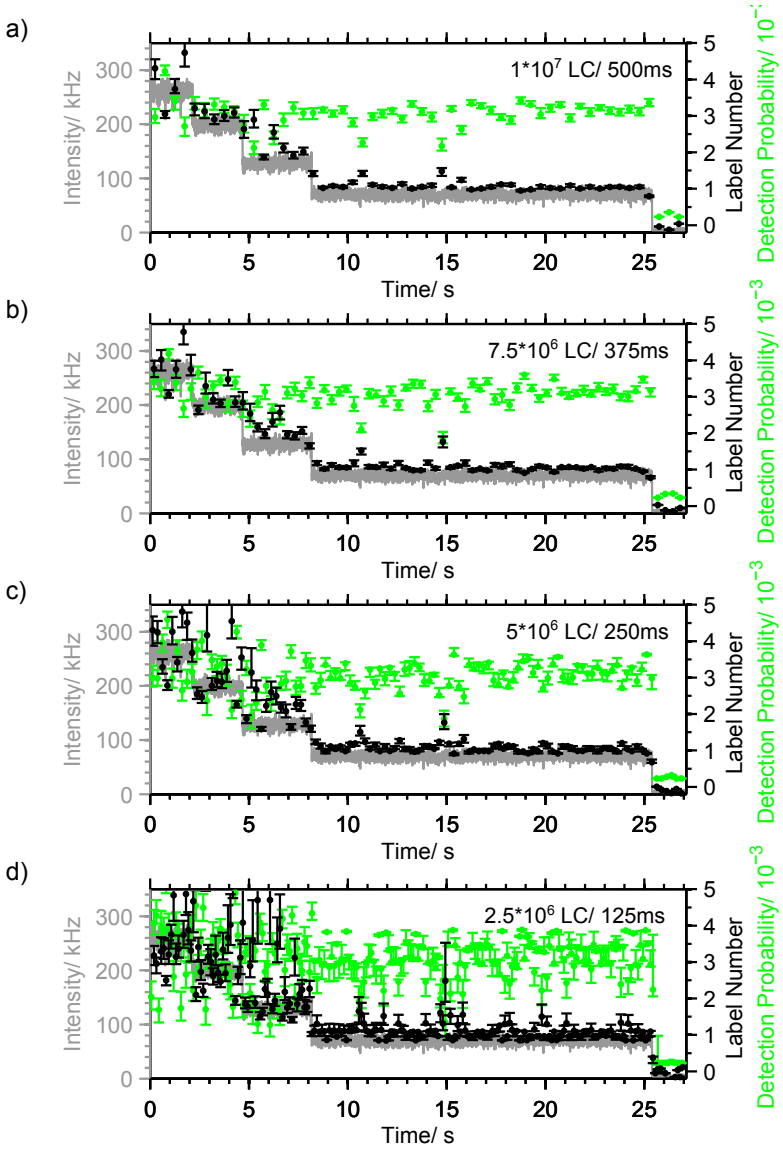

FIGURE A.15: Single molecule tetraAtto633 CoPS analysis with different analysis periods and 10 µW laser excitation power at 640 nm and a repetition rate of 20 MHz. CoPS estimates with a time resolution (= analysis period τ_{acq}) of 10×10^6 LC, 7.5×10^6 LC, 5×10^6 LC and 2.5×10^6 LC or 500 ms, 375 ms, 250 ms and 125 ms correlate with intensity bleaching steps. Black/green: Label number/ detection probability estimates with error bars derived from resampling algorithm, grey: Intensity.

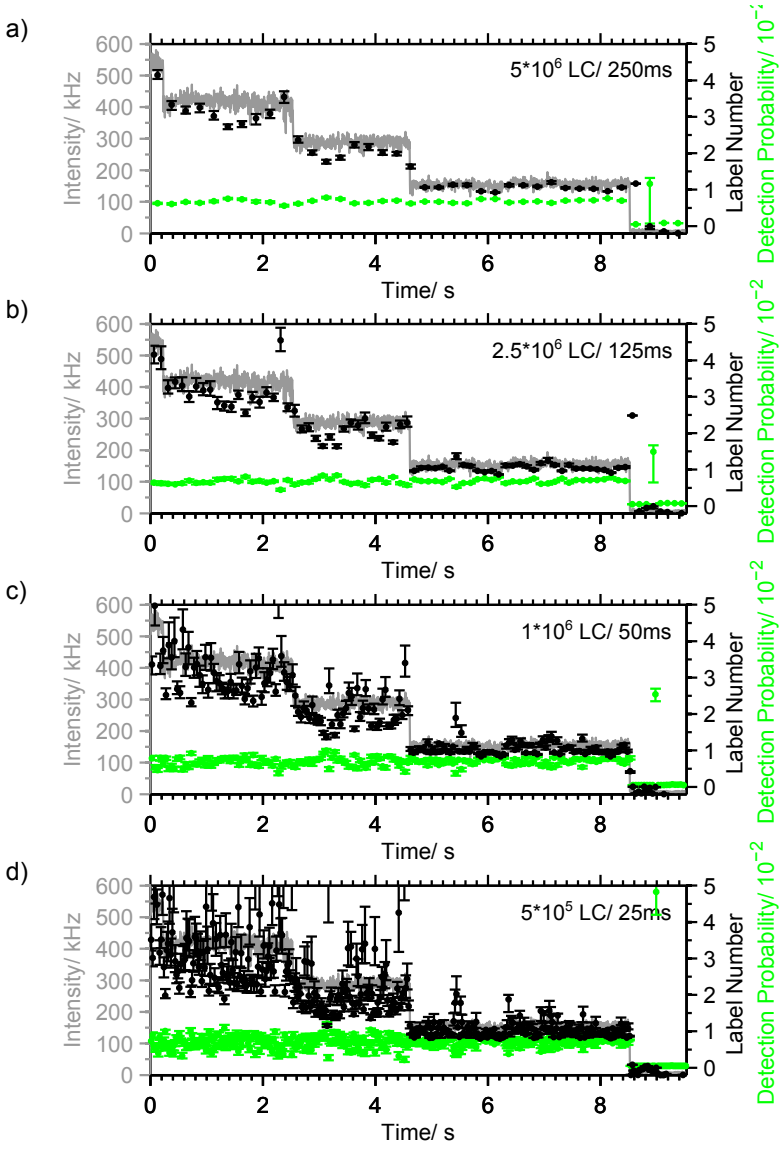

FIGURE A.16: Single molecule tetraAtto633 CoPS analysis with different analysis periods and 20 µW laser excitation power at 640 nm and a repetition rate of 20 MHz. CoPS estimates with a time resolution (= analysis period τ_{acq}) of 5×10^6 LC, 2.5×10^6 LC, 1×10^6 LC and 0.5×10^6 LC or 250 ms, 125 ms, 50 ms and 25 ms correlate with intensity bleaching steps. Black/green: Label number/ detection probability estimates with error bars derived from resampling algorithm, grey: Intensity.

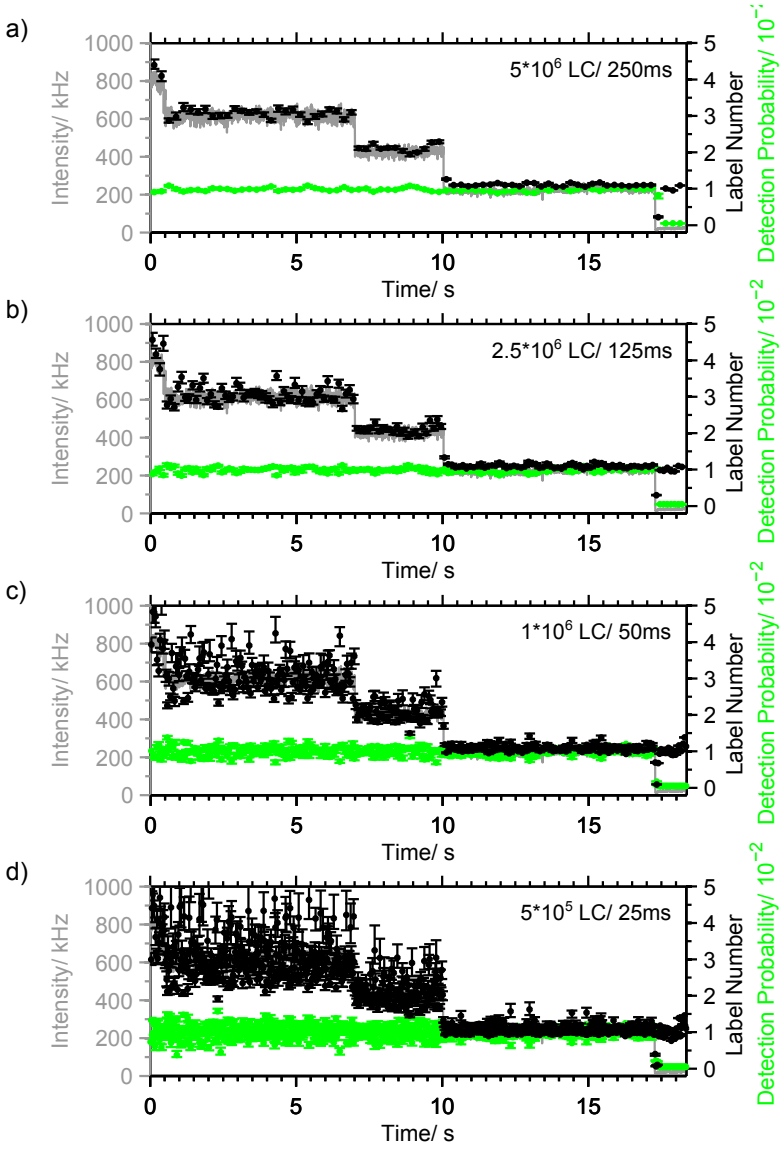

FIGURE A.17: Single molecule tetraAtto647N CoPS analysis with different analysis periods and 20 µW laser excitation power at 640 nm and a repetition rate of 20 MHz. CoPS estimates with a time resolution (= analysis period τ_{acq}) of 5×10^6 LC, 2.5×10^6 LC, 1×10^6 LC and 0.5×10^6 LC or 250 ms, 125 ms, 50 ms and 25 ms correlate with intensity bleaching steps. Black/green: Label number/ detection probability estimates with error bars derived from resampling algorithm, grey: Intensity.

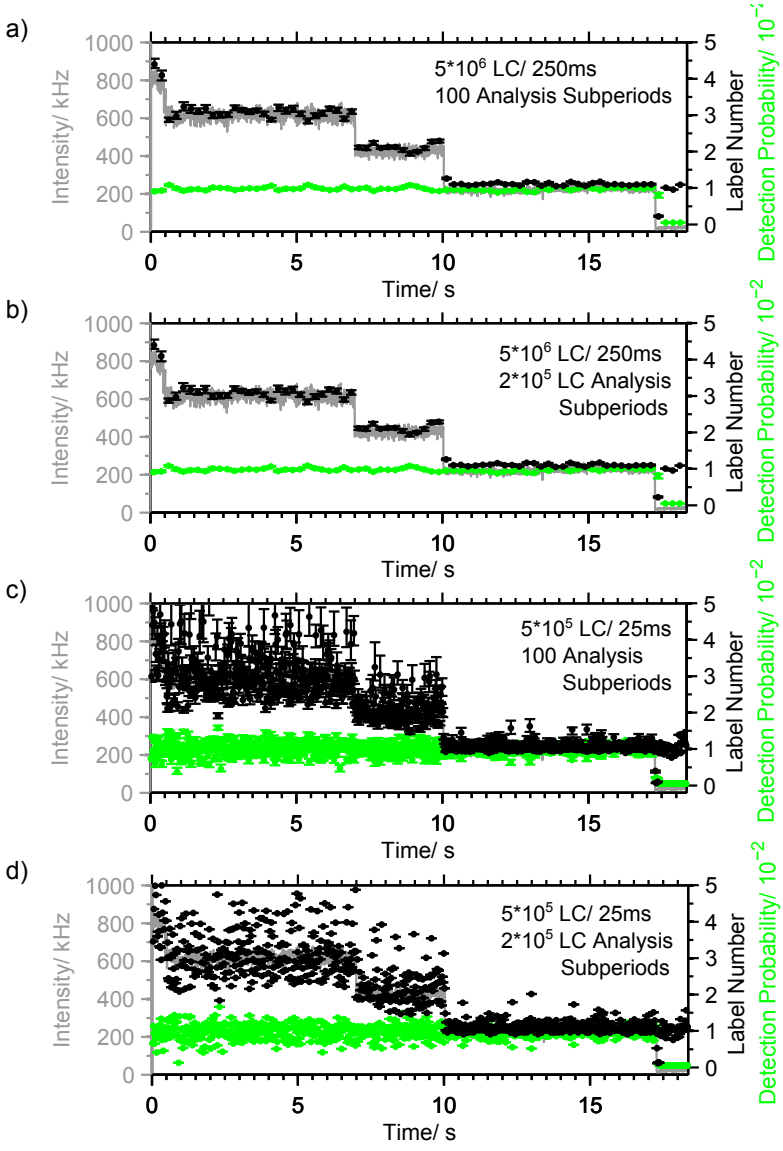

FIGURE A.18: Single molecule tetraAtto647N CoPS analysis with different analysis periods and analysis subperiods, 20 µW laser excitation power at 640 nm and a repetition rate of 20 MHz. CoPS estimates with a time resolution (= analysis period τ_{acq}) of 5×10^6 LC and 0.5×10^6 LC or 250 ms and 25 ms correlate with intensity bleaching steps. The error for single measurements is unterestimated for constant analysis subperiods at lower analysis periods. Black/green: Label number/ detection probability estimates with error bars derived from resampling algorithm, grey: Intensity.

B

ORGANIC DYES FOR COPS ACROSS THE VISIBLE SPECTRUM

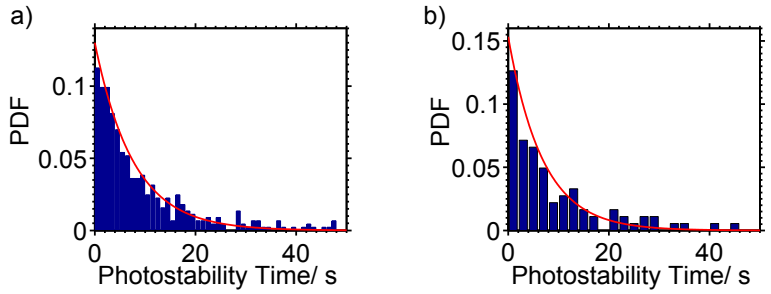

FIGURE B.19: Histogram of photostability times for measurements with Atto647N. Figure S3 of [49]. Red line: monoexponential fit to the normalized histogram (=PDF). τ_{ph}= estimated parameter (95 % confidence intervals). a) DNA hybridization probe with 10 µW laser excitation power at 635 nm and a repetition rate of 20 MHz, bin size=1 s, τ_{ph}=7.6 s(0.4 s) b) SNAP-tag with 5 µW laser excitation power at 640 nm and a repetition rate of 20 MHz, bin size=2 s, τ_{ph}=6.8 s(1.1 s).

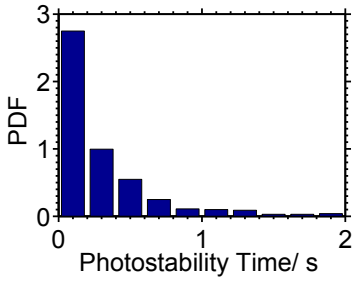

FIGURE B.20: Normalized histogram (=PDF) of photostability times for measurements with Atto488. DNA hybridization probe with 6.75 µW laser excitation power at 470 nm and a repetition rate of 20 MHz, bin size=0.2 s

TABLE 8: Fluorescence properties and brightness comparison of dyes in the red wavelength regime. Table S1 of [49], modified.

	Atto647N	Atto633	Cy5	Alexa647	AbberiorStar635	SiR
λ_{abs} / nm	644	629	649	650	634	652
λ_{em} / nm	669	657	670	665	654	674
ϵ_{max} / $M^{-1}\,cm^{-1}$	1.5	1.3	2.5	2.39	0.6	1,0
ϵ_{635} / $M^{-1}\,cm^{-1}$	1.15	1.21	2.1	1.5	0.57	0.74
Q_f	0.65	0.64	>0.28	0.33	0.51	0.39
B=$\epsilon_{635} \cdot Q_f$ / $M^{-1}\,cm^{-1}$	0.75	0.77	>0.58	0.49	0.29	0.28

TABLE 9: Degree of labeling of DNA hybridization probe with different fluorophores in the red wavelength regime measured by ensemble absorption spectroscopy and number of probes N measured in single molecule experiments. Table S2 of [49], modified.

	Atto647N	Atto633	Cy5	Alexa647	AbberiorStar635	SiR
DOL REP'	0.7±0.1	0.7±0.1	0.9±0.2	0.9±0.2	2.1±0.4	1.4±0.3
DOL REP_4	1.12±0.2	0.9±0.2	1.4±0.3	0	0	0
N / # 5/ 10	166/ 115	158/ 148	165/ 156	210/ 125	176/ 201	157/ 154

TABLE 10: Fluorescence properties and brightness comparison of dyes in the green/yellow wavelength regime.

	Cy3B	Atto550	Atto565	AttoRho6G	Alexa532	Atto532
λ_{abs} / nm	559	554	563	535	532	532
λ_{em} / nm	570	576	592	560	554	553
ϵ_{max} / $M^{-1}\,cm^{-1}$	1.3	1.2	1.2	1.15	0.81	1.15
ϵ_{532} / $M^{-1}\,cm^{-1}$	0.78	0.48	0.46	1.13	0.81	1.15
Q_f	>0.67	0.8	0.9	0.9	0.61	0.9
B=$\epsilon_{532} \cdot Q_f$ / $M^{-1}\,cm^{-1}$	>0.52	0.38	0.41	1.02	0.49	1.04

TABLE 11: Degree of labeling of DNA hybridization probe with different fluorophores in the green/yellow wavelength regime measured by ensemble absorption spectroscopy and number of probes N measured in single molecule experiments. In addition, the percentage of traces with clearly identifiable photobleaching steps is given.

	Cy3B	Atto550	Atto565	AttoRho6G	Alexa532	Atto532
DOL REP'	1.84±0.4	1±0.2	0.85±0.2	0.91±0.2	1.53±0.3	0.99±0.2
DOL REP_4	0	0	0	0	0	0
N / # high/ low laser power	127/ 123	149/ 156	149/ 198	130/ 107	148/ -	150/ -
N / % clear steps high/ low laser power	100/ 100	0.54/ 0.63	0.46/ 0.39	0.84/ 0.82	0.94/ -	0.81/ -

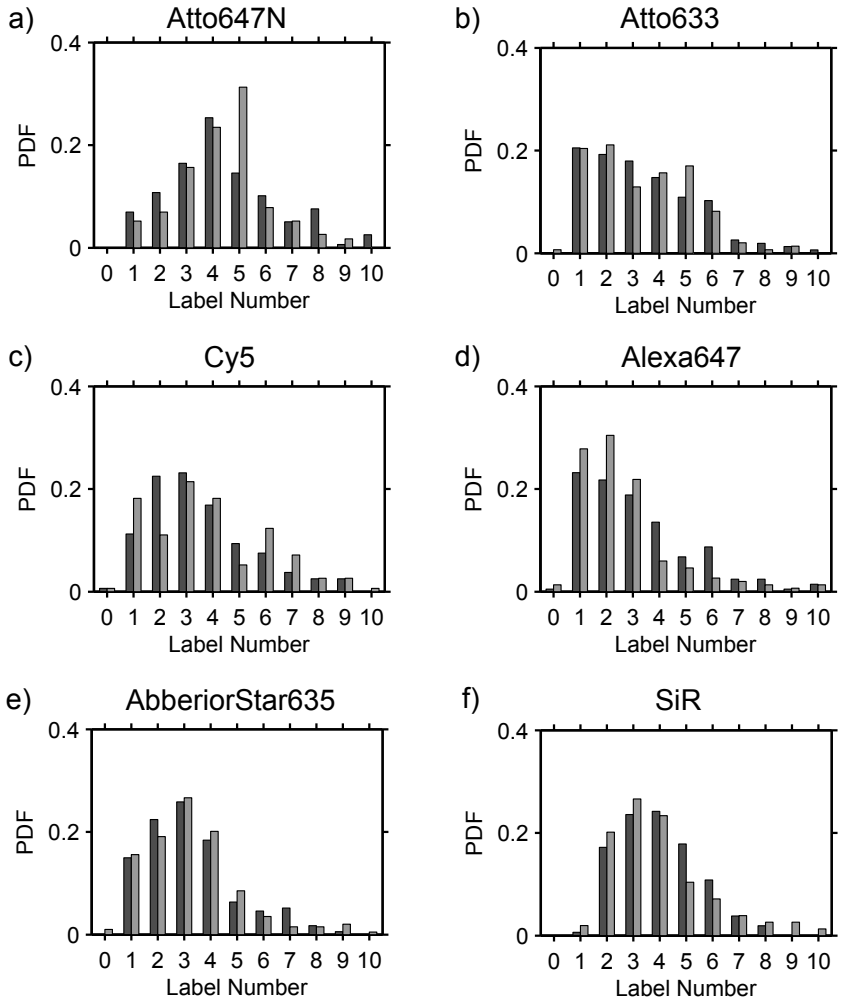

FIGURE B.21: Label number distributions for DNA hybridization probes with different fluorophores in the red wavelength regime. Figure S1 of [49]. Normalized label number distributions (PDF) determined by CoPS for 5 µW (dark grey) and 10 µW (grey) laser excitation power at 635 nm and a repetition rate of 20 MHz. Measurements for SiR were conducted at 640 nm. Analysis period t_{acq}=2.5 MLC or 125 ms. The measurement for SiR with 5 µW laser excitation was analyzed with t_{acq}=10 MLC or 500 ms. a) Atto647N, b) Atto633, c) Cy5, d) Alexa647, e) AbberiorStar635, f) SiR.

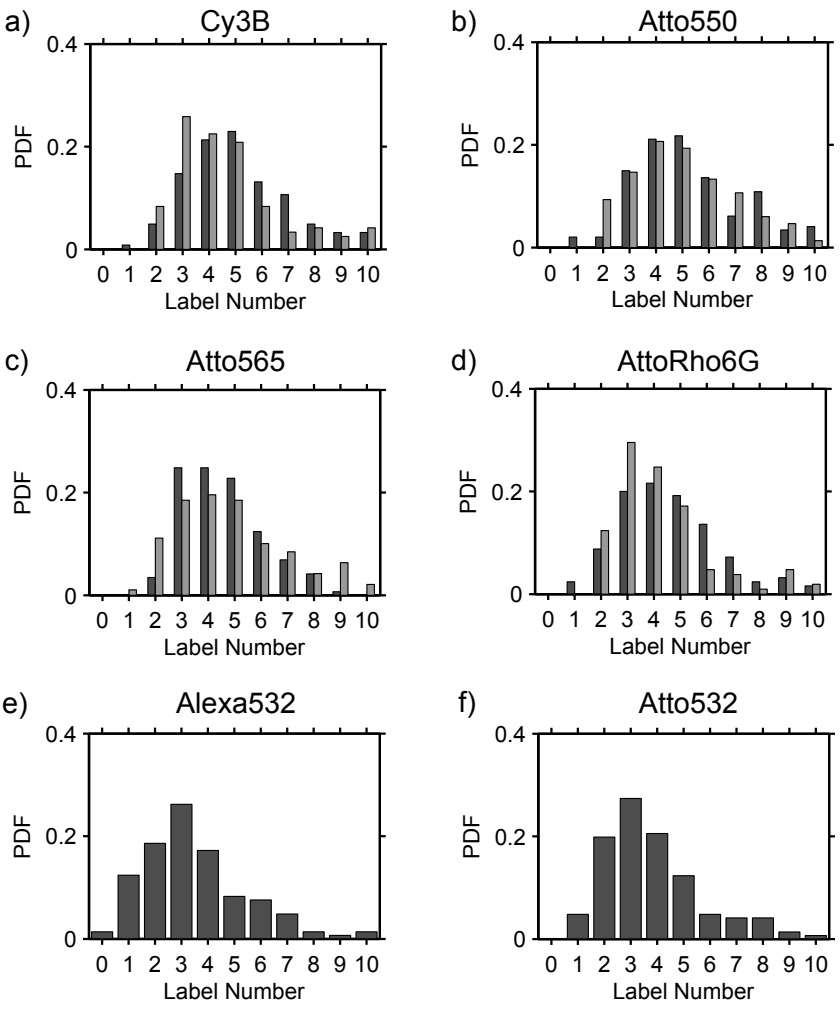

FIGURE B.22: Label number distributions for DNA hybridization probes with different fluorophores in the green/yellow wavelength regime. Normalized label number distributions (PDF) determined by CoPS for : low (darg grey) and high (light grey) laser excitation power (6 µW and 12 µW for Cy3B, AttoRho6G, Alexa532 and Atto532, 12 µW and 24 µW for Atto550 and Atto565) at 532 nm and a repetition rate of 20 MHz. CoPS analysis with t_{acq}=10 MLC or 500 ms for low and t_{acq}=2.5 MLC or 125 ms for high laser excitation power. a) Cy3B, b) Atto550, c) Atto565, d) AttoRho6G, e) Alexa532, f) Atto532.

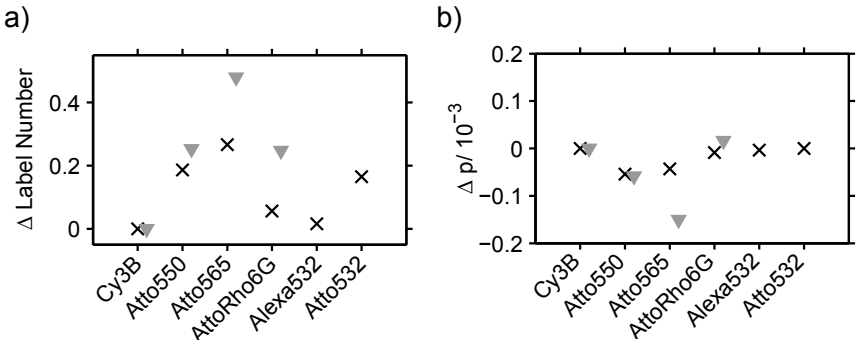

FIGURE B.23: Difference of CoPS analysis of DNA hybridization probes for all traces versus traces with clearly identifiable photobleaching steps for dyes in the green/yellow wavelength regime. The percentage of traces with clearly identifiable photobleaching steps is given in Table 11. Black crosses/ light grey downward-pointing triangles: low and high laser excitation power (6 µW and 12 µW for Cy3B, AttoRho6G, Alexa532 and Atto532, 12 µW and 24 µW for Atto550 and Atto565) at 532 nm and a repetition rate of 20 MHz. a)/ b) Difference in estimated detection probabilities/ label numbers (median(all) - median(clear steps)) for CoPS analysis with t_{acq}=10 MLC or 500 ms for low and t_{acq}=2.5 MLC or 125 ms for high laser excitation power.

TABLE 12: Fluorescence properties and brightness comparison of dyes in the blue/green wavelength regime.

	Atto488	Alexa488	OregonGreen488 (6-Isomer)	OregonGreen514
λ_{abs} / nm	501	495	495	506
λ_{em} / nm	523	519	516	526
ϵ_{max} / $M^{-1}\,cm^{-1}$	0.9	0.71	0.82	0.85
ϵ_{470} / $M^{-1}\,cm^{-1}$	0.33	0.33	0.35	0.22
Q_f	0.8	0.92	0.92	-
B=$\epsilon_{470} \cdot Q_f$ / $M^{-1}\,cm^{-1}$	0.26	0.30	0.32	-

TABLE 13: Degree of labeling of DNA hybridization probe with different fluorophores in the blue/green wavelength regime measured by ensemble absorption spectroscopy and number of probes N measured in single molecule experiments.

	Atto488	Alexa488	OregonGreen488 (6-Isomer)	OregonGreen514
DOL REP'	1.0±0.2	1.2±0.2	0.8±0.2	1.1±0.2
DOL REP_4	0	0.75±0.2	0	0
N / # 3.3/ 6.75/13.5	131/ 233/177	217/176/135	248/225/213	162/159/159

C

LABEL NUMBER DISTRIBUTION OF FLUORESCENT MARKERS

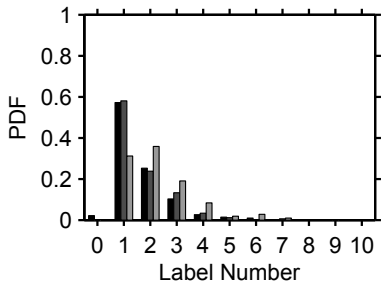

FIGURE C.24: Label number distributions for anti-GFP-antibody with different dye-to-protein ratio. Figure S4 of [49]. Laser excitation power 5 µW at 640 nm with a repetition rate of 20 MHz, FOV-scan $\leq$3 µW. Analysis period 2.5 MLC or 125 ms. Black: Alexa647 label ratio 3:1, dark grey: Atto647N label ratio 3:1, light grey: Atto647N label ratio 10:1.

TABLE 14: Comparison of ensemble and single molecule CoPS measurements of labeled anti-GFP antibody with different label numbers and classification of photophysical properties. Table S3 of [49]. Degree of labeling (DOL) measured by ensemble absorption spectroscopy with a relative error of 20 %. Average label number (ALN) with standard error of the mean (SEM) and standard deviation (σ) determined from CoPS analysis and median of the label number (MLN) distribution with 15.9 and 84.1 % quantiles. Percentage of fluorescent transients that display rapid fluctuations in intensity along with the total number of investigated transients in brackets.

	anti-GFP antibody-Alexa647	anti-GFP antibody-Atto647N lower DOL	anti-GFP antibody-Atto647N higher DOL
DOL$\pm\Delta$DOL	2.1$\pm$0.4	1.4$\pm$0.2	2.9$\pm$0.6
ALN$\pm$SEM(σ)	1.70$\pm$0.05(1.00)	1.71$\pm$0.07(0.95)	2.22$\pm$0.09(1.26)
MLN ($Q_{0.159}$, $Q_{0.841}$)	1.4(0.9,2.5)	1.3(1.0,2.6)	1.9(1.0,3.4)
Blinking(total)/ %(#)	7(459)	60(182)	88 (223)

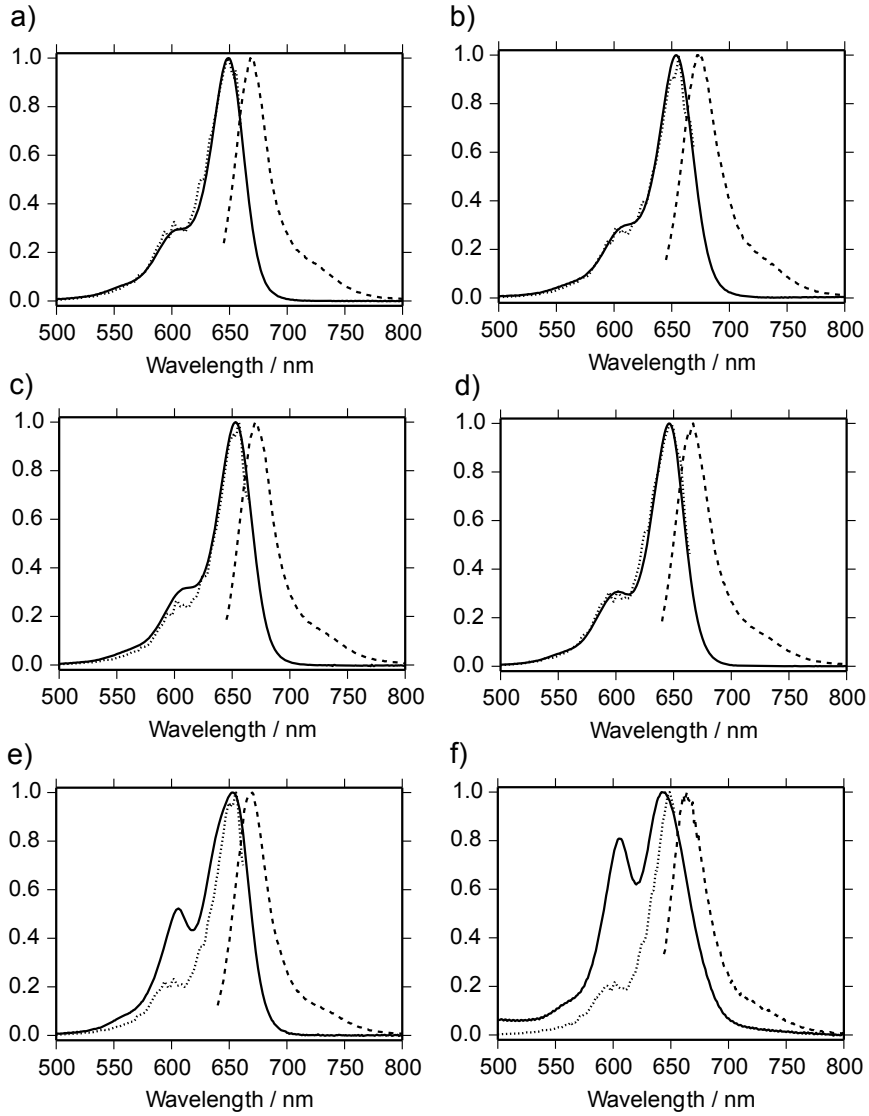

FIGURE C.25: Normalized absorption, fluorescence excitation and fluorescence emission spectra in PBS for exemplary fluorescent markers. Figure S5 of [49]. Solid line: Absorption spectra, dotted line: Fluorescence excitation spectra with detection at the respective maximum of the emission spectra, dashed line: Fluorescence emission spectra with excitation at 640 nm for Alexa647-labelled samples and at 635 nm for Atto647N-labeled samples. a) hydrolyzed Alexa647-NHS-Ester, b) SNAP-tag-Alexa647, c) anti-GFP antibody-Alexa647, d) hydrolyzed Atto647N-NHS-Ester, e) Streptavidin-Atto647N, f) anti-GFP antibody-Atto647N higher DOL.

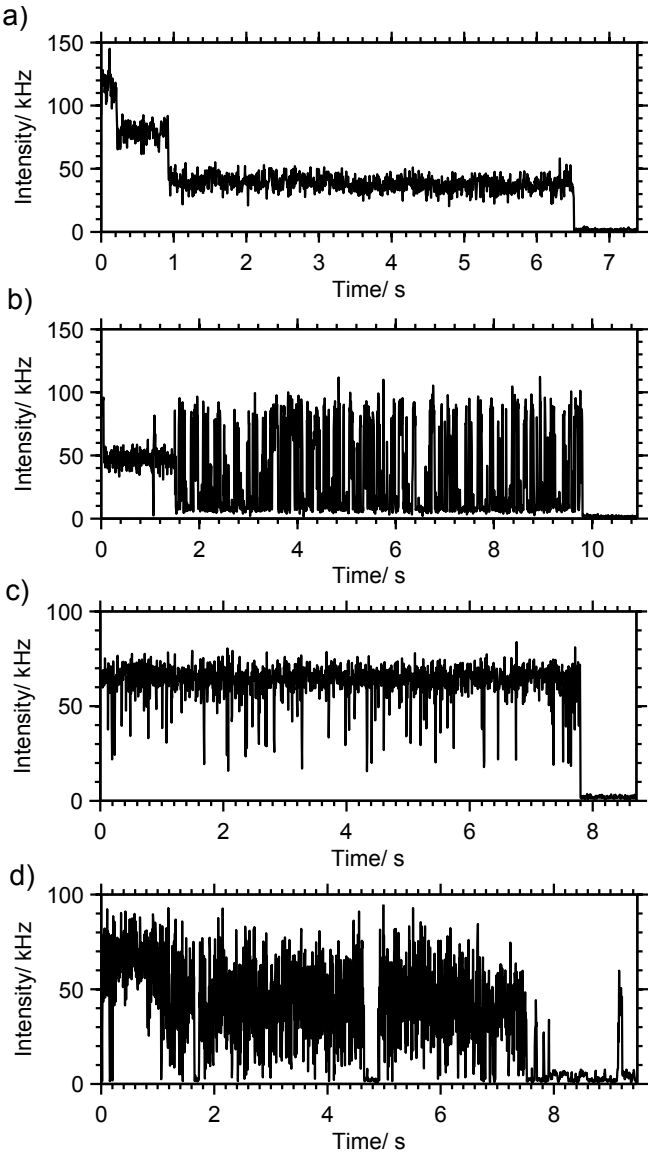

FIGURE C.26: Differences in photophysical behaviour of protein-conjugated Alexa647. Figure S7 of [49]. Excitation laser power 5 µW at 640 nm with a repetition rate of 20 MHz. a) Stable emission with little variations in intensity for anti-GFP antibody-Alexa647, b) Stable emission followed by on/ off blinking for anti-GFP antibody-Alexa647, c) and d) fast on/ off blinking of SNAP-tag-Alexa647.

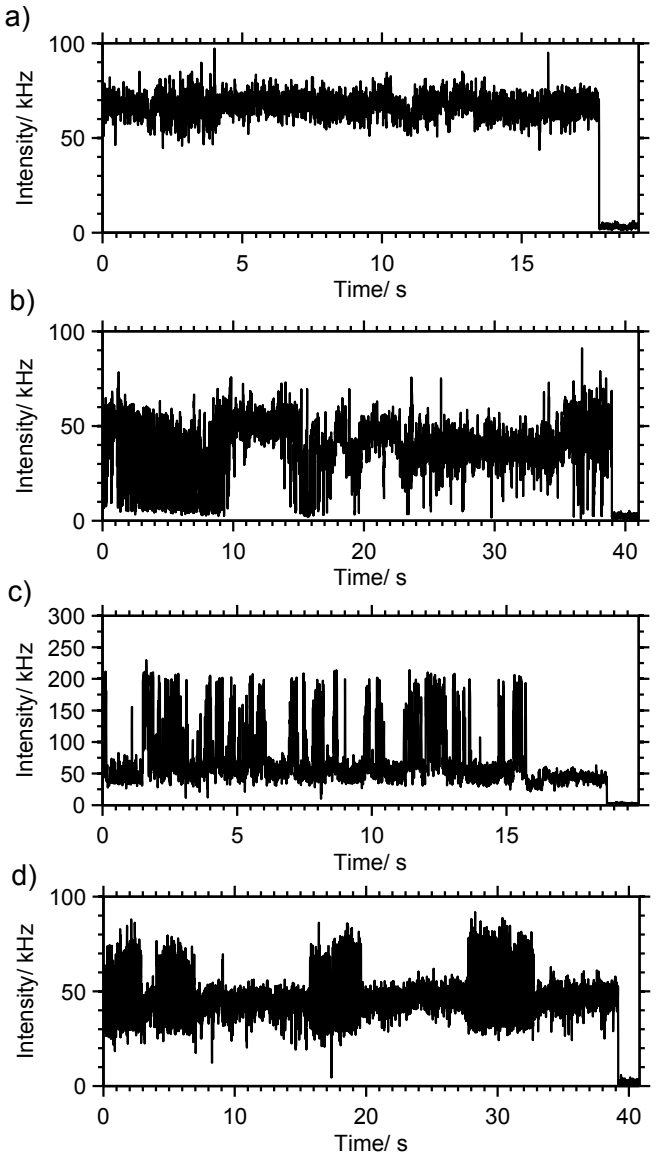

FIGURE C.27: Differences in photophysical behaviour of protein-conjugated Atto647N. Figure S6 of [49]. Excitation laser power 5 µW at 640 nm with a repetition rate of 20 MHz. a) Stable fluorescence emission with occasional fluctuations between the two known states of Atto647N. b), c) and d) On/off blinking and highly fluctuating emission of fluorophores.

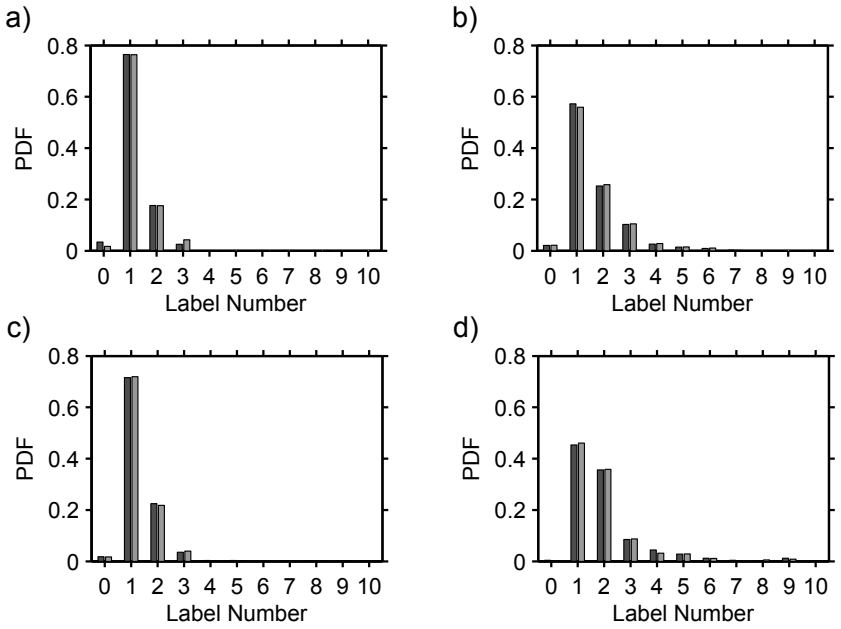

FIGURE C.28: Fluorophore blinking does not significantly influence the label number distribution of Alexa647 labeled marker proteins. Figure S9 of [49]. Normalized label number distributions (PDF) for excitation laser powers of 5 µW at 640 nm with a repetition rate of 20 MHz. Analysis period 2.5 MLC or 125 ms. Dark grey: Non-blinking, light grey: All. a) SNAP-tag, b) anti-GFP antibody, c) anti-GFP nanobody, d) streptavidin.

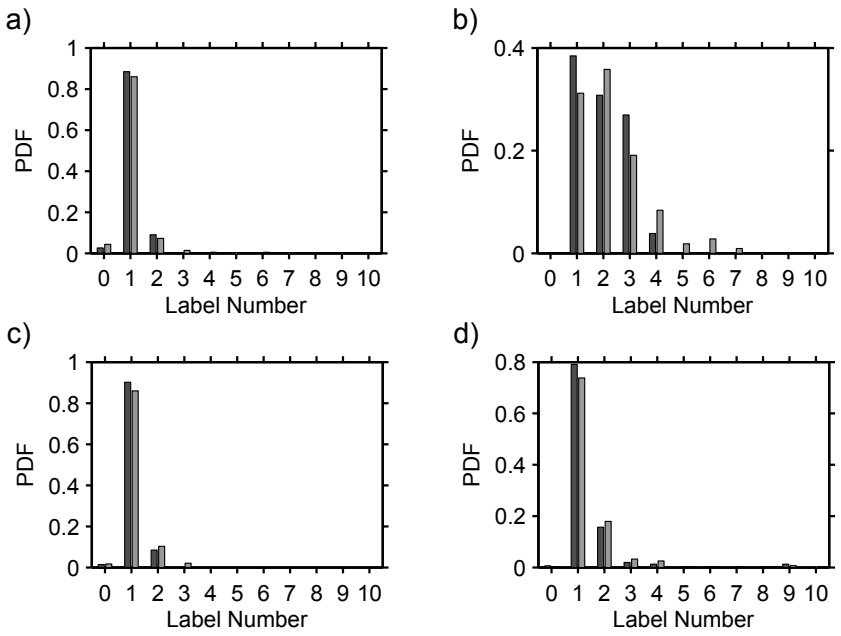

FIGURE C.29: Fluorophore blinking does not significantly influence the label number distribution of Atto647N labeled marker proteins. The only difference occurs for b), because of the low number of histogram entries without blinking. Figure S8 of [49]. Normalized label number distributions (PDF) for excitation laser powers of 5 µW at 640 nm with a repetition rate of 20 MHz. Analysis period 2.5 MLC or 125 ms. Dark grey: Non-blinking, light grey: All. a) SNAP-tag, b) anti-GFP antibody, c) anti-GFP nanobody, d) streptavidin.

TABLE 15: Number averaged molecular weight M_n (see Equation 24) of fractionated Poly(3-hexylthiophene) samples and the respective number of single polymer chains N_{total} measured and analyzed in single molecule experiments. For several molecular weights experiments were conducted with two different prepared cover slips. In addition, the amplitude weighted average photostability time τ_{ph} along with the photostability times $\tau_{ph,1}$ and $\tau_{ph,2}$ from a biexponential fit to the summed PL intensity decay are given.

sample	1	2	3	4	5	6
M_n/ kDa	19	35	55	71	90	110
N_{total}/ #	493	390	238	196	313	365
N_{sample}/ #	228/265	166/224	238	196	143/170	167/198
τ_{ph}/ s	11.5/9.5	30.7/17.2	28.1	36.0	35.3/10.7	12.0/11.8
$\tau_{ph,1}$/ s	0.7/0.7	3.1/3.7	4.7	1.9	1.3/0.9	0.7/1.2
$\tau_{ph,2}$/ s	16.1/13.5	36.3/39.6	42.3	42.6	42.3/15.6	16.9/17.7

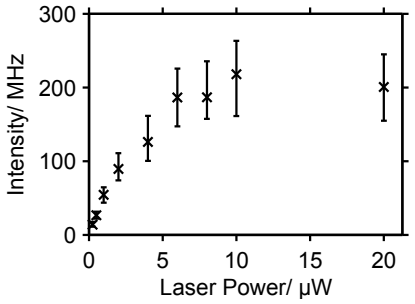

FIGURE D.30: Photoluminescence saturation of fractionated P3HT with a number averaged molecular weight of 90 kDa with increasing laser excitation power. At least three 20 µm × 20 µm fields of view were scanned at 0.5 ms/pixel at 470 nm with a repetition rate of 20 MHz for each excitation condition and the summed PL intensity per polymer chain was extracted using the ALEX software developed in my diploma thesis [214]. The median of the PL intensity is plotted along with the lower and upper quartiles as error bars against the laser excitation power.

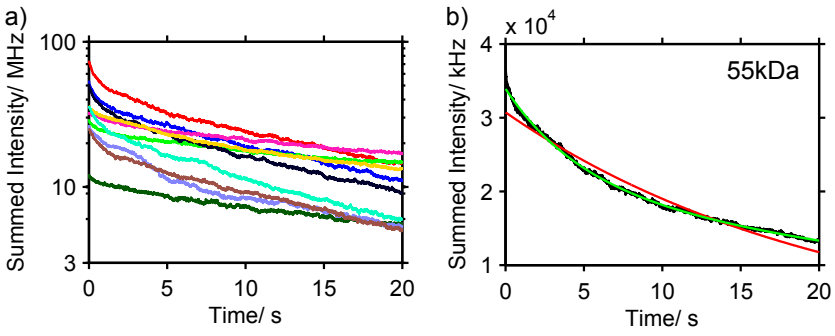

FIGURE D.31: Photostability of P3HT samples of different number average molecular weight. a) Summed photoluminescence (PL) intensity decay of the respective measured single polymer chains embedded in Zeonex. b) Exemplary mono- (red line) and biexponential (green line) decay fit to the summed PL intensity decay (black) of P3HT with number averaged molecular weight of 55 kDa.

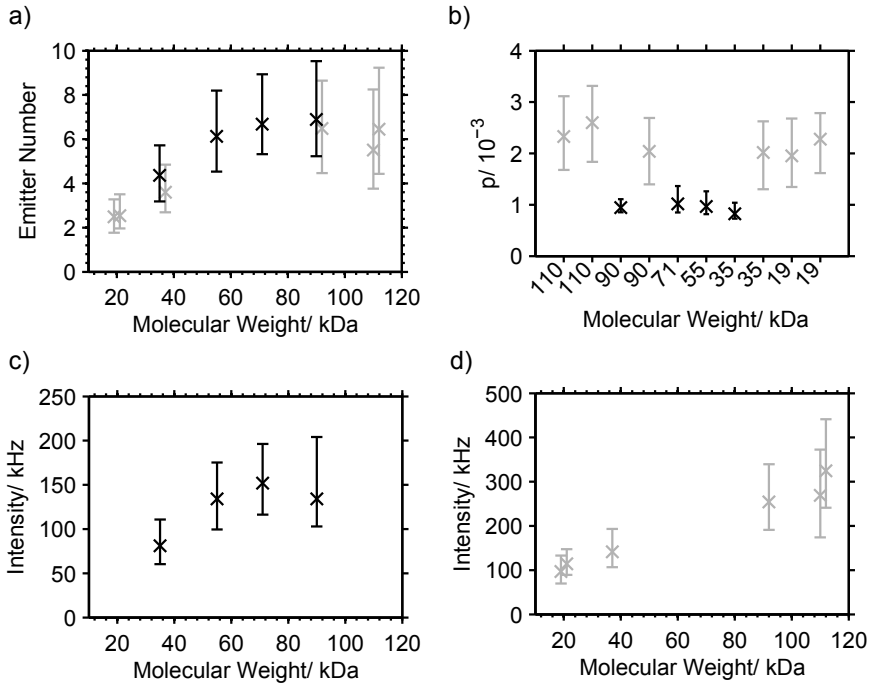

FIGURE D.32: Properties of poly(3-hexylthiophene) (P3HT) of different molecular brightness in dependence of the number average molecular weight. Single P3HT chains embedded in Zeonex were excited at 470 nm with an excitation power of 2 µW and a repetition rate of 20 MHz. The median is displayed along with the lower and upper quartiles as error bars for CoPS estimates with an analysis period of 5 MLC or 250 ms. Bright (light grey) and dim (black) samples are plotted seperately for each experiment. a) Label number estimates. b) Detection probability estimates. c) Intensity for dim samples. d) Intensity for bright samples.

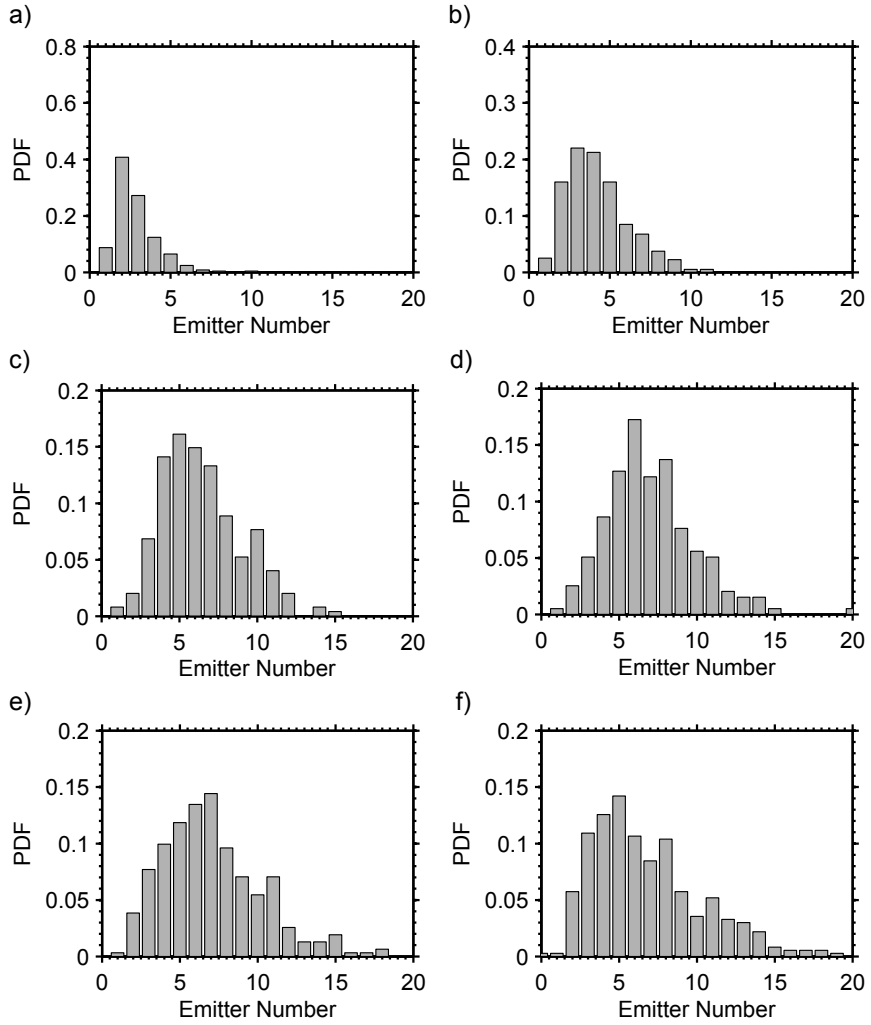

FIGURE D.33: Estimated emitter number distributions of poly(3-hexylthiophene) (P3HT) of different number average molecular weight M_n. Single P3HT chains embedded in Zeonex were excited at 470 nm with an excitation power of 2 µW and a repetition rate of 20 MHz. CoPS analysis period 5 MLC or 250 ms. a) M_n=19 kDa. b) M_n=35 kDa. c) M_n=55 kDa. d) M_n=71 kDa. e) M_n=90 kDa. f) M_n=110 kDa.

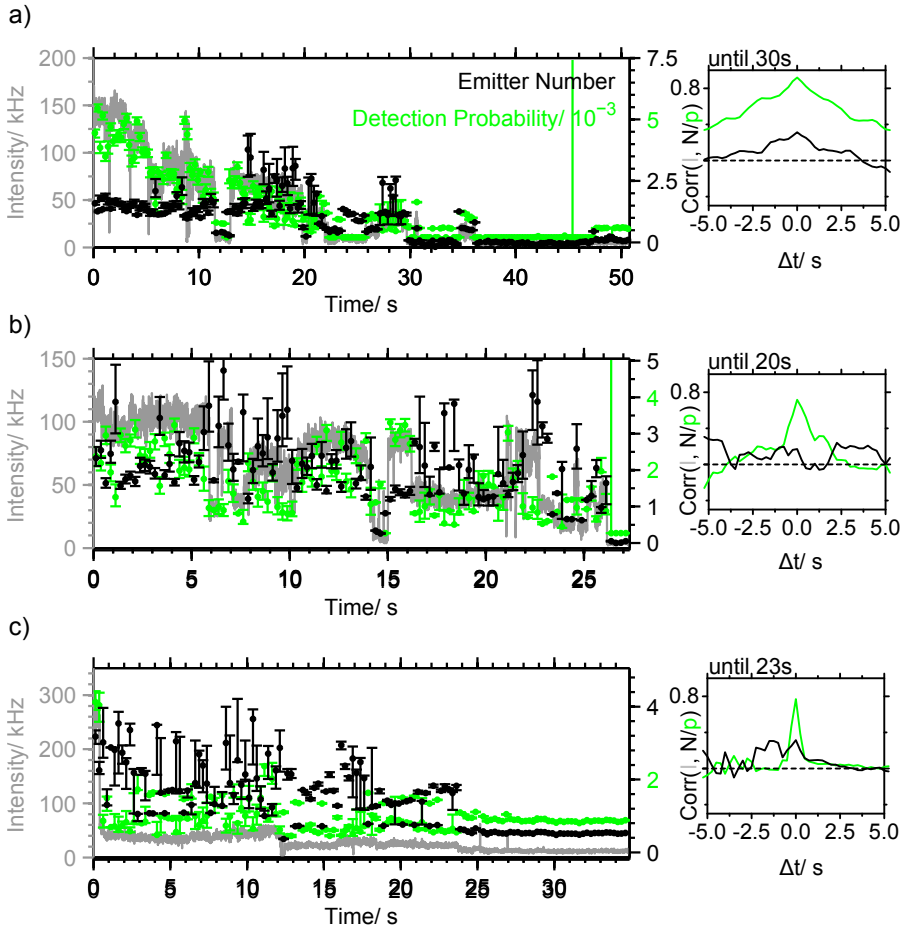

FIGURE D.34: Different dynamical behaviour of photoluminescence in conjugated polymer chains due to quenching. Photoluminescence (PL) intensity traces (grey line) along with emitter number (black) and detection probability estimates (green) for single P3HT chains. The error bars are derived from resampling. On the right the correlation between PL intensity and emitter number (black line) or detection probability estimates (green line). Modification of Figure S2 of [179].

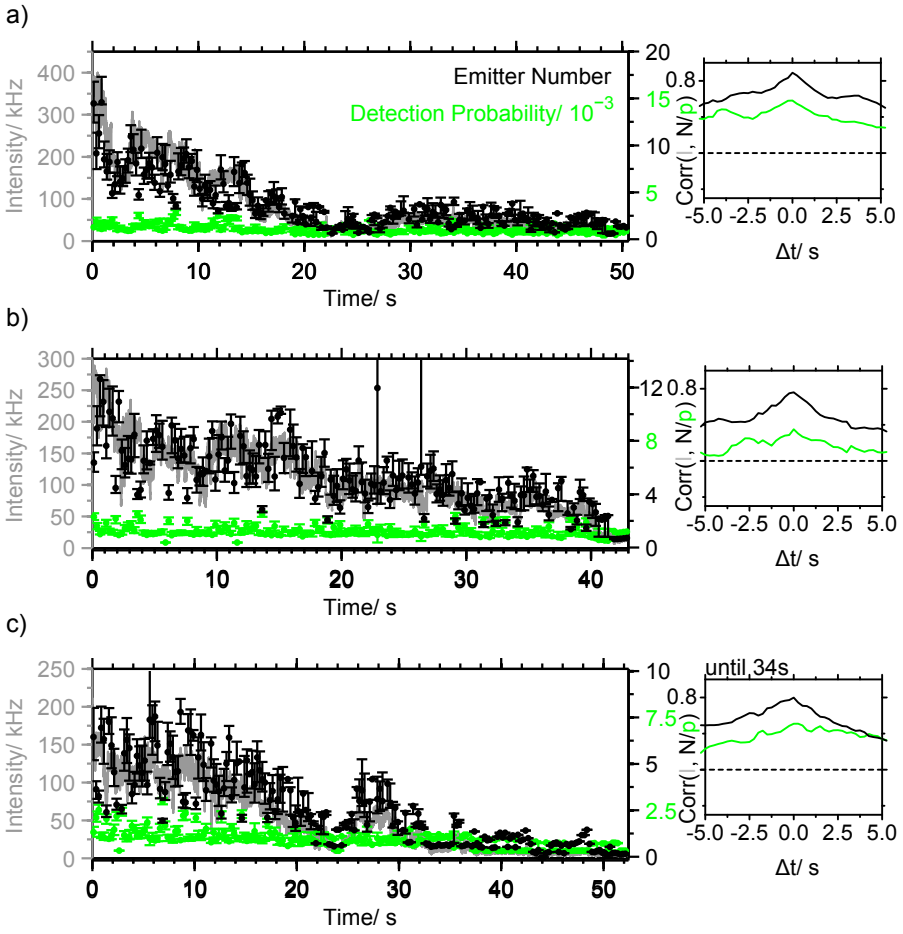

FIGURE D.35: Different dynamical behaviour of photoluminescence in conjugated polymer chains due to quenching. Photoluminescence (PL) intensity traces (grey line) along with emitter number (black) and detection probability estimates (green) for single P3HT chains. The error bars are derived from resampling. On the right the correlation between PL intensity and emitter number (black line) or detection probability estimates (green line). Modification of Figure S2 of [179].

PUBLICATIONS

PEER REVIEWED JOURNAL ARTICLES

1. K. S. Grußmayer, F. Steiner, J. M. Lupton, D.–H. Herten, and J. Vogelsang, Differentiation between shallow and deep trap states on single poly(3-hexylthiophene) chains by photon statistics, *ChemPhysChem* **2015**, Accepted.

2. C. Liesche, K. S. Grußmayer, M. Ludwig, S. Wörz, K. Rohr, D.–H. Herten, J. Beaudouin, and R. Eils, Automated Analysis of Single Molecule Photobleaching Data by Statistical Modeling of Spot Populations. *Biophysical Journal* **2015**, in Review.

3. K. S. Grußmayer, D.–P. Herten, Photon Antibunching in Single Molecule Fluorescence Spectroscopy, in Advanced Photon Counting, (Eds.: P. Kapusta, M. Wahl, R. Erdmann), *Springer International Publishing, Cham*, **Apr. 2015**, pp. 159–190.

4. K. S. Grußmayer, A. Kurz, D.–P. Herten, Single-Molecule Studies on the Label Number Distribution of Fluorescent Markers, *ChemPhysChem* **Feb. 2014**, 15, 734–742.

5. A. Kurz, J. J. Schmied, K. S. Grußmayer, P. Holzmeister, P. Tinnefeld, D.–P. Herten, Counting fluorescent dye molecules on DNA origami by means of photon statistics, *Small* **Dec. 2013**, 9, 4061–4068.

6. A. Rybina, C. Lang, M. Wirtz, K. S. Grußmayer, A. Kurz, F. Maier, et al., Distinguishing Alternative Reaction Pathways by Single-Molecule Fluorescence Spectroscopy, *Angewandte Chemie International Edition* **2013**, 52(24), 6322–6325.

7. K. S. Grußmayer, T. Ehrhard, K. Lymperopoulos, and D.–H. Herten, Precise quantification of transcription factors in a surface-based single-molecule assay, *Biophysical Chemistry* **2013**, 184(C), 1–7

CONFERENCE CONTRIBUTIONS

1. *PicoQuant 21st International Workshop on 'Single Molecule Spectroscopy and Super-resolution Microscopy in the Life Sciences'*, Berlin (Germany) **2015**, oral contribution: 'Counting by Photon Statistics — Fluorescence Quantification based on Photon Antibunching'

2. *Focus on Microscopy 2015*, Göttingen (Germany) **2015**, oral contribution: 'Counting by Photon Statistics — Versatile Fluorescence Quantification based on Photon Antibunching'

3. *PicoQuant 20th International Workshop on 'Single Molecule Spectroscopy and Ultra Sensitive Analysis in the Life Sciences'*, Berlin (Germany) **2014**, poster: 'Counting by Photon Statistics — Versatile Fluorescence Quantification with Photon Antibunching'

4. *Labeling and Nanoscopy*, DKFZ Heidelberg (Germany) **2014**, poster: 'Counting by Photon Statistics — Versatile Fluorescence Quantification with Photon Antibunching'

5. *PicoQuant 19th International Workshop on 'Single Molecule Spectroscopy and Ultra Sensitive Analysis in the Life Sciences'*, Berlin (Germany) **2013**, poster: 'Counting by Photon Statistics — An Investigation of Number and Brightness Distribution for Different Labeling Strategies'

6. *'Seeing is Believing – Imaging the Processes of Life' 2013*, EMBL Heidelberg (Germany) **2013**, poster: 'Counting by Photon Statistics: an Investigation of Number and Brightness Distributions for Different Labeling Strategies'

7. *48th Winterseminar on 'Biophysical Chemistry, Molecular Biology and Cybernetics of Cell Function'*, Klosters (Switzerland) **2013**, poster: 'Counting by Photon Statistics – An Investigation of Number and Brightness Distribution for Different Labeling Strategies'

8. *PicoQuant 18th International Workshop on 'Single Molecule Spectroscopy and Ultra Sensitive Analysis in the Life Sciences'*, Berlin (Germany) **2012**, poster: 'Counting by Photon Statistics – Quantification Beyond the Resolution Limit'

BIBLIOGRAPHY

[1] R. Cowan, *Journal of Child Psychology and Psychiatry and Allied Disciplines* **1981**, *22*, 204–204.

[2] K. Wynn, *Cognitive Psychology* **1992**, *24*, 220–251.

[3] K. C. Fuson, Children's counting and concepts of number, Springer New York, **1988**.

[4] V. Slaughter, S. Itakura, A. Kutsuki, M. Siegal, *Proceedings of the Royal Society B* **Oct. 2011**, *278*, 2979–2984.

[5] J. M. Matthews, M. Sunde in *Protein Dimerization and Oligomerization in Biology*, (Ed.: J. M. Matthews), Springer, **2012**, pp. 1–18.

[6] F. K.-M. Chan, H. J. Chun, L. Zheng, R. M. Siegel, K. L. Bui, M. J. Lenardo, *Science* **June 2000**, *288*, 2351–2354.

[7] L. Clancy, K. Mruk, K. Archer, M. Woelfel, J. Mongkolsapaya, G. Screaton, M. J. Lenardo, F. Chan, *Proceedings of the National Academy of Sciences of the United States of America* **2005**, *102*, 18099–18104.

[8] T. A. Wassenaar, W. J. Quax, A. E. Mark, *Proteins: Structure Function and Bioinformatics* **Aug. 2007**, *70*, 333–343.

[9] J. Pawley, *Handbook of Biological Confocal Microscopy*, Springer London, Limited, **1995**.

[10] D. Axelrod, T. P. Burghardt, N. L. Thompson, *Annual Review of Biophysics and Bioengineering* **1984**, *13*, 247–268.

[11] P. Kapusta, M. Wahl, R. Erdmann, *Advanced Photon Counting*, Springer.

[12] Z. Liu, L. D. Lavis, E. Betzig, *Molecular Cell* **May 2015**, *58*, 644–659.

[13] S. W. Hell, *Science* **May 2007**, *316*, 1153–1158.

[14] A. R. Small, R. Parthasarathy, *Annual Review of Physical Chemistry* **2014**, *65*, 107–125.

[15] T. J. Gould, S. T. Hess, J. Bewersdorf, *Annual Review of Biomedical Engineering* **2012**, *14*, 231–254.

[16] T. Müller, C. Schumann, A. Kraegeloh, *ChemPhysChem* **June 2012**, *13*, 1986–2000.

[17] B. N. Giepmans, S. R. Adams, M. H. Ellisman, R. Y. Tsien, *Science Signaling* **2006**, *312*, 217–224.

[18] A. Kapanidis, S. Weiss, *The Journal of Chemical Physics* **2002**, *117*, 10953–10964.

[19] W. Demtröder, *Experimentalphysik 3: Atome, Moleküle und Festkörper*, *Vol. 4*, Springer Verlag, **2010**.

[20] J. Lakowicz, *Principles of fluorescence spectroscopy*, *Vol. 1*, 3rd edition, Springer Science+Business Media, **2006**.

[21] J. Vogelsang, R. Kasper, C. Steinhauer, B. Person, M. Heilemann, M. Sauer, P. Tinnefeld, *Angewandte Chemie International Edition* **2008**, *47*, 5465–5469.

[22] N. Johnsson, K. Johnsson, *ACS Chemical Biology* **2007**, *2*, 31–38.

[23] R. Wombacher, V. W. Cornish, *Journal of Biophotonics* **2011**, *4*, 391–402.

[24] M. Boyce, C. R. Bertozzi, *Nature Methods* **Aug. 2011**, *8*, 638–642.

[25] C. Szent-Gyorgyi, B. A. Schmidt, Y. Creeger, G. W. Fisher, K. L. Zakel, S. Adler, J. A. J. Fitzpatrick, C. A. Woolford, Q. Yan, K. V. Vasilev, P. B. Berget, M. P. Bruchez, J. W. Jarvik, A. Waggoner, *Nature Biotechnology* **Dec. 2007**, *26*, 235–240.

[26] A. Juillerat, T. Gronemeyer, A. Keppler, S. Gendreizig, H. Pick, H. Vogel, K. Johnsson, *Chemistry & Biology* **Apr. 2003**, *10*, 313–317.

[27] A. Keppler, S. Gendreizig, T. Gronemeyer, H. Pick, H. Vogel, K. Johnsson, *Nature Biotechnology* **Dec. 2002**, *21*, 86–89.

[28] G. V. Los, L. P. Encell, M. G. McDougall, D. D. Hartzell, N. Karassina, C. Zimprich, M. G. Wood, R. Learish, R. F. Ohana, M. Urh, D. Simpson, J. Mendez, K. Zimmerman, P. Otto, G. Vidugiris, J. Zhu, A. Darzins, D. H. Klaubert, R. F. Bulleit, K. V. Wood, *ACS Chemical Biology* **June 2008**, *3*, 373–382.

[29] E. A. Greenfield, *Antibodies: A Laboratory Manual*, Cold Spring Harbor Laboratory Press, **2013**.

[30] J. Ries, C. Kaplan, E. Platonova, H. Eghlidi, H. Ewers, *Nature Methods* **Apr. 2012**, *9*, 582–584.

[31] P. C. Fridy, Y. Li, S. Keegan, M. K. Thompson, I. Nudelman, J. F. Scheid, M. Oeffinger, M. C. Nussenzweig, D. Fenyö, B. T. Chait, M. P. Rout, *Nature Methods* **Dec. 2014**, *11*, 1253–1260.

[32] M. R. Green, J. Sambrook, *Molecular Cloning: A Laboratory Manual*, Cold Spring Harbor Laboratory Press, **2012**.

[33] R. C. Wilson, J. A. Doudna, *Annual Review of Biophysics* **2013**, *42*, 217–239.

[34] L. Cong, F. A. Ran, D. Cox, S. Lin, R. Barretto, N. Habib, P. D. Hsu, X. Wu, W. Jiang, L. A. Marraffini, F. Zhang, *Science* **Feb. 2013**, *339*, 819–823.

[35] N. Ehmann, S. van de Linde, A. Alon, D. Ljaschenko, X. Z. Keung, T. Holm, A. Rings, A. DiAntonio, S. Hallermann, U. Ashery, M. Heckmann, M. Sauer, R. J. Kittel, *Nature Communications* **2014**, *5*.

[36] M. Sauer, *Journal of Cell Science* **Aug. 2013**, *126*, 3505–3513.

[37] N. Durisic, L. L. Cuervo, M. Lakadamyali, *Current Opinion in Chemical Biology* **June 2014**, *20*, 22–28.

[38] D. L. Meadows, J. S. Shafer, J. S. Schultz, *Journal of Immunological Methods* **1991**, *143*, 263–272.

[39] R. P. Haugland in *Current Protocols in Cell Biology*, Wiley Online Library, **Nov. 2003**, pp. 1–22.

[40] H. J. Gruber, C. D. Hahn, G. Kada, C. K. Riener, G. S. Harms, W. Ahrer, T. G. Dax, H.-G. Knaus, *Bioconjugate Chemistry* **Sept. 2000**, *11*, 696–704.

[41] G. P. Anderson, N. L. Nerurkar, *Journal of Immunological Methods* **Nov. 2002**, *271*, 17–24.

[42] J. E. Berlier, A. Rothe, G. Buller, J. Bradford, D. R. Gray, B. J. Filanoski, W. G. Telford, S. Yue, J. Liu, C. Y. Cheung, W. Chang, J. D. Hirsch, J. M. Beechem Rosaria P Haugland, R. Haugland, *Journal of Histochemistry & Cytochemistry* **Dec. 2003**, *51*, 1699–1712.

[43] T. Feltkamp, *Immunology* **1970**, *18*, 865–873.

[44] M. Brinkley, *Bioconjugate Chemistry* **1992**, *3*, 2–13.

[45] S. Vira, E. Mekhedov, G. Humphrey, P. S. Blank, *Analytical Biochemistry* **July 2010**, *402*, 146–150.

[46] N. Durisic, L. Laparra-Cuervo, A. n. S.-&. lvarez, J. S. Borbely, M. Lakadamyali, *Nature Methods* **Jan. 2014**, *11*, 156–162.

[47] D. Casanova, D. Giaume, M. Moreau, J.-L. Martin, T. Gacoin, J.-P. Boilot, A. Alexandrou, *Journal of the American Chemical Society* **Oct. 2007**, *129*, 12592–12593.

[48] T. Pons, I. L. Medintz, X. Wang, D. S. English, H. Mattoussi, *Journal of the American Chemical Society* **Nov. 2006**, *128*, 15324–15331.

[49] K. S. Grußmayer, A. Kurz, D.-P. Herten, *ChemPhysChem* **Feb. 2014**, *15*, 734–742.

[50] R. H. Friend, R. W. Gymer, A. B. Holmes, J. H. Burroughes, *Nature* **1999**, *397*, 121–128.

[51] J. M. Lupton, *Advanced Materials* **Apr. 2010**, *22*, 1689–1721.

[52] G. Strobl in *The physics of polymers*, Springer Berlin Heidelberg, Berlin, Heidelberg, **1997**.

[53] F. Steiner, J. Vogelsang, J. M. Lupton, *Physical Review Letters* **Apr. 2014**, *112*, 137402–137405.

[54] J. M. Lupton, *ChemPhysChem* **Dec. 2011**, *13*, 901–907.

[55] T.-Q. Nguyen, V. Doan, B. J. Schwartz, *Journal of Chemical Physics* **1999**, *110*, 4068–4078.

[56] D. Hu, J. Yu, K. Wong, B. Bagchi, P. J. Rossky, P. F. Barbara, *Nature* **2000**, *405*, 1030–1033.

[57] S. Sarzi Sartori, S. De Feyter, J. Hofkens, M. Van der Auweraer, F. De Schryver, K. Brunner, J. W. Hofstraat, *Macromolecules* **2003**, *36*, 500–507.

[58] T. Huser, M. Yan, *Journal of Photochemistry and Photobiology A: Chemistry* **2001**, *144*, 43–51.

[59] T. Huser, M. Yan, L. J. Rothberg, *Proceedings of the National Academy of Sciences of the United States of America* **Oct. 2000**, *97*, 11187–11191.

[60] Y. Ebihara, M. Vacha, *Journal of Physical Chemistry B* **Oct. 2008**, *112*, 12575–12578.

[61] A. Mehta, P. Kumar, M. D. Dadmun, J. Zheng, R. M. Dickson, T. Thundat, B. G. Sumpter, M. D. Barnes, *Nano Letters* **May 2003**, *3*, 603–607.

[62] C. W. Hollars, S. M. Lane, T. Huser, *Chemical Physics Letters* **Mar. 2003**, *370*, 393–398.

[63] P. Kumar, T.-H. Lee, A. Mehta, B. G. Sumpter, R. M. Dickson, M. D. Barnes, *Journal of the American Chemical Society* **Mar. 2004**, *126*, 3376–3377.

[64] S. Fore, T. Huser, T. A. Laurence, C. W. Hollars, *IEEE Journal of Selected Topics in Quantum Electronics* **2007**, *13*, 996–1005.

[65] A. Thiessen, J. Vogelsang, T. Adachi, F. Steiner, D. Vanden Bout, J. M. Lupton, *Proceedings of the National Academy of Sciences* **Sept. 2013**, *110*, E3550–E3556.

[66] H. Sirringhaus, P. J. Brown, R. H. Friend, M. M. Nielsen, *Nature* **1999**, *401*, 685–688.

[67] J. S. Verdaasdonk, J. Lawrimore, K. Bloom, *Methods in Cell Biology* **2014**, *123*, 347–365.

[68] J. J. Schmied, A. Gietl, P. Holzmeister, C. Forthmann, C. Steinhauer, T. Dammeyer, P. Tinnefeld, *Nature Methods* **Dec. 2012**, *9*, 1133–1134.

[69] U. Resch-Genger, M. Grabolle, S. Cavaliere-Jaricot, R. Nitschke, T. Nann, *Nature Methods* **Aug. 2008**, *5*, 763–775.

[70] D. Magde, R. Wong, P. G. Seybold, *Photochemistry and Photobiology* **Apr. 2002**, *75*, 327–334.

[71] T. Schmidt, G. Schütz, H. Gruber, H. Schindler, *Analytical Chemistry* **1996**, *68*, 4397–4401.

[72] Y. Sako, S. Minoghchi, T. Yanagida, *Nature Cell Biology* **2000**, *2*, 168–172.

[73] J. Madl, J. Weghuber, R. Fritsch, I. Derler, M. Fahrner, I. Frischauf, B. Lackner, C. Romanin, G. Schütz, *Journal of Biological Chemistry* **Dec. 2010**, *285*, 41135–41142.

[74] R. Reyes-Lamothe, D. J. Sherratt, M. C. Leake, *Science* **2010**, *328*, 498–501.

[75] J. Lawrimore, K. S. Bloom, E. Salmon, *The Journal of Cell Biology* **Nov. 2011**, *195*, 573–582.

[76] V. C. Coffman, J.-Q. Wu, *Trends in Biochemical Sciences* **Nov. 2012**, *37*, 499–506.

[77] M. H. Ulbrich, E. Y. Isacoff, *Nature Methods* **Mar. 2007**, *4*, 319–321.

[78] M. H. Ulbrich in *Far-Field Optical Nanoscopy*, Springer Berlin Heidelberg, Berlin, Heidelberg, **Jan. 2012**, pp. 263–291.

[79] R. J. Arant, M. H. Ulbrich, *ChemPhysChem* **Jan. 2014**, *15*, 600–605.

[80] S. K. Das, M. Darshi, S. Cheley, M. I. Wallace, H. Bayley, *ChemBioChem* **June 2007**, *8*, 994–999.

[81] M. Rust, M. Bates, X. Zhuang, *Nature Methods* **2006**, *3*, 793–796.

[82] E. Betzig, G. Patterson, R. Sougrat, O. Lindwasser, S. Olenych, J. Bonifacino, M. Davidson, J. Lippincott-Schwartz, H. Hess, *Science* **2006**, *313*, 1642–1645.

[83] S. T. Hess, T. P. K. Girirajan, M. D. Mason, *Biophysical Journal* **Dec. 2006**, *91*, 4258–4272.

[84] G. Patterson, M. Davidson, S. Manley, J. Lippincott-Schwartz, *Annual Review of Physical Chemistry* **Mar. 2010**, *61*, 345–367.

[85] P. Annibale, S. Vanni, M. Scarselli, U. Rothlisberger, A. Radenovic, *PloS one* **July 2011**, *6*, 1–8.

[86] S.-H. Lee, J. Y. Shin, A. Lee, C. Bustamante, *Proceedings of the National Academy of Sciences* **Oct. 2012**, *109*, 17436–17441.

[87] S. L. Veatch, B. B. Machta, S. A. Shelby, E. N. Chiang, D. A. Holowka, B. A. Baird, *PloS one* **Feb. 2012**, *7*, 1–13.

[88] P. Sengupta, T. Jovanovic-Talisman, D. Skoko, M. Renz, S. L. Veatch, J. Lippincott-Schwartz, *Nature Methods* **Sept. 2011**, *8*, 969–975.

[89] R. P. J. Nieuwenhuizen, K. A. Lidke, M. Bates, D. L. Puig, D. Grünwald, S. Stallinga, B. Rieger, *Nature Methods* **Apr. 2013**, *10*, 557–562.

[90] J. Gunzenhäuser, N. Olivier, T. Pengo, S. Manley, *Nano Letters* **Sept. 2012**, *12*, 4705–4710.

[91] Y. Li, Y. Ishitsuka, P. N. Hedde, G. U. Nienhaus, *ACS Nano* **June 2013**, *7*, 5207–5214.

[92] V. Raicu, D. R. Singh, *Biophysical Journal* **Nov. 2013**, *105*, 1937–1945.

[93] L. W. Runnels, S. F. Scarlata, *Biophysical Journal* **Oct. 1995**, *69*, 1569–1583.

[94] A. N. Bader, S. Hoetzl, E. G. Hofman, J. Voortman, P. M. P. van Bergen en Henegouwen, G. van Meer, H. C. Gerritsen, *ChemPhysChem* **Dec. 2010**, *12*, 475–483.

[95] P. Kask, K. Palo, D. Ullmann, K. Gall, *Proceedings of the National Academy of Sciences of the United States of America* **1999**, *96*, 13756–13761.

[96] Y. Chen, J. D. Müller, P. T. So, E. Gratton, *Biophysical Journal* **1999**, *77*, 553–567.

[97] R. B. Dalal, M. A. Digman, A. F. Horwitz, V. Vetri, E. Gratton, *Microscopy Research and Technique* **2007**, *71*, 69–81.

[98] K. S. Grußmayer, D.-P. Herten in *Advanced Photon Counting*, (Eds.: P. Kapusta, M. Wahl, R. Erdmann), Springer International Publishing, Cham, **Apr. 2015**, pp. 159–190.

[99] R. H. Brown, R. Q. Twiss, *Nature* **1956**, *177*, 27–29.

[100] M. Fox, *Quantum Optics: An Introduction*, Oxford University Press, Oxford, **2006**.

[101] H. Kimble, L. Mandel, *Physical Review A* **June 1976**, *13*, 2123–2144.

[102] H. J. Carmichael, D. F. Walls, *Journal of Physics B: Atomic and Molecular Physics* **1976**, *9*, 1199–1219.

[103] H. J. Kimble, M. Dagenais, L. Mandel, *Physical Review Letters* **1977**, *39*, 691–695.

[104] T. Basché, W. Moerner, M. Orrit, H. Talon, *Physical Review Letters* **1992**, *69*, 1516–1519.

[105] P. Michler, A. Kiraz, C. Becher, W. V. Schoenfeld, P. M. Petroff, L. Zhang, E. Hu, A. Imamoglu, *Science* **Dec. 2000**, *290*, 2282–2285.

[106] P. Michler, A. Imamoglu, M. D. Mason, P. J. Carson, G. F. Strouse, S. K. Buratto, *Nature* **2000**, *406*, 968–970.

[107] B. Lounis, H. A. Bechtel, D. Gerion, P. Alivisatos, W. E. Moerner, *Chemical Physics Letters* **2000**, *329*, 399–404.

[108] B. Lounis, W. E. Moerner, *Nature* **Sept. 2000**, *407*, 491–493.

[109] G. Messin, J. P. Hermier, E. Giacobino, P. Desbiolles, M. Dahan, *Optics Letters* **2001**, *26*, 1891–1893.

[110] R. Brouri, A. Beveratos, J.-P. Poizat, P. Grangier, *Optics Letters* **2000**, *25*, 1294–1296.

[111] C. Kurtsiefer, S. Mayer, P. Zarda, H. Weinfurter, *Physical Review Letters* **2000**, *85*, 290–293.

[112] M. Nothaft, S. Höhla, F. Jelezko, N. Frühauf, J. Pflaum, J. Wrachtrup, *Nature Communications* **1**, *3*, 1–6.

[113] L. H. G. Tizei, M. Kociak, *arXiv* **Jan. 2013**, arXiv: `1301.0922v1 [cond-mat.mes-hall]`.

[114] T. M. Babinec, B. J. M. Hausmann, M. Khan, Y. Zhang, J. R. Maze, P. R. Hemmer, M. Loncar, *Nature Nanotechnology* **Mar. 2010**, *5*, 195–199.

[115] J. Claudon, J. Bleuse, N. S. Malik, M. Bazin, P. Jaffrennou, N. Gregersen, C. Sauvan, P. Lalanne, J.-M. Gerard, *Nature Photonics* **Mar. 2010**, *4*, 174–177.

[116] N. Mizuochi, T. Makino, H. Kato, D. Takeuchi, M. Ogura, H. Okushi, M. Nothaft, P. Neumann, A. Gali, F. Jelezko, J. Wrachtrup, S. Yamasaki, *Nature Photonics* **May 2012**, *6*, 299–303.

[117] J. G. Rarity, P. C. M. Owens, P. R. Tapster, *Journal of Modern Optics* **Dec. 1994**, *41*, 2435–2444.

[118] R. P. Feynman, *International Journal of Theoretical Physics* **1982**, *21*, 467–488.

[119] M. Nielsen, I. Chuang, *Quantum Computation and Quantum Information*, Cambridge University Press, **Jan. 2004**.

[120] A. Beveratos, R. Brouri, T. Gacoin, A. Villing, J.-P. Poizat, P. Grangier, *Physical Review Letters* **Oct. 2002**, *89*, 1–4.

[121] E. Waks, K. Inoue, C. Santori, D. Fattal, J. Vuckovic, G. S. Solomon, Y. Yamamoto, *Nature* **2002**, *420*, 762–762.

[122] V. Giovannetti, S. Lloyd, L. Maccone, *Nature Photonics* **Apr. 2011**, *5*, 222–229.

[123] W. Patrick Ambrose, P. Goodwin, J. Enderlein, D. Semin, J. Martin, R. Keller, *Chemical Physics Letters* **1997**, *269*, 365–370.

[124] P. Kask, P. Piksarv, Ü. Mets, *European Biophysics Journal* **1985**, *12*, 163–166.

[125] Ü. Mets, J. Widengren, R. Rigler, *Chemical Physics* **1997**, *218*, 191–198.

[126] L. Fleury, J. Segura, G. Zumofen, B. Hecht, U. Wild, *Physical Review Letters* **Feb. 2000**, *84*, 1148–1151.

[127] F. Treussart, A. Clouqueur, C. Grossman, J.-F. Roch, *Optics Letters* **2001**, *26*, 1504–1506.

[128] J. Sýkora, K. Kaiser, I. Gregor, W. Bönigk, G. Schmalzing, J. Enderlein, *Analytical Chemistry* **June 2007**, *79*, 4040–4049.

[129] S. C. Kitson, P. Jonsson, J. G. Rarity, P. R. Tapster, *Physical Review A* **1998**, *58*, 620.

[130] Y. Y. Hui, Y.-R. Chang, T.-S. Lim, H.-Y. Lee, W. Fann, H.-C. Chang, *Applied Physics Letters* **2009**, *94*, 1–4.

[131] M. Wu, P. M. Goodwin, W. P. Ambrose, R. A. Keller, *The Journal of Physical Chemistry* **1996**, *100*, 17406–17409.

[132] P. Tinnefeld, C. Müller, M. Sauer, *Chemical Physics Letters* **Aug. 2001**, *345*, 252–258.

[133] K. D. Weston, M. Dyck, P. Tinnefeld, C. Müller, D. P. Herten, M. Sauer, *Analytical Chemistry* **Oct. 2002**, *74*, 5342–5349.

[134] T. Heinlein in Imaging, Manipulation, and Analysis of Biomolecules and Cells: Fundamentals and Applications III, SPIE, pp. 141–148.

[135] S. Fore, T. A. Laurence, Y. Yeh, R. Balhorn, C. W. Hollars, M. Cosman, T. Huser, *IEEE Journal of Selected Topics in Quantum Electronics* **2005**, *11*, 873–880.

[136] S. Ly, J. Petrlova, T. Huser, S. Fore, T. Gao, J. Voss, T. A. Laurence, *Biophysical Journal* **Aug. 2011**, *101*, 970–975.

[137] G. Sánchez-Mosteiro, M. Koopman, E. M. H. P. van Dijk, J. Hernando, N. F. van Hulst, M. García-Parajó, *ChemPhysChem* **Nov. 2004**, *5*, 1782–1785.

[138] P. Tinnefeld, K. D. Weston, T. Vosch, M. Cotlet, T. Weil, J. Hofkens, K. Müllen, F. C. De Schryver, M. Sauer, *Journal of the American Chemical Society* **Dec. 2002**, *124*, 14310–14311.

[139] P. Tinnefeld, J. Hofkens, D.-P. Herten, S. Masuo, T. Vosch, M. Cotlet, S. Habuchi, K. M llen, F. C. De Schryver, M. Sauer, *ChemPhysChem* **Nov. 2004**, *5*, 1786–1790.

[140] C. Hübner, G. Zumofen, A. Renn, A. Herrmann, K. Müllen, T. Basché, *Physical Review Letters* **Aug. 2003**, *91*, 1–4.

[141] A. J. Berglund, A. C. Doherty, H. Mabuchi, *Physical Review Letters* **July 2002**, *89*, 1–4.

[142] T. Vosch, M. Cotlet, J. Hofkens, K. Van Der Biest, M. Lor, K. Weston, P. Tinnefeld, M. Sauer, L. Latterini, K. Müllen, F. C. De Schryver, *J. Phys. Chem. A* **Sept. 2003**, *107*, 6920–6931.

[143] B. Fückel, G. Hinze, F. Nolde, K. Müllen, T. Basché, *J. Phys. Chem. A* **July 2010**, *114*, 7671–7676.

[144] J. Hofkens, M. Cotlet, T. Vosch, P. Tinnefeld, K. D. Weston, C. Ego, A. Grimsdale, K. Müllen, D. Beljonne, J. L. Brédas, S. Jordens, G. Schweitzer, M. Sauer, F. De Schryver, *Proceedings of the National Academy of Sciences of the United States of America* **Nov. 2003**, *100*, 13146–13151.

[145] H. Ta, J. Wolfrum, D.-P. Herten, *Laser Physics* **July 2009**, *20*, 119–124.

[146] H. Ta, A. Kiel, M. Wahl, D.-P. Herten, *Physical Chemistry Chemical Physics* **2010**, *12*, 10295–10300.

[147] H. Ta, PhD thesis, Naturwissenschaftlich-Mathematischen Gesamtfakultät der Ruprecht-Karls-Universität Heidelberg, **Feb. 2010**.

[148] A. Kurz, J. J. Schmied, K. S. Grußmayer, P. Holzmeister, P. Tinnefeld, D.-P. Herten, *Small* **Dec. 2013**, *9*, 4061–4068.

[149] W. H. Press, S. A. Teukolsky, W. T. Vetterling, B. P. Flannery, *Numerical Recipes 3rd Edition: The Art of Scientific Computing*, 3rd ed., Cambridge University Press, **Sept. 2007**.

[150] B. Efron, *The Annals of Statistics* **1979**.

[151] D. N. Politis, J. P. Romano, *The Annals of Statistics* **1994**, *22*, 2031–2050.

[152] J. Enderlein, *Chemical Physics Letters* **July 2005**, *410*, 452–456.

[153] W. E. Moerner, D. P. Fromm, *Review of Scientific Instruments* **2003**, *74*, 3597–3524.

[154] V. Marx, *Nature Methods* **Mar. 2015**, *12*, 187–190.

[155] H. C. Kolb, M. G. Finn, K. B. Sharpless, *Angewandte Chemie International Edition* **2001**, *40*, 2004–2021.

[156] A. Kurz, PhD thesis, Naturwissenschaftlich-Mathematischen Gesamtfakultät der Ruprecht-Karls-Universität Heidelberg, **Jan. 2013**.

[157] T. Cordes, J. Vogelsang, C. Steinhauer, I. H. Stein, C. Forthmann, A. Gietl, J. J. Schmied, G. P. Acuna, S. Laurien, B. Lalkens, P. Tinnefeld in *Far-Field Optical Nanoscopy*, Springer Berlin Heidelberg, Berlin, Heidelberg, **2015**.

[158] G. Lukinavičius, K. Umezawa, N. Olivier, A. Honigmann, G. Yang, T. Plass, V. Mueller, L. Reymond, I. R. Corrêa Jr, Z.-G. Luo, C. Schultz, E. A. Lemke, P. Heppenstall, C. Eggeling, S. Manley, K. Johnsson, *Nature Chemistry* **Jan. 2013**, *5*, 132–139.

[159] G. Lukinavičius, L. Reymond, E. D'Este, A. Masharina, F. Göttfert, H. Ta, A. Güther, M. Fournier, S. Rizzo, H. Waldmann, C. Blaukopf, C. Sommer, D. W. Gerlich, H.-D. Arndt, S. W. Hell, K. Johnsson, *Nature Methods* **July 2014**, *11*, 731–733.

[160] A. Schöffler, Einfluss verschiedener Puffersysteme auf die Photostabilität grün fluoreszierender Farbstoffe, tech. rep., Physikalisch-Chemisches Institut der Ruprecht-Karls-Universität Heidelberg, **Dec. 2013**.

[161] C. E. Aitken, R. A. Marshall, J. D. Puglisi, *Biophysical Journal* **Mar. 2008**, *94*, 1826–1835.

[162] M. Swoboda, J. Henig, H.-M. Cheng, D. Brugger, D. Haltrich, N. Plumeré, M. Schlierf, *ACS Nano* **July 2012**, *6*, 6364–6369.

[163] PerkinElmer Inc., Single Photon Counting Module SPCM-AQR Series Datasheet, **2001**.

[164] A. Le Gall, D. Dulin, G. Clavier, R. Méallet-Renault, P. Bouyer, K. Perronet, N. Westbrook, *ChemPhysChem* **May 2011**, *12*, 1657–1660.

[165] M. Haan, Influence of different buffer systems on the photostability of blue fluorescing dyes, tech. rep., Physikalisch-Chemisches Institut der Ruprecht-Karls-Universität Heidelberg, **June 2014**.

[166] B. Hinkeldey, A. Schmitt, G. Jung, *ChemPhysChem* **Oct. 2008**, *9*, 2019–2027.

[167] C. Eggeling, J. Widengren, R. Rigler, C. Seidel, *Analytical Chemistry* **1998**, *70*, 2651–2659.

[168] C. Eggeling, A. Volkmer, C. A. M. Seidel, *ChemPhysChem* **May 2005**, *6*, 791–804.

[169] T. Klein, A. Löschberger, S. Proppert, S. Wolter, S. van de Linde, M. Sauer, *Nature Methods* **Jan. 2011**, *8*, 7–9.

[170] B. Hein, K. I. Willig, C. A. Wurm, V. Westphal, S. Jakobs, S. W. Hell, *Biophysical Journal* **Jan. 2010**, *98*, 158–163.

[171] J. C. M. Gebhardt, D. M. Suter, R. Roy, Z. W. Zhao, A. R. Chapman, S. Basu, T. Maniatis, X. S. Xie, *Nature Methods* **May 2013**, *10*, 421–426.

[172] A. Kirchhofer, J. Helma, K. Schmidthals, C. Frauer, S. Cui, A. Karcher, M. Pellis, S. Muyldermans, C. S. Casas-Delucchi, M. C. Cardoso, H. Leonhardt, K.-P. Hopfner, U. Rothbauer, *Nature Structural & Molecular Biology* **Dec. 2009**, *17*, 133–138.

[173] I. Chen, M. Howarth, W. Lin, A. Ting, *Nature Methods* **2005**, *2*, 99–104.

[174] R. P. J. Nieuwenhuizen, M. Bates, A. Szymborska, K. A. Lidke, B. Rieger, S. Stallinga, **May 2015**, *10*, 1–18.

[175] Atto-tec GmbH, Recommended Procedures for Labeling, **2015**.

[176] Abberior GmbH, Recommended labeling protocols, **2015**.

[177] J. B. Randolph, A. S. Waggoner, *Nucleic Acids Research* **1997**, *25*, 2923–2929.

[178] D. Bout, W. T. Yip, D. Hu, D. K. Fu, T. M. Swager, *Science* **1997**, *277*, 1074–1077.

[179] K. S. Grußmayer, F. Steiner, J. M. Lupton, D.-P. Herten, J. Vogelsang, *ChemPhysChem*.

[180] J. Yu, D. Hu, P. Barbara, *Science* **Aug. 2000**, *289*, 1327–1330.

[181] H. Lin, S. R. Tabaei, D. Thomsson, O. Mirzov, P.-O. Larsson, I. G. Scheblykin, *Journal of the American Chemical Society* **June 2008**, *130*, 7042–7051.

[182] I. Scheblykin, G. Zoriniants, J. Hofkens, S. De Feyter, M. Van der Auweraer, F. C. De Schryver, *ChemPhysChem* **Mar. 2003**, *4*, 260–267.

[183] J. Vogelsang, T. Adachi, J. Brazard, D. A. Vanden Bout, P. F. Barbara, *Nature Materials* **Dec. 2011**, *10*, 942–946.

[184] H. Lin, R. Camacho, Y. Tian, T. E. Kaiser, F. Würthner, I. G. Scheblykin, *Nano Letters* **Feb. 2010**, *10*, 620–626.

[185] F. Feller, D. Geschke, A. P. Monkman, *Journal of Applied Physics* **2003**, *93*, 2884–7.

[186] M. Meier, S. Karg, K. Zuleeg, W. Brütting, M. Schwoerer, *Journal of Applied Physics* **1998**, *84*, 87–7.

[187] J. Schafferhans, A. Baumann, C. Deibel, V. Dyakonov, *Applied Physics Letters* **2008**, *93*, 1–4.

[188] J. C. Bolinger, L. Fradkin, K.-J. Lee, R. E. Palacios, P. F. Barbara, *Proceedings of the National Academy of Sciences of the United States of America* **Feb. 2009**, *106*, 1342–1346.

[189] C. Giebeler, S. A. Whitelegg, A. J. Campbell, M. Liess, S. J. Martin, P. A. Lane, D. D. C. Bradley, G. Webster, P. L. Burn, *Applied Physics Letters* **1999**, *74*, 3714–4.

[190] Y. Kim, S. Cook, S. M. Tuladhar, S. A. Choulis, J. Nelson, J. R. Durrant, D. D. C. Bradley, M. Giles, I. McCulloch, C.-S. Ha, M. Ree, *Nature Materials* **Feb. 2006**, *5*, 197–203.

[191] F. Chiti, C. M. Dobson, *Annual Review of Biochemistry* **2006**, *75*, 333–366.

[192] C. A. Wurm, K. Kolmakov, F. Göttfert, H. Ta, M. Bossi, H. Schill, S. Berning, S. Jakobs, G. Donnert, V. N. Belov, S. W. Hell, *Optical Nanoscopy* **2012**, *1*.

[193] J. B. Grimm, B. P. English, J. Chen, J. P. Slaughter, Z. Zhang, A. Revyakin, R. Patel, J. J. Macklin, D. Normanno, R. H. Singer, T. Lionnet, L. D. Lavis, *Nature Methods* **Jan. 2015**, *12*, 244–250.

[194] R. B. Altman, Q. Zheng, Z. Zhou, D. S. Terry, J. D. Warren, S. C. Blanchard, *Nature Methods* **May 2012**, *9*, 428–429.

[195] P. Tinnefeld, T. Cordes, *Nature Methods* **May 2012**, *9*, 426–427.

[196] C. Haan, S. Kreis, C. Margue, I. Behrmann, *Biochemical Pharmacology* **Nov. 2006**, *72*, 1538–1546.

[197] W. H. Goldmann, V. Auernheimer, I. Thievessen, B. Fabry, *Cell Biology International* **Mar. 2013**, *37*, 397–405.

[198] B. Geiger, A. Bershadsky, R. Pankov, K. M. Yamada, *Nature Reviews Molecular Cell Biology* **Nov. 2001**, *2*, 793–805.

[199] X. Michalet, R. A. Colyer, G. Scalia, A. Ingargiola, R. Lin, J. E. Millaud, S. Weiss, O. H. W. Siegmund, A. S. Tremsin, J. V. Vallerga, A. Cheng, M. Levi, D. Aharoni, K. Arisaka, F. Villa, F. Guerrieri, F. Panzeri, I. Rech, A. Gulinatti, F. Zappa, M. Ghioni, S. Cova, *Philosophical Transactions of the Royal Society of London. Series B* **Feb. 2013**, *368*, 1–22.

[200] P. Dedecker, F. C. De Schryver, J. Hofkens, *Journal of the American Chemical Society* **Feb. 2013**, *135*, 2387–2402.

[201] D. M. Shcherbakova, V. V. Verkhusha, *Current Opinion in Chemical Biology* **June 2014**, *20*, 60–68.

[202] C. Eggeling, S. Berger, L. Brand, J. R. Fries, J. Schaffer, A. Volkmer, C. A. Seidel, *Journal of Biotechnology* **Apr. 2001**, *86*, 163–180.

[203] N. K. Lee, A. N. Kapanidis, H. R. Koh, Y. Korlann, S. O. Ho, Y. Kim, N. Gassman, S. K. Kim, S. Weiss, *Biophysical Journal* **Jan. 2007**, *92*, 303–312.

[204] S. Kalinin, T. Peulen, S. Sindbert, P. J. Rothwell, S. Berger, T. Restle, R. S. Goody, H. Gohlke, C. A. M. Seidel, *Nature Methods* **Nov. 2012**, *9*, 1218–1225.

[205] A. Röhl, D. Wengler, T. Madl, S. Lagleder, F. Tippel, M. Herrmann, J. Hendrix, K. Richter, G. Hack, A. B. Schmid, H. Kessler, D. C. Lamb, J. Buchner, *Nature Communications* **2015**, *6*, 1–14.

[206] O. Schwartz, D. Oron, *Physical Review A* **Mar. 2012**, *85*, 1–5.

[207] O. Schwartz, J. M. Levitt, R. Tenne, S. Itzhakov, Z. Deutsch, D. Oron, *Nano Letters* **Dec. 2013**, *13*, 5832–5836.

[208] *Handbook Of Biological Confocal Microscopy*, (Ed.: J. B. Pawley), Springer US, Boston, MA, **2006**.

[209] E. Charbon, *Philosophical Transactions of the Royal Society A: Mathematical Physical and Engineering Sciences* **Feb. 2014**, *372*, 1–31.

[210] F. Guerrieri, S. Tisa, A. Tosi, F. Zappa, *IEEE Photonics Journal* **Aug. 2015**, *2*, 759–774.

[211] L. M. Hirvonen, F. Festy, K. Suhling, *Optics Letters* **2014**, *39*, 5602–5604.

[212] K. Stöhr, D. Siegberg, T. Ehrhard, K. Lymperopoulos, S. Öz, S. Schulmeister, A. C. Pfeifer, J. Bachmann, U. Klingmüller, V. Sourjik, D.-P. Herten, *Analytical Chemistry* **Oct. 2010**, *82*, 8186–8193.

[213] J. Bogomolovas, B. Simon, M. Sattler, G. Stier, *Protein Expression and Purification* **Mar. 2009**, *64*, 16–23.

[214] K. S. Grußmayer, Diploma thesis, Naturwissenschaftlich-Mathematischen Gesamtfakultät der Ruprecht-Karls-Universität Heidelberg.

ACKNOWLEDGEMENTS

An dieser Stelle möchte ich mich bei allen bedanken, die mich bei der Enstehung meiner Doktorarbeit unterstützt haben.

Bei Dirk-Peter Herten, meinem Betreuer und Mentor, für die Förderung meiner Doktorarbeit. Im Speziellen für ein immer offenes Ohr und wertvollen Rat bei Problemen, für die vielen kritischen Diskussionen, die spannenden Fragestellungen und für die Möglichkeit auf zahlreichen Konferenzen mit internationalen Forschern zusammenzukommen. Du hast mir Geholfen immer den Überblick zu bewahren.

Bei den Arbeitskollegen der Arbeitsgruppe für Einzelmolekülspektroskopie und bei unserem Arbeitsgruppenleiter Dirk-Peter Herten für eine unterhaltsame Zeit auch außerhalb des Labors: Daniel Barzan, Jessica Balbo, Tanja Ehrhard, Anton Kurz, Konstantinos Lymperopoulos, Arina Rybina, Michael Schwering, Anne Unger, Christina Spassova, Dominik Brox, Andreas Haderspeck, Klaus Yserentant, Ilse Valtierra, Siegfried Hänselmann und Martin Seefeld. Die angenehme Arbeitsatmosphäre mit großer Diskussions- und Hilfsbereitschaft hat viel zum Gelingen meiner Arbeit beigetragen. Die drei Uhr Kaffeepause war lange Zeit ein fester Bestandteil meines Arbeitstages, wie auch das wöchentliche Fußballspiel.

Bei Sebastian Bierbaum für die kritischen Diskussionen über Photonenstatistik und die weiterführende Bearbeitung des Forschungsthemas im Rahmen seiner Masterarbeit.

Bei den Forschungspraktikanten die ich im Laufe meiner Arbeit betreut habe, insbesondere Anne Schöffler und Martine Haan, die mit Untersuchungen zur Photostabilität von Farbstoffen die Vorarbeit für einige Messungen geliefert haben.

Bei den Korrekturlesern Dominik Brox, Andreas Haderspeck, Klaus Yserentant, Siegfried Hänselmann, Sebastian Bierbaum, Martine Haan, Nikolas Dimitriadis und Moritz Kiehn für die hilfreichen Kommentare und Beseitigung von Fehlern.

Bei allen Beteiligten des Graduiertenkolleg 1114 „Optische Messtechniken für die Charakterisierung von Transportprozessen an Grenzflächen“ der Deutschen Forschungsgemeinschaft (DFG) für die gemeinsame Zeit auf zahlreichen GRK-Veranstaltungen mit interessanten wissenschaftlichen und privaten Diskussionen. In diesen Rahmen bedanke ich mich auch bei der DFG für die finanzielle Förderung in Form eines Doktorandenstipendiums.

Bei meinen Kooperationspartnern Jan Vogelsang und Florian Steiner aus der Gruppe von J. M. Lupton an der Universität Regensburg für die unkomplizierte und produktive Zusammenarbeit sowie das Forschungsobjekt konjugierte Polymere.

Bei allen, die nicht explizit erwähnt wurden, aber meine Arbeit wesentlich erleichtert bzw. erst ermöglicht haben, wie z.B. der elektronischen und feinmechanischen Werkstatt im PCI sowie der Laborbetreuung, Verwaltung und IT im BioQuant und PCI.

Spezieller Dank geht an Daniel Barzan, Dominik Brox und Klaus Yserentant für die fortwährende Unterstüzung in allen Belangen sowie an Anton Kurz für die Vorarbeit und Einführung in das Forschungsthema.

Ein Dankeschön gebührt natürlich auch meinen Freunden, die mich auf meinem Weg begleitet und bei Laune gehalten haben.

Der größte Dank gilt Moritz Kiehn und meiner Familie. Euer Rückhalt und Unterstützung ist sehr wichtig für mich.